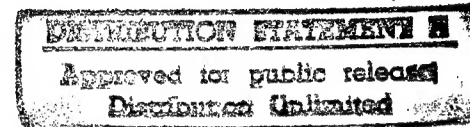


JPRS-JST-92-009  
20 MARCH 1992



FOREIGN  
BROADCAST  
INFORMATION  
SERVICE

# ***JPRS Report***



# **Science & Technology**

***Japan***

STA'S NATIONAL RESEARCH INSTITUTE  
FOR METALS RESEARCH  
REPORT 12

**19980128 187**

**DTIC QUALITY INSPECTED 3**

REPRODUCED BY  
U.S. DEPARTMENT OF COMMERCE  
NATIONAL TECHNICAL INFORMATION SERVICE  
SPRINGFIELD, VA. 22161

JPRS-JST-92-009  
20 MARCH 1992

SCIENCE & TECHNOLOGY  
JAPAN

STA'S NATIONAL RESEARCH INSTITUTE  
FOR METALS RESEARCH  
REPORT 12

916C0048 Tokyo KENKYU HOKOKUSHU 12 in Japanese 1991 Issue

[Selected articles from the Research Reports Issued Feb 91 by the National Research Institute for Metals of the Science and Technology Agency]

CONTENTS

Research on Development of Lightweight Thermal Resistance Intermetallic Compound Materials.....	1
Research on Properties of New Superconducting Wire Materials for Nuclear Fusion Reactor.....	25
Research on Manufacturing Intermetallic Compounds by Self- Propagating High-Temperature Syntheses.....	44
Composite Materials R&D.....	54
High-Performance Crystal Control Alloy R&D.....	68

**Research on Development of Lightweight Thermal Resistance Intermetallic Compound Materials**

916C0048A Tokyo KENKYU HOKOKUSHU 12 in Japanese 1991 Issue pp 1-17

[Special Research, FY85-FY88]

**[Text] Abstract**

From the research over the past five years it has been found that the intermetallic compound TiAl has excellent high temperature characteristics as a lightweight heat-resistant material, and that although this compound has defects in low ductility at ordinary temperatures and hardness of processing at high temperatures, these are not insurmountably difficult defects. The objects of this special research project which was started in FY 1985 are to overcome the defects of TiAl by developing schemes based on the study of alloys, the plastic working method, etc., and to establish the basic manufacturing method of materials based on TiAl. The strategic goal is to have the world recognize TiAl as a structural material for industries.

In the present project, the five fields of alloy design, melting and solidification, plastic deformation, powder metallurgy, and surface modification were the principal research topics. In alloy design, the influence of the control over the composition and texture on the structure and characteristics of the TiAl-based alloys was studied. Research results that are worthy of mention re the findings that the alloys doped with Mn and dispersed  $Ti_3Al$  manifest ductility of 3 percent at ordinary temperatures, and that the addition of Si enhances the resistance to oxidation. In melting and solidification, the dissolution method by means of a plasma beam furnace and high frequency vacuum melting that uses a CaO crucible were studied. It was found that ingots of sound TiAl-based alloys can be obtained by plasma beam melting, but it was impossible to avoid the oxygen content of ingots obtained by high-frequency melting, which is a handy method, to be about three times higher than the oxygen content of the plasma melted materials. In plastic deformation, a working simulation device was developed in order to investigate the isothermal forging method which is effective for working the compounds and controlling the texture. The plastic behavior and the working method of TiAl at high temperatures and the lubricant to be used in isothermal forging were also

investigated. In order to apply the powder metallurgical method to TiAl, the relationship among the raw materials, forming and sintering conditions, and the mechanical properties was studied. In the sintering of a cold green compact, it was not possible to obtain materials free from voids; thus it was necessary to subject powder to hot isostatic pressing (HIP) by sealing it in a stainless steel container. The characteristics of the HIP materials depended on the method of preparation of the raw material powder. For surface modification of TiAl, a method of injecting nitrogen ions was used. The distribution of injected nitrogen and the analysis of nitrides produced were studied along with surface hardening, improvement of corrosion resistance, etc.

## 1. Introduction

Lightweight materials that can be used in a high-temperature environment are constantly in demand by those who are involved in the design of equipment for high temperature. However, the performance of typical metallic materials has already been exhaustively developed by now, and their characteristics are said to be approaching the saturated state. However, there are too many problems in malleability and ductility, toughness, and manufacturability to make ceramics the material for general structures. The underlying idea of the present research is that since there exists an unexplored field of structural materials called intermetallic compounds between metals and ceramics, which have characteristics essentially between the two, we should try to seek epoch-making new materials for structures in this field rather than going directly to the development of ceramic materials.

Among the intermetallic compounds there exist some which have the reversed temperature dependence of strength which is the very characteristic we are seeking. Unfortunately, such a compound is usually brittle. That the grain boundary brittleness of Ni<sub>3</sub>Al which belongs to such a group of compounds can be enormously improved by the addition of a minute amount of boron has just been discovered recently. This means that the ductility at ordinary temperatures of the intermetallic compounds can be improved by a scheme based on the theory of alloys, unless they have an especially strong nonmetallic property. Then the question is: which intermetallic compounds, with metallic properties that have strong reversed temperature dependence, have the highest value for development? As the answer to this question, we at the National Research Institute for Metals (NRIM) selected the intermetallic compound TiAl which has a melting point of 1753 K and specific gravity of 3.7. This compound has an electrical conductivity comparable to metallic titanium, and a crystal structure of relatively good crystal symmetry of Ll<sub>0</sub> type with an axial ratio of 1.02.

At NRIM, we selected TiAl five years before the start of the present special research program, and expanded the research scale from general research to specified research. During this period it was found that Ti-rich TiAl is not so brittle as was believed, making it possible to achieve compressive deformation of more than 20 percent at ordinary temperatures, that it has a high yield strength of 400 MPa at 1073 K, and 250 MPa at 1273 K, that it is possible to subject it to high temperature plastic working if special methods are used, that it can be subjected to cutting work, etc. The objects of the

present special research program which was started in FY 1985 based on these findings are to develop characteristics of TiAl to establish it as a new industrial material, and to establish a basic manufacturing method. The result of this special research program became the object of attention not only of scientific societies but also of industries. At present, materials based on TiAl are being actively investigated in many universities and large enterprises specialized in metals.

## 2. Alloy Design

In order to put the metallic compound TiAl to practical application it is necessary to improve ductility at ordinary temperatures and resistance to oxidation which is degraded at high temperatures above 1073 K. To resolve these problems we examined methods of adding alloy elements.

The ductility of a compound is closely related to its crystal structure, and the basic data required in attempting to improve ductility at ordinary temperatures by the addition of an alloy element is the change in the crystal structure of the compound that accompanies the solid solution of the added element. In Section 2.1, the techniques of predicting the tendency in the change of crystal structure of TiAl that accompanies the addition of an alloy element will be examined. In addition, in Section 2.2, the influence of the added element on the texture will be examined in its connection with ductility, and the structural factors required to improve the cold ductility will be extracted.

On the other hand, as to improving the characteristic of resistance to oxidation, techniques accumulated for various kinds of heat resisting alloys will be applied to the TiAl phase, and the basic data will be studied. Namely, in Sections 2.2 and 2.3, the relationship between the addition of elements Y, Si, Cr, Al, etc., which are said to improve oxidation resistance and the increase in the amount of oxidation will be examined at a temperature near 900°C.

### 2.1 Influence of Addition of a Third Element on the Crystal Structure of TiAl

#### 2.1.1 Experimental Method

1) **Specimens:** TiAl-based alloys with an added third element are produced by argon arc dissolution. Their chemical compositions are shown in Table 1. Here, Zr and Nb are elements having atomic diameters greater than that of Al, whereas Mn and V have smaller atomic diameters.

2) **Crystal Structure Analysis:** By X-ray analysis, measurement of the lattice constants and the amount of element distribution in the sublattice were determined. It should be mentioned that in the present research we developed a new analytical method regarding the determination of the amount of element distribution in the sublattices.

Table 1. Chemical Composition (wt%)

Ti-34.00Al	Ti-34.89Al- 3.10Zr
Ti-32.78Al- 3.58Mn	Ti-33.89Al- 5.86Zr
Ti-31.59Al- 7.09Mn	Ti-31.92Al-11.33Zr
Ti-30.42Al-10.52Mn	Ti-30.08Al-16.44Zr
Ti-31.99Al- 5.91Nb	Ti-28.36Al-21.23Zr
Ti-30.11Al-11.43Nb	Ti-35.37Al- 1.76V
Ti-28.36Al-16.58Nb	Ti-34.75Al- 3.37V
Ti-32.03Al- 5.81Zr	Ti-38.00Al
Ti-30.18Al-11.24Zr	Ti-36.61Al- 3.67Mn
Ti-28.45Al-16.33Zr	Ti-35.25Al- 7.25Mn
Ti-33.15Al- 2.50V	Ti-35.72Al- 6.04Nb
Ti-32.30Al- 5.00V	Ti-33.58Al-11.67Nb
Ti-31.52Al- 7.50V	Ti-35.75Al- 5.94Zr
Ti-36.00Al	Ti-33.65Al-11.48Zr
Ti-35.64Al- 1.02Mn	Ti-36.10Al- 5.00V
Ti-35.32Al- 1.90Mn	
Ti-34.70Al- 3.62Mn	
Ti-33.42Al- 7.17Mn	

signify Ti, Al, and the third element, respectively. As shown in the bottom parts of Figures 1(a) and 1(b), in the case of addition of Zr and Nb, the values for the blank triangles are large, indicating that Zr and Nb mainly enter the Ti sites. Similarly, from Figures 1(c) and 1(d), it was found that Mn and V preferentially enter the Al sites. In addition, as the black circles and the blank squares show, addition of small amounts of Zr and Nb reduce the mutual replacement amounts of Ti and Al elements. Namely, the regularity is improved. In contrast, in the case of adding Mn and V, increase in the added amount reduces the mutual replacement amount, and increases the regularity. From these changes in the element distribution that accompanies the solid solution of the third element, several predictions can be obtained as to the modification of the TiAl phase. For example, Mn or V replaces Al of the TiAl phase and augments the atomic ratio, Ti/Al, in the phase. This suggests a reduction in the shared bonding in the crystal and the accompanying improvement in cold ductility.

### 2.1.2 Result and Consideration

1) As a result of examining the extension of the analytical method for the long-range regularity in binary system compounds to ternary system, it was found that the element distribution in the two sublattices of TiAl crystals that contain an added element can be determined by measuring at least two sets of integrated intensity that determines the regularity. An example of the result obtained by this technique is shown in Figure 1. In the figure, the symbols  $\square$ ,  $\circ$ , and  $\Delta$  represent the amounts of the element that enter the sublattice position that the Ti atom should properly occupy (Ti sites),  $\blacksquare$ ,  $\bullet$ , and  $\blacktriangle$  represent the corresponding amounts of the element that enter the sublattice position that Al should properly occupy (A site), and the circle, square, and triangle,

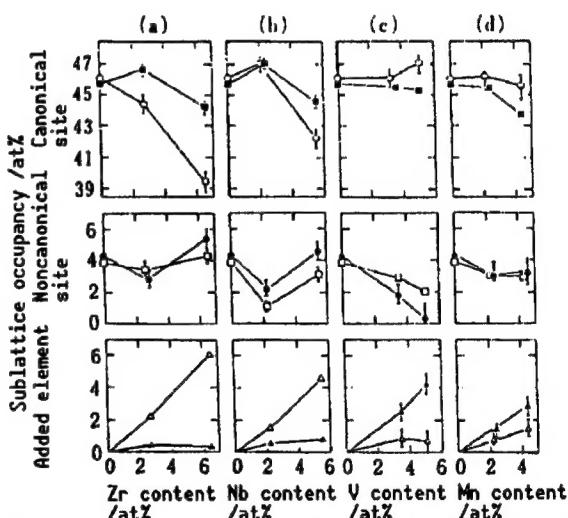


Figure 1. Quantities of Constituting Elements That Occupy the Ti Sublattice and Al Sublattice

2) Analogous to the element distribution in the sublattices, the size of the unit lattice and the anisotropy of crystals are considered to be closely related to the ductility at ordinary temperatures. The change of the TiAl crystal lattice accompanying the addition of a third element is shown in Figure 2. It can be seen that the addition of elements with large atomic radius Zr and Nb inflates the crystal lattice, and the addition of elements with small atomic radius Mn and V contracts the lattice. In addition, since the axial ratio  $c/a$  which represents the anisotropy of the crystal lattice is in the reciprocal relation to the mean atomic diameter ratio represented by  $D_{Ti}/D_{Al}$ , it can be concluded that  $c/a$  is determined by the amount of added element and the replacement position. From the point that the contraction of the lattice increases the cleavage fracture strength, it can be estimated from the data that the addition of Mn and V improves ductility at ordinary temperatures. In addition, from the fact that the addition of Mn and Zr improves the anisotropy of the lattice, the isotropy of deformation will be increased, and includes the possibility of improving ductility at ordinary temperatures.

### 2.1.3 Summary

The influence of the addition of a third element on the crystal structure of TiAl which is the fundamental data in improving ductility at ordinary temperatures due to addition of an alloying element was investigated.

- a) The replacement position of a third element added to the TiAl phase, and the mutual replacement amounts of Ti and Al were determined according to the analytical method developed by the present research. As a result, the trend estimation of the change in the mechanical properties accompanying the solid solution of a third element became possible.
- b) The rule on the change of the lattice constants accompanying the addition of a third element was formulated. Namely, the addition of a large element inflates the lattice, and the addition of a small element contracts it. Further, the axial ratio  $c/a$  of a crystal lattice can be determined if the amount of added element and the replacement position are found. As a result, it was possible to obtain the selection standards that are suited to the increase of the fracture strength and the enhancement of isotropy.

## 2.2 Influence of a Third Element on Structure and Mechanical Properties of TiAl-Based Alloys

### 2.2.1 Experimental Method

1) Specimen: The alloy compositions used are the same as in the previous section.

2) Structural Analysis: Analyses were made using optical microscope, scanning electron microscope, and electron beam microanalyzer.

3) The mechanical properties were investigated by hardness measurement, compression test using a square bar of 3 mm x 3 mm x 7 mm, and three-point bending test using a testpiece of 2.5 mm x 5.0 mm x 25 mm.

### 2.2.2 Experimental Result and Consideration

The result of the structural analysis is shown in Figure 3. Here,  $\gamma$  is the TiAl phase, and  $\alpha_2$  is  $Ti_3Al$  which appears in a TiAl-based alloy as the second phase. From the figure, it can be seen that in alloys of Ti-excess composition, the addition of Zr and Nb augments the volume factor of the  $\alpha_2$  phase, makes the structure finer, and reduces the atomic ratio Ti/Al in the TiAl phase. Moreover, the addition of V does not alter the volume factor and the atomic ratio, but the addition of Mn reduces the volume factor but increases the atomic ratio. In this way, the changes in the structure accompanying the addition of a third element can be predicted from the figure. Furthermore, it became clear that the addition of Mn and V increases the annealing twins, which leads to finer structure of the alloy. The compressive and bending strains at room temperature are shown in Figure 4. In the figure, notation such as "34 series" signifies that  $Al/(Ti+Al)$  in a TiAl-based alloy is fixed, and a third element is added. For a composition on the Ti-excess side, addition of a small amount of Mn and V increases the compressive ductility, whereas on the Al-excess side, addition of a large amount of Nb improves ductility. A similar tendency can also be seen in bending tests. As a result of an overall examination of the effect of adding an alloying element and the change in the crystal structure, it was concluded that an added element which is suitable for improving ductility is an element which reduces the stability of the TiAl crystal lattice, and more specifically, that it is Mn for Ti-excess compositions and is Nb for Al-excess compositions.

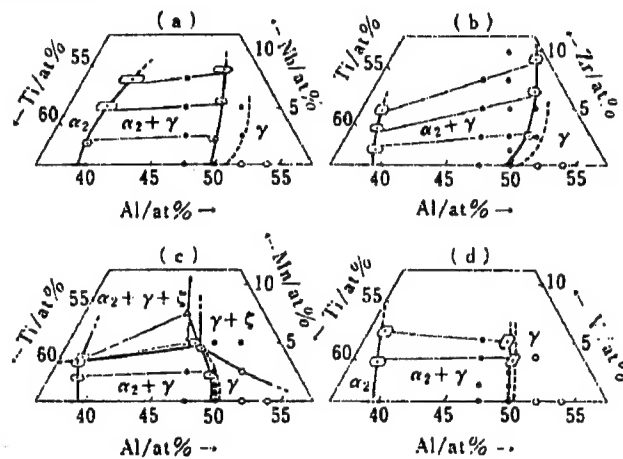


Figure 3. Phase Equilibria in Vicinity of TiAl Phase at 1273 K

The  $\alpha_2 + \gamma/\gamma$  phase boundaries shown by solid and broken lines correspond to short and long time heat treated materials, respectively.

6

### 2.2.3 Summary

In order to obtain the selection standards of a component element which is suitable for improving ductility at ordinary temperatures, the relationship among the added element, crystal structure, and the change in the alloy texture was systematically clarified, and the predictions and the actually measured ductility at ordinary temperatures were compared.

a) Addition of a large amount of Nb to an Al-excess TiAl-based alloy improves the compressive and bending ductility. The factors in improving ductility are the increased fineness in the texture due to dispersion of a small amount of the  $\alpha_2$  phase, reduction of the axial ratio, and nearly fixed volume of the unit lattice.

b) Addition of a small amount of Mn to a Ti-excess TiAl-based alloy improves the compressive and bending ductility. The factors in improving ductility are the increased fineness due to dispersion of a small amount of the  $\alpha_2$  phase and the annealing twins, the decrease in the axial ratio and the volume of the unit lattice, and the increase of the atomic ratio Ti/Al.

### 2.3 Effect of Third Element Addition on Oxidation Characteristic of TiAl-Based Alloys

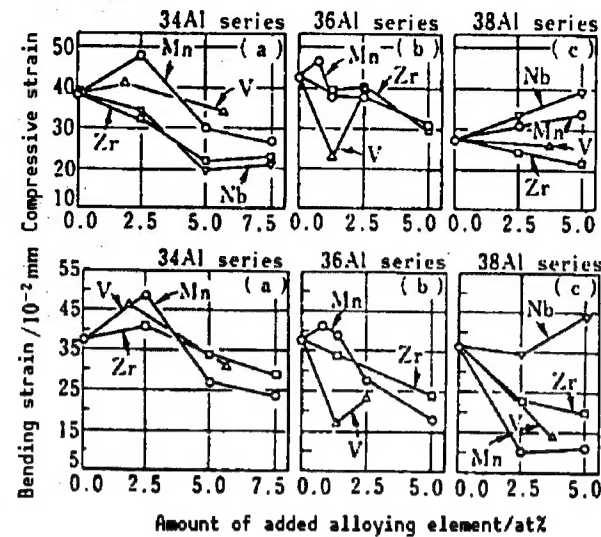


Figure 4. Changes in Compressive and Bending Strains Accompanying the Addition of an Alloying Element

Table 2. Chemical Composition of Alloys (wt%)

1) Specimen: The chemical compositions of the TiAl-based alloys are shown in Table 2. Here, in addition element Y is well known for its effect to improve the adhesion to oxide film and to improve the oxidation characteristic of Ni-Cr alloy. Chromium is added to stainless steel, and Si is added to austenite stainless steel, and it is known that the oxide films produced are dense and have an excellent protective characteristic. Manganese is an element which improves the cold ductility of TiAl-based alloys.

36Al	Ti-36Al
38Al	Ti-38Al
Cr-1	Ti-36Al -0.69Cr (0.5at%)
2	1.38Cr (1.0)
3	2.76Cr (2.0)
Y-1	Ti-36Al -1.17Y (0.5)
2	2.34Y (1.0)
3	4.68Y (2.0)
Mn	Ti-345Al-1.50Mn (1.0)
Si-1	Ti-36Al -0.15Si
2	0.30Si
3	0.50Si
4	1.00Si

2) The oxidation experiment was carried out in the air in the range of 1173~1223 K.

### 2.3.2 Result and Consideration

Irrespective of the added element, the oxide film produced consists, in order from outside, of  $TiO_2$ ,  $Al_2O_3$ , and a mixed layer of  $TiO_2$  and  $Al_2O_3$ . The resistance characteristic to oxidation of the TiAl phase is clearly superior to Ti alloys. The reason for this is that there is a large amount of Al in TiAl so that  $Al_2O_3$  is readily formed. Figure 5 shows the increase of oxides in TiAl alloys at 1173 K. The addition of Cr, Mn, and Y degrades as resistance characteristic to oxidation, but the addition of Si clearly improves the resistance characteristic to oxidation. As a result of structure analysis of the oxide films, it is concluded that the reason for this is that  $SiO_2$  forms a continuous oxide film which suppresses the diffusion of oxide ions and metallic ions. In addition, it was found that the addition of Y improves the adhesion of the oxide film, and that the degradation of the resistance to oxidation brought about by the addition of Cr or Mn is due to the fact that it makes the  $Al_2O_3$  layer porous.

### 2.4 Brief Summary

The fracture mode of TiAl at room temperature is cleavage fracture or pseudo cleavage fracture, and the slip deformation exhibits a strong flatness. Therefore, considering that the most plausible method for improving cold ductility of the TiAl phase is the addition of an alloying element, we investigated in this research the influence of an added element on the cold ductility of the TiAl phase. In addition, the resistance to oxidation was also studied. A summary of the result is given below.

- An alloying element which causes the crystal lattice of the TiAl phase by solid solution, reduces the anisotropy of the lattice, and increases the alloy Ti/Al; for example, Mn improves the cold ductility of a TiAl-based alloy.
- An element which forms a solid solution with the TiAl phase and forms a dense oxide film in the oxidation process, for example, Si, improves the characteristic of resistance to oxidation of the TiAl phase.

### 3. Melting and Solidification

In melting TiAl, it is possible to dissolve it by arcing in an Ar atmosphere if the amount is small, but various problems will arise if the amount is several kilograms or more. For example, in an electrode consumption type vacuum arc furnace, the melting rate is high due to stabilization of the arc

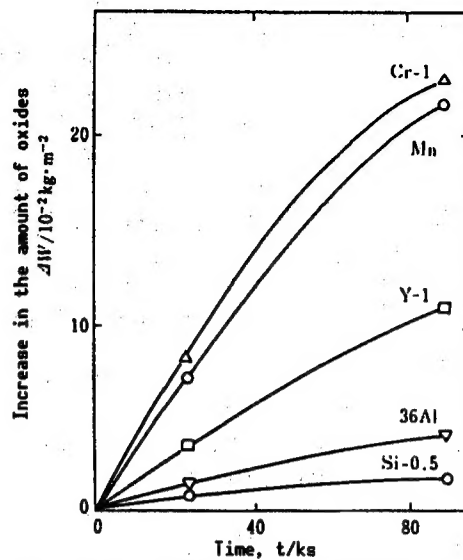


Figure 5. Curves for Increase in Amount of Oxides

which tends to generate microcracks.<sup>2</sup> On the other hand, in an electron beam furnace, the pressure in the furnace is low at  $10^{-2}\text{--}10^{-4}\text{Pa}$  so that Al evaporates which makes melting impossible.

Therefore, in the present research, TiAl was dissolved by the use of a plasma beam furnace which permits free adjustment of the melting rate and the in-furnace pressure is higher than that of an electron beam furnace by two orders of magnitude.

Next, the possibility of using high frequency melting was investigated. This method is desirable for both profitability and workability. However, it is said that the high-frequency melting is not feasible because of an easy reaction with the crucible of Ti and Ti alloys that are active, which leads to the contamination of the molten metal. However, the rate of Ti atom in TiAl is half that of metallic Ti so that the activity will be reduced and it seems as if melting in crucible is possible. Therefore, the feasibility was examined for using a crucible made of CaO which is one of the most chemically stable and general industrial materials.

### 3.1 Experimental Method

For the plasma beam melting of TiAl, a 60 KVA furnace was used. The principle of the furnace is to convert Ar gas to high-temperature gas of low-pressure plasma within a Ta tube (cathode with inner diameter of 13 mm) by the use of a high-frequency superposed dc power supply, and to melt a sample used as the anode by thermoelectrons that are generated from the plasma. The flow rate of Ar gas for plasma was 0.8 l/min and the current for melting was 900 A. In addition, the pressure within the furnace at the time of optimum melting was around 2.7 Pa. As the raw material for a primary melting by a water-cooled hearth (width 60 mm, depth 40 mm, and length 100 mm), a compressed body of sponge titanium and chopped pieces of Al rod (diameter 3 mm) was used. An ingot (5.2 kg) 80 mm in diameter was obtained by a secondary-melting of the obtained rod material by the pull-down method.

For the high-frequency melting of TiAl a commercially available CaO crucible of high purity and high density, was used having an inner diameter of 74 mm, outer diameter of 94 mm, and height of 170 mm. In addition, sintered crucibles with 5 percent and 10 percent CaF<sub>2</sub> blended were also used to suppress the reactivity of the CaO crucible. The 0.7~1.1 kg of TiAl was melted by a high-frequency melting furnace at 5 kW and 10 kHz. The pressure within the furnace was kept at 0.53 Pa before start of melting, and the pressure was increased  $2.1 \times 10^4\text{Pa}$  by passing Ar gas after completion of melting, and holding it for 3 minutes or so, and then poured into a metallic die at about 1873 K.

### 3.2 Experimental Result

#### 3.2.1 Plasma Beam Dissolution

Although Ti-36wt%Al was melted several times it was not possible to obtain a solution with desired composition. Namely, the Al of the obtained ingots was scattered in the range of 34~32wt% (Al yield of 95~89 percent) which varied

for every melting. This decrease in the Al yield is due to evaporation of Al from the surface of the melt pool, and this was understood from the generation of a vaporized layer close to pure Al on the surface of the hearth after melting. Here, the cleaning of the evaporated layer of Al is cumbersome work.

Next, reproducibility was examined. Even with melting in accordance with the standard manual for the apparatus, the pressure within the furnace varied within the range of 0.93~4.0 Pa. Since it was suspected that the in-furnace pressure variation is related to the evaporation of Al, the relationship between the in-furnace pressure and the evaporation rate of Al was investigated. The evaporate rate was determined from the melting time and the weight decrease. The size of the pool is 60 mm wide and 70 mm long. The result is shown in Figure 6. Namely, the evaporation rate of Al within the range of variation of the in-furnace pressure that is generated by ordinary dissolution is, on the high-vacuum side, even twice as large as that on the low-vacuum side, and it became clear that this phenomenon strongly influences the yield of Al. To resolve this problem, the Ar gas flow rate for plasma was constantly regulated in small amounts in order to keep the in-furnace pressure at a constant level, and a satisfactory reproducibility was obtained by this arrangement. The optimum condition of the pressure within the furnace was 6~7 Pa and the yield of the Al was 96 percent.

Next, Ti-34.5wt%Al-1.5wt%Mn was melted. As a result of melting under the above-mentioned conditions, Mn was not observed in the ingots by almost complete evaporation. Then, aware of the existence of a limit to the increase of blended amount of Mn, the sample was melted at the lowest current for melting, 750 A. Even in this case, 40% in the melting of a rod material and 50 percent in the melting of pull-down melting, of the Mn was evaporated. Eventually, by blending 4.5%Mn an ingot of 1.5%Mn was obtained. As in the above, melting of TiAl containing Mn in a plasma beam furnace is difficult.

The quality of the ingots obtained was examined. Samples were taken from the top, bottom, and sides of the ingots to examine the micro and macro segregation of EPMA, and homogeneous ingots with obtained which revealed no segregation that may be considered due to melting and solidification. In addition, the ingots were sound materials having neither microporosity nor microcracks. On the other hand, among the ingots doped with Mn, some segregations were observed in Al, Ti, and Mn because of the melting at low temperatures, but they were not of the degree that should be of special concern.

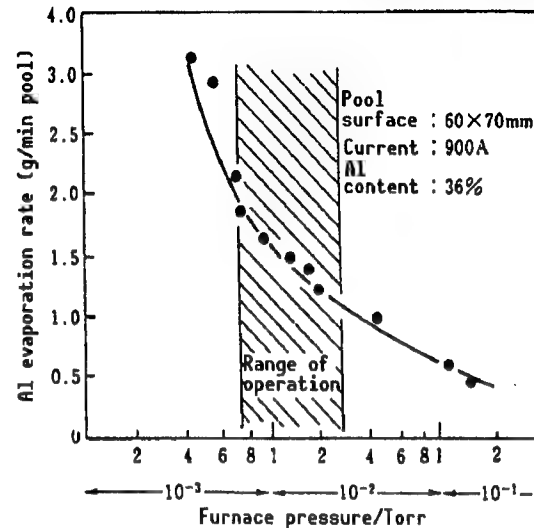


Figure 6. Influence of Pressure in Furnace on the Rate of Al Evaporation

### 3.2.2 High-Frequency Melting

Figure 7 shows the oxygen and calcium contents of the ingots. When TiAl is melted in a CaO crucible, the oxygen content in an ingot is in the range of 0.10~0.15 percent. This value is about three times as high as the value of 0.04 percent for the plasma beam furnace shown in Figure 7. It should be mentioned that a crucible was mixed with CaF<sub>2</sub> that does not react with Ti, for the purpose of reducing the oxygen content, but no oxygen effect was observed. On the other hand, the content of Ca as an inclusion of CaO was 0.02~0.04 percent which is not too high a value. However, it is of concern as a nonmetallic inclusion. Therefore, its area factor was determined according to the measuring method of nonmetallic inclusion in iron and steel. As a result, it was found that the value is 0.12~0.17 percent in the case of high purity CaO crucible which is comparable to the value of 0.1~0.2 percent of the commercially available case hardening steel, being of no particular concern. It should be noted that the area factor for a crucible compounded with CaF<sub>2</sub> is 0.08 percent, so that the mixing was effective for reducing the nonmetallic inclusions. Moreover, the size of the nonmetallic inclusions is about 1~5 μm and are considered not to be adversely affecting the mechanical properties. Table 3 shows a comparison with the dissolved materials by a plasma beam furnace. Magnesium and Cl have nearly equal values for both cases and there will be no problem.

Table 3. Analytical Values of Ingots

	O	Ca	Mg	Cl
CaO crucible	0.10 ~0.15	0.02 ~0.07	0.003 ~0.007	0.02 ~0.04
Plasma beam	0.02 ~0.04	0	0.001 ~0.005	0.02 ~0.03

following problems: 1) the press forming of the raw material for melting and 2) the long time required for rod material melting and pull-down melting. It is not an efficient melting method. For this reason the establishment of high-frequency melting technology is proposed.

The oxygen content of TiAl obtained by high-frequency melting was in the range of 0.1~0.15 percent for all cases, with the mean value 0.13 percent. This value can be considered as the equilibrium value for the case of using the CaO crucible. This fact can also be understood from the following phenomenon; that is, the equilibrium oxygen quantity when pure Ti is held in a CaO crucible for 20 minutes is 1~1.3 percent. Further, when the oxygen quantity in Ti which is in equilibrium with CaO is computed, using the free energy for partial mol

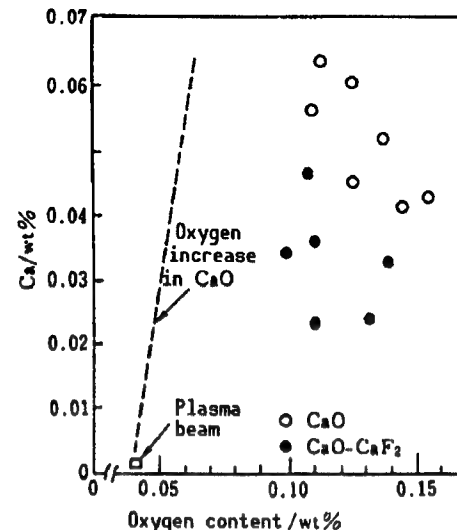


Figure 7. Oxygen and Calcium Contents in TiAl Ingot

### 3.3 Consideration

In melting TiAl in a plasma beam furnace, a sound ingot having desired composition can be obtained if the pressure in the furnace is kept constant. Although this method is an excellent melting method, its industrial use will give rise to the

formation of Ti-O system at 1473 K obtained by Kubachewsky, et al., it comes out to be 1.3 percent which agrees with the above-mentioned measurement value. On the other hand, from the value of about one-tenth for the activity of Ti in TiAl obtained by these authors, the oxygen quantity when a CaO crucible is used comes out to be 0.13 percent. In other words, when TiAl is melted by the use of CaO crucible, the phenomenon that the oxygen quantity becomes 0.13 percent is an inevitable fact. For this reason, the development of a material for crucible which brings down the activity of CaO is necessary for reducing the oxygen.

### 3.4 Brief Summary

(1) In melting TiAl in a plasma beam furnace, the problem with reproducibility of the composition arises, but it can be settled by fixing the pressure within the furnace at a constant level. The ingots obtained were sound ones with uniform composition and free of forging defects.

(2) When TiAl is melted in a CaO crucible, the two react with each other and the oxygen content becomes about 0.13 percent. This value is higher compared with the vale of 0.04 percent in a plasma beam furnace, but seems to be inevitable. Further, a nonmetallic inclusion CaO is observed in crucible melted materials, but the area factor is about 0.1~0.2 so that it is considered not a value of concern.

(3) Research on new crucible materials that have CaO as the principal component is necessary.

## 4. Plastic Deformation

In order to put the TiAl intermetallic compound to practical use as structural materials, R&D on forming and processing technologies such as precision forging, powder metallurgy, plastic processing, etc., have been pushed vigorously.

For forming and processing as well as improving the material by such a plastic processing method as isothermal forging for hard-to-process materials of this kind, we developed an apparatus for simulating plastic processing at high temperatures of the intermetallic compounds. Using this apparatus we examined high temperature deformation behavior, high temperature processability, and the lubrication characteristic in isothermal forging, of the TiAl compounds.

### 4.1 Preliminary Consideration for Experimental Manufacture of the Apparatus

The principal factors to be considered in the plastic processing of the hard-to-process materials like intermetallic compounds are shown below.

(1) High Temperature Processability: Considering the simplicity of stress and strain, high reproducibility, difficulty in preparing testpieces of the object material, etc., the best evaluation method of processability will be the simple compression method. We decided to use this method for this apparatus,

and extracted the following technical problems. In a compression test, the influence of friction between a material and a tool becomes a problem. In the range of uniform deformation, the equivalent stress ( $\sigma$ ) and the true stress coincide. When the friction between the sample and the tool is taken into account,  $\sigma$  is given by the following Equation (1).

$$\sigma = P/(1 + \mu D/3H), \quad (1)$$

where  $P$  is the mean compressive pressure,  $\mu$  is the friction coefficient, and  $D$  and  $H$  are the diameter and the height of the testpiece. A quantitative evaluation of the deformability by the compression test is difficult. However, it can be evaluated by comparing whether or not cracks generated in a compression testpiece are generated by a strain of a predetermined magnitude and over.

(2) Processing Tool and Processing Method: Ceramics can withstand stress at high temperatures better than Mo. However, their fracture toughness is extremely small compared with alloys. It is necessary to devise a design that will be able to withstand severe conditions for practical use. In this apparatus, use of sialon was considered.

(3) Characteristics of the Lubricant: The problem of lubrication in isothermal processing at a temperature above 1400 K has not been clarified so far. In this research, we examined glass and BN lubrication which are relatively stable even at high temperatures.

(4) Deformed Texture: As to the dynamic characteristics of the lower texture of de-crystallization, etc., we considered freezing the deformed state by quenching it by gas jet of Ar, etc., and examining it at room temperature.

(5) Material Quality After Processing: Since these are materials where it is difficult to apply ordinary hot pressing, we tried to obtain materials that make it possible to examine changes in the material characteristics by processing.

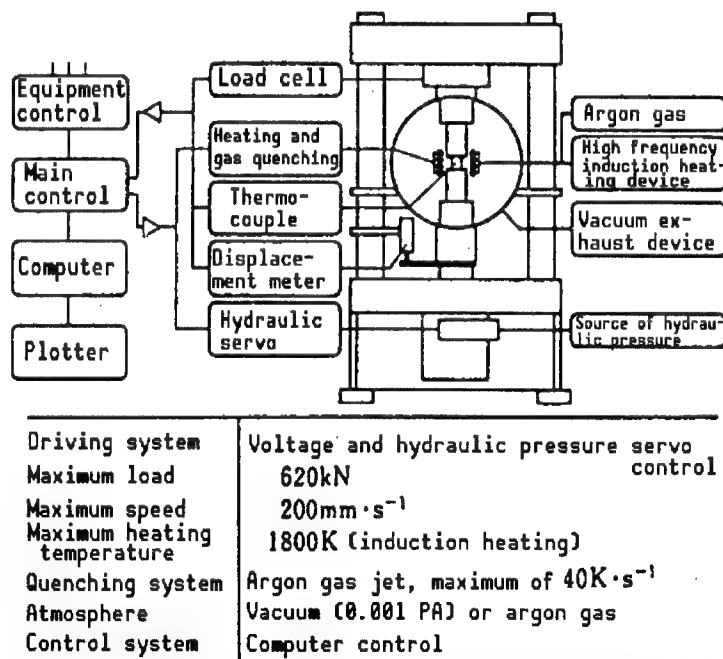


Figure 8. Schematic Diagram and Principal Performance of High-Temperature Processing Simulation Apparatus

## 4.2 Specifications and Performance of Experimentally Manufactured Apparatus

An apparatus aimed at satisfying the conditions of various factors described in the previous section was trial manufactured. A schematic diagram and its principal performance are shown in Figure 8. The test was carried out by full control of the program by personal computers, and the test result was output by the plotter.

## 4.3 Experiment on High-Temperature Plastic Deformation and Its Consideration

A testpiece of TiAl compound with a diameter of 25 mm and 30 mm high was inductively heated at a temperature rate of 4 K/s, and a satisfactory result was obtained with a followup delay within 5 K. Photograph 1 [not reproduced] shows an example of texture observation of the TiAl compound which was inductively heated, and quenched by Ar gas jet immediately after compressive deformation at high temperature. A dynamically recrystallized texture (a) by the so-called bulging mechanism and a twin deformation and a minute recrystallization in a part near the grain boundary are observed.

### (2) Ceramic Tools for Hot Processing

As a result of performing upset processing at constant temperatures with actual distortion above 1.2, and at the average pressure of 300 MPa after lubricating TiAl compound with BN or glass, the ceramic tool was broken three to five times. It was found that the durability of the working tool can be improved sharply by inserting a plate of Mo or W, or by using a method of winding ceramic fibers around the periphery of the working tool giving them tensile stress.

### (3) Compression Test With Constant Rate of Strain

A compression test with a constant rate of strain was carried out using a TiAl compound. The true stress-strain relationship in which the influence of friction on the stress is compensated for by Equation 1 (in Section 4.1), and the influence of the testing machine system is compensated for, is shown in Figure 9. In the example of testing a single  $\gamma$  phase material under 1445 K and  $0.01 \text{ s}^{-1}$ , the true strain shows a maximum stress, and at higher strain the stress decreases gradually, approaching a constant value. In single  $\gamma$  phase materials, such a peak stress is observable. On the other hand, in testing  $\gamma/\alpha_2$  two-phase material that includes  $\text{Ti}_3\text{Al}$ , the strain where the maximum strain appears is small, and the value of the stress is larger compared with the case of the single  $\gamma$  phase material. On

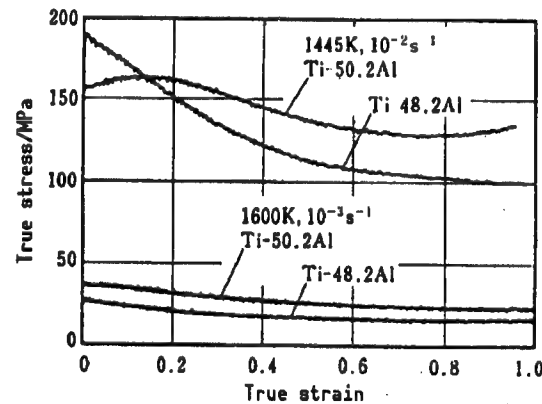


Figure 9. True Stress-Strain Relationship of TiAl Compound at High Temperatures

Compression test of Ti-50.2mol%Al (single-phase  $\gamma$ ) and Ti-48.2mol%Al (two-phase  $\gamma+\alpha_2$ ) high-temperature forged materials

the contrary, the value of the stress which is nearly constant is smaller. The characteristic situation which is seen in the true stress-strain relationship for the  $\gamma/\alpha_2$  two-phase material can be understood as follows. The yielding stress is higher for a two-phase texture than for a single phase texture. The drop in the stress due to the increase in the strain was generated by a local grain boundary slip and the progress of fine dynamic recrystallizing texture from the vicinity of the grain boundary accompanying the increase of the strain. This is clear also from an example of quenched texture.

We have already reported that the relationship between the deformation stress of TiAl compound and the temperature and the rate of strain can be satisfactorily represented by hyperbolic curves. The result of determining the maximum flow stress of TiAl compound by this method, and a summary of further investigation of the deformability are shown in Figure 10. From the result, we made it clear that the TiAl compound shows a satisfactory workability provided that the temperature is high and the rate of strain is low.

#### (4) Glass and BN Lubrication in Isothermal Forging

Using a standard ring testpiece of TiAl compound, isothermal forging was carried out with ceramic tools lubricated by hexagonal system BN powder (BN) and glass, and the friction coefficient was determined by referring to the calibration curve shown by Marle, et al. The result is shown in Figure 11. As a result of the test it was found that BN shows the most stable lubrication characteristic.

#### 4.4 Brief Summary

A testing machine for simulating high temperature working of intermetallic compounds, etc., which do not lend themselves to workings by conventional methods, was developed.

By the use of the experimentally manufactured apparatus, high-temperature deformation behavior, high-temperature workability, deformation texture, etc., were investigated, and the usefulness of the apparatus and several basic problems for the high-temperature plastic working of TiAl compound were clarified. By applying the so-called thermomechanical treatment to the compounds of this kind, it is expected in the future to improve the quality of

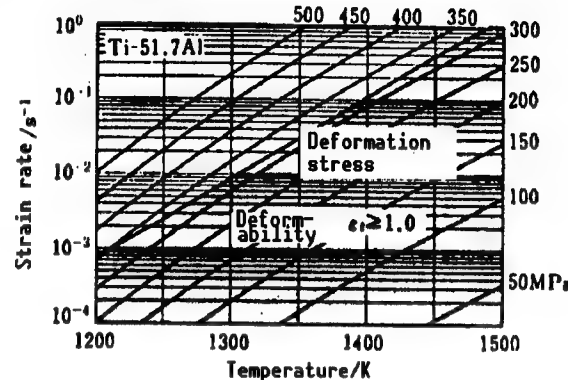


Figure 10. High-Temperature Workability Map of Ti-51.7mol%Al Melted Material

The numerical value attached to the right end of each curve shows the maximum flow stress. The deformability shows the conditions, temperature, and rate of strain for which sound compressive deformation with the true strain of greater than 1.0.

the materials. Finally, we are very grateful to Tokyo Koki Works Co., Fuji Denpa Koki Co., Hitachi Metals Co., and NKK Co., who assisted us greatly in the trial manufacture of the present apparatus.

## 5. Powder Metallurgy

Plastic working of TiAl is difficult by usual methods such as forging, hot rolling, hot extrusion, etc., even at temperatures above 1273 K. Because of this, various research to improve room-temperature ductility and plastic workability has been conducted.

One way to avoid the difficulty of the working method is to manufacture a near net shape sintered member by utilizing powder metallurgical technology. This is also a convenient method to make the texture fine. A TiAl sintered body manufactured from fine powder does not have a coarse cast structure, and may be considered macroscopically as a homogeneous bulk material. Further, a sintered body of fine crystalline grains is expected to be obtained by the use of solidified powder obtained by quick cooling. In this report, the structure of the sintered bodies and the mechanical properties for the range of room temperature to high temperature were investigated using pulverized powder, centrifugally atomized powder, and powder obtained by a combustion synthesis (SHS) method.

### 5.1 Equivalent

The pulverized powder used is the powder of -200 mesh obtained from a TiAl material manufactured by Consolidated Aeronautics Corp. (United States). The centrifugally atomized powder is solidified powder obtained by quick cooling, manufactured by high-frequency melting TiAl in the gas by the use of a calcia crucible, and pouring it over a fast rotating graphite desk. The powder is of -60 mesh centered around the powder diameter of 100~200  $\mu\text{m}$ .

The other is an SHS powder obtained by mixing Ti powder and Al powder, and by mechanically pulverizing a spongelike alloy manufactured by combustion synthesis. This is a powder formed by aggregation of fine grains.

The chemical composition of these powders is shown in Table 4. The pulverized powder contains a large amount of impurities Fe (0.02wt%) and O which are mixed during the course of pulverization. The centrifugally atomized powder contains about 0.2wt% of O, and is close to what is seen in an ordinary Ti alloy such as Ti-6Al-4V alloy. The SHS powder contains a large amount of

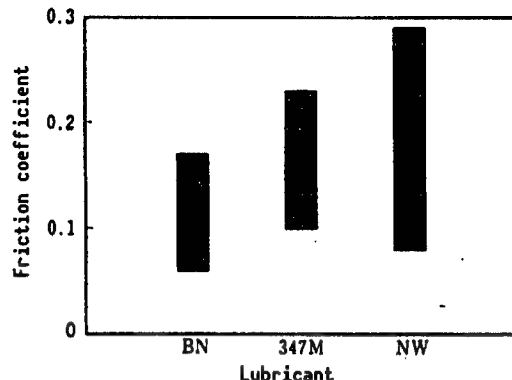


Figure 11. Lubricants and Friction Coefficient in Isothermal Forging of TiAl Compound

BN (hexagonal system boron nitride powder) 347M, and NW (glass powder) lubricants for hot working. Forged for the ranges of temperature of 1200~1500 K and the strain rate of  $1 \times 10^{-4} \sim 1 \times 10^{-2} \text{s}^{-1}$  by using sialon-forged tools.

Table 4. Chemical Analysis Values of TiAl Powders (wt%)

	Al	V	C	O	N	Mg	Ti
Pulverized powder							
	34.87	...	...	2.5	...	0.024	64.08
Centrifugally atomized powder							
D1	36.7	...	0.031	0.227	0.004	...	bal.
D4	37.5	...	0.044	0.195	0.004	...	bal.
D6	35.2	...	0.061	0.130	0.005	...	bal.
D7	33.7	2.13	0.047	0.165	0.005	...	bal.
D9	32.7	2.26	0.067	0.248	0.005	...	bal.
SHS powder							
KA	34.90	...	...	0.72	...	0.040	bal.
KB	35.63	...	...	0.78	...	0.060	bal.
KC	36.84	...	...	0.96	...	0.033	bal.

pressure, and 1473 K. For the purpose of homogenizing the sintered body, the sample was further annealed at 1273 K for 100 hours.

The mechanical properties were investigated by the compression test and the 18-mm span three-point bending test using an instron type testing machine.

## 5.2 Result and Consideration

### 5.2.1 Structure of the Sintered Body

The pulverized powder and the SHS powder which were in vacuum after CIP at room temperature contain many voids even after sintering at 1632 K, their relative densities were about 91 percent and about 70 percent, respectively, and showed two-phase layered structure of  $Ti_3Al$  and TiAl. These structures were destroyed by the succeeding HIP treatment and the homogenizing sintering at 1273 K, but the voids did not go away even after the HIP treatment of the sintered body, so that it was not possible to obtain sound bulk materials.

For the HIP sintered body a bulk material with relative density of 100 percent was obtained for both the SHS powder and the centrifugally atomized powder. Both samples consisted of fine crystal grains of about  $30\ \mu m$ , and some layered structure was observed in the former, whereas such a structure was hardly observable in the latter.

### 5.2.2 Mechanical Properties of Sintered Bodies

In the sintered body in vacuum, the compressive ductility at room temperature increases as the two-phase layered structure is destroyed by heat treatment, but ductility by the bending test was not obtained. In the compressive deformation, it was observed that cracks originate from the residual voids, propagate within the grain by linking the voids, and lead to the fracture.

impurity O, but it is considered to be reducible by improving the method of manufacture.

The sintered bodies of the pulverized powder and the SHS powder were manufactured, after formation of pressed powder by a cold isostatic press (CIP) at room temperature and 4000 atmospheric pressure, sintering them at a temperature below 1623 K. The centrifugally atomized powder and the SHS powder were vacuum sealed in stainless steel tubes and their sintered bodies were manufactured by a hot isostatic process (HIP) at 1000 atmospheric pressure (HIP) at 1000 atmospheric

In an HIP sintered body, a compressive deformation of more than 26 percent was possible at room temperature for both the centrifugally atomized powder and the SHS powder. Figure 12 shows the temperature dependence of the compressive stress of the centrifugally atomized powder (D1). The compressive stress does not decrease up to the vicinity of about 1073 K, dropping suddenly thereafter. It also shows that the curing does not change up to the vicinity of 973 K. These tendencies are similar to the result for the molten materials. Figure 13 shows the temperature dependence of the bending characteristic in vacuum of the HIP sintered body (D1) of the centrifugally atomized powder and the HIP sintered body (KA) of the SHS powder, respectively. At room temperature, both have a bending ductility of about 0.5 percent, and above 973 K the bending increases. In contrast to a ductility of greater than 15 percent at 1073 K for the former, only about 4 percent of the ductility is observable for the latter. For both, the ductility goes down at 1173 K. The corresponding fractures are shown in Photographs 2 and 3 [not reproduced]. Both exhibit cleavage at room temperature, crystal grain boundaries at 1073 K, and prepowder boundary fracture at 1173 K. The ductility at room temperature is not strongly influenced by the amount of oxygen contained in a sintered body, but it may be said that it has a large effect for cracks at crystal grain boundaries and cracks at prepowder boundaries at high-speed.

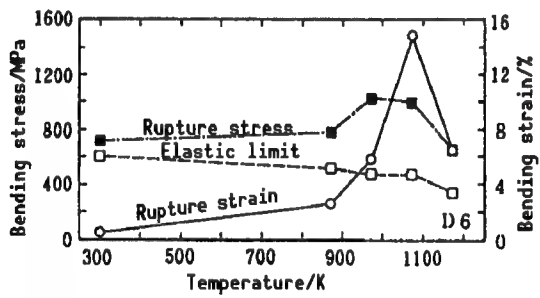


Figure 13. Bending Characteristic of HIP Sintered Body of Centrifugally Atomized Powder (D1)

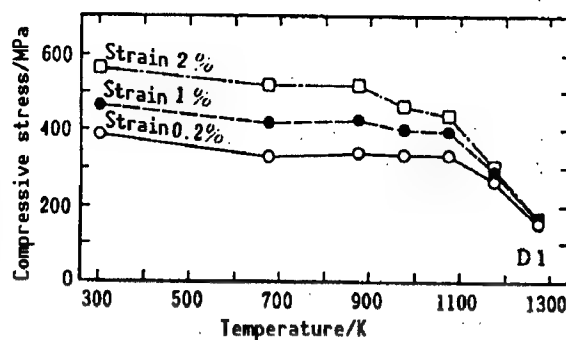


Figure 12. Temperature Dependence of Compressive Stress of HIP Sintered Body of Centrifugally Atomized Powder (D1)

Figure 13 shows the bending characteristic in vacuum of the HIP sintered body (D1) of the centrifugally atomized powder and the HIP sintered body (KA) of the SHS powder, respectively. At room temperature, both have a bending ductility of about 0.5 percent, and above 973 K the bending increases. In contrast to a ductility of greater than 15 percent at 1073 K for the former, only about 4 percent of the ductility is observable for the latter. For both, the ductility goes down at 1173 K. The corresponding fractures are shown in Photographs 2 and 3 [not reproduced]. Both exhibit cleavage at room temperature, crystal grain boundaries at 1073 K, and prepowder boundary fracture at 1173 K. The ductility at room temperature is not strongly influenced by the amount of oxygen contained in a sintered body, but it may be said that it has a large effect for cracks at crystal grain boundaries and cracks at prepowder boundaries at high-speed.

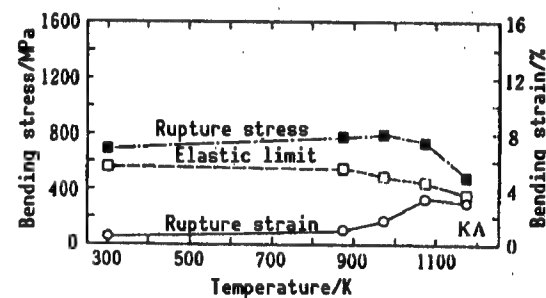


Figure 14. Bending Characteristic of HIP Sintered Body of SHS Powder (KA)

The strength and ductility of sintered bodies are affected by the environment in the atmosphere at room temperature. In the atmosphere the bending ductility and the strength are larger for the larger deformation rate, and the bending ductility and the strength in the atmosphere are smaller than in a vacuum. When delay test due to a bending load is carried out in the atmosphere with a Vickers indentation as a source of the stress concentration, crack growth over time is recognized as shown in Figure 15, and the crack face of delayed rupture showed a fracture of crystal grain boundary.

### 5.3 Brief Summary

(1) To manufacture a near-net-shape bulk material using powder metallurgical technology, green compact forming at room temperature and sintering are desirable. However, for this compound, it was impossible to obtain a sound sintered body with no voids by CIP. Neither was vacuum sintering possible, either for the pulverized powder or for the SHS powder.

(2) By HIP after vacuum-sealing the centrifugally atomized powder or the SHS powder in a stainless steel tube, it was possible to obtain a sintered body having small crystal grains and relative density of 100 percent.

(3) Both the centrifugally atomized powder and the SHS powder have a bending ductility of about 0.5 percent at room temperature in vacuum, exhibiting a cleavage fracture. The bending ductility increased with the temperature up to about 1073 K, and it dropped at 1173 K. At temperatures with high ductility, both sintered bodies exhibited a grain boundary fracture, and at high temperatures where the ductility drops, they exhibited prepowder boundary fracture.

(4) The sintered body is affected by the atmospheric environment, and it was observed that delayed puncture cracks propagate along the crystal grain boundaries.

In order to prevent the prepowder boundary rupture and improve the ductility of the TiAl boundaries at high temperatures it is necessary to subject them to sufficient heat treatment or hot processing. Further, by HIP sintering the SHS powder having small oxygen content, it is expected that a ductility similar to that of the sintered body of the centrifugally atomized powder can be obtained. A further examination of the effect of the environment on the strength and ductility at room temperature, and the effect of oxygen at high temperatures will be necessary.

### 6. Surface Modification

The atomic bonding between Ti and Al in TiAl which takes up the  $L1_0$  face-centered cubic lattice is not a typical metallic bonding, differing from that between Ti and Ti or Al and Al. It is possible to increase the bonding strength of the TiAl lattice via an element which has a strong bonding with the constituents of the crystal, introduced into the lattice. In particular, nitrogen enters the TiAl lattice as an interstitial element to form a regular lattice with higher symmetry by  $L1_0$  type  $\rightarrow$   $B1$  type, forms stable compounds by reacting with Ti and Al, and hence is expected to increase the bonding

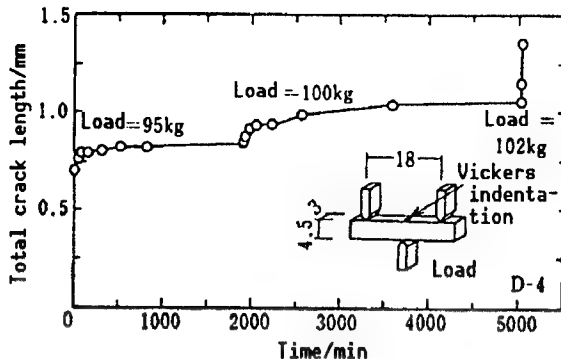


Figure 15. Growth of Delayed Rupture Crack of HIP Sintered Body of Centrifugally Atomized Powder (D1) (In atmosphere at room temperature; source of stress concentration is a Vickers indentation)

strength within the grain and at the grain boundary. Based on the above viewpoint we attempted the surface modification of the intermetallic compound TiAl by means of ion implantation; namely, the microscopic structural change and the change in the mechanical properties were investigated by implanting nitrogen ions into the surface of a TiAl sample.

### 6.1 Sample and Experimental Method

#### 6.1.1 Preparation of Sample

A button ingot of about 100 g was prepared by arc melting in an Ar atmosphere, and an ingot of about 2.5 kg was prepared by Ar plasma melting.

These materials were held for 1.8 ks in a vacuum at 1473 K to remove working strain, and were further subjected to a homogenization treatment at 1273 K for 605 ks. After specular finishing of these materials by buffering and electro-polishing, these were used as samples for ion implantation.

#### 6.1.2 Ion Implantation and Various Measurements

The implantation of  $N_2^+$  ions was carried out at room temperature under an acceleration voltage of 150 kV and a dose of  $2 \times 10^{17}$ – $1.8 \times 10^{18}$  ions/cm<sup>2</sup>. For each of the samples, the product composition distribution, concentration distribution of implanted nitrogen in the depth direction, etc., were measured by the X-ray diffraction (XRD) method, X-ray photoelectronic spectroscopy (XPS), Auger electron spectroscopy (AES), etc. Further, transmission electron microscope (TEM) and scanning electron microscope (SEM) observations were taken for the purpose of the microscope structural analysis of the implanted layer. In addition, the hardness measurement by a micro Vickers hardness meter was carried out. For the corrosion resistance test, etching was given for 30 seconds at room temperature using a corroding solution obtained by diluting a mixture of nitric and hydrofluoric acids with water. The three-point bending strength at room temperature was measured by an Instron type tension tester at crosshead moving speed of  $8.3 \times 10^{-6}$  m/s, using a narrow slip-formed (3 mm x 45 mm x 0.7 mm) sample.

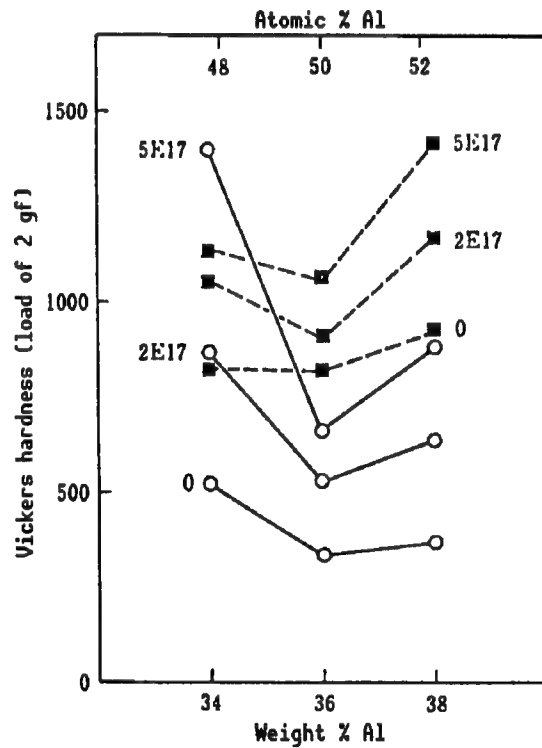


Figure 16. Hardness Change at the TiAl Sample Surface Due to Implantation of 150 kV Nitrogen Ions  
 (○ for electropolished material and ■ for buffed material)

## 6.2 Experimental Result and Consideration

### (1) Hardness Change

Figure 16 shows the relationship between the increase of the hardness and the composition of the TiAl samples with nitrogen ion implantation of  $2 \times 10^{17}$  ions/cm<sup>2</sup> and  $5 \times 10^{17}$  ions/cm<sup>2</sup>. For the electropolished material, a conspicuous minimum of the hardness is recognizable at stoichiometric composition of 50at%Al, obtaining a V-shaped curve. Such a dependence on the composition is considered due to the presence of Al lattice vacancies on the Ti-rich side and to the presence of replacement type Al atoms in the Al-rich side. The hardness is increased by nitrogen implantation, and it is two to three times the hardness of unimplanted material on both sides of the stoichiometric composition. That the increase in the hardness is larger on the Ti-rich side is considered due to the contribution to the hardening, of the stable vacancy type point defects among the point defects introduced by the ion irradiation. In the mechanically polished buffed material, the hardness increase due to nitrogen implantation is smaller on the Ti-rich side. This is considered due to canceling of hardening by the point defects caused by the dislocation lines introduced by the surface working acting as the sinks for the point defects. As in the above, the increase in the surface hardness due to nitrogen implantation is considered to be contributed by the hardening caused by the point defects introduced by the ion irradiation, in addition to the internal strain hardening by the supersaturated solid solution nitrogen and the precipitation hardening due to formation of nitrides.

### (2) Distribution of Implanted Nitrogen and Identification of Nitrides

Figure 17 is an XPS composition distribution curve obtained by the implantation of nitrogen into the Ti-48at%Al sample. For the implantation of  $5 \times 10^{17}$  ions/cm<sup>2</sup>, a maximum concentration of ~40at% is reached at a depth of ~80 nm. An example of measuring the change in the depth direction of the XPS spectrum taken to examine the bonding condition of the implanted nitrogens is shown in Figure 18. The Nls spectra after sputtering for 70 minutes which produces the maximum nitrogen concentration shows that there are peaks in the neighborhood of 396.7 eV or 397.0 eV that correspond to the bonding energy of TiN. Further, an examination of the Ti<sub>2</sub>p spectra revealed that the peaks exist at positions between the energy of metallic Ti and the bonding energy of TiN. These results in the above suggest the formation of AlN and the formation of quasi stoichiometric nitrogen compound Ti<sub>2</sub>N.

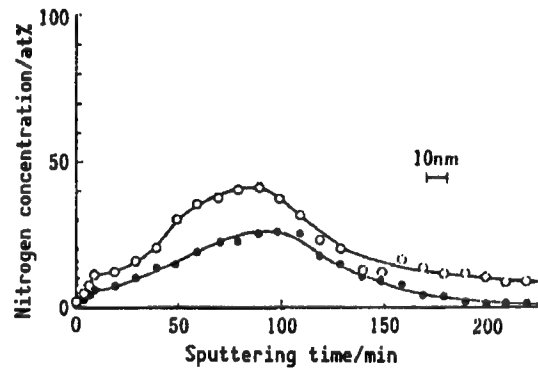


Figure 17. Depth Distribution Curve of Implanted Nitrogen  
(●  $2 \times 10^{17}$ ions/cm<sup>2</sup> and ○  $5 \times 10^{17}$ ions/cm<sup>2</sup>)

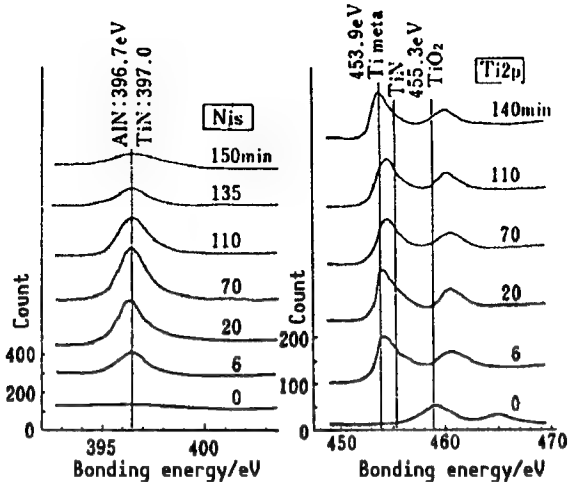


Figure 18. Depth Change of XPS Spectrum for Nitrogen Implantation of  $5 \times 10^{17}$  ions/cm<sup>2</sup>

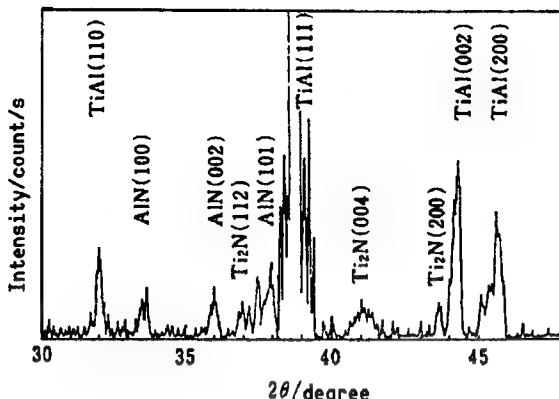


Figure 19. X-Ray Diffraction Pattern of Ti-52at%Al Sample (Implantation of  $5 \times 10^{17}$  ions/cm<sup>2</sup>)

Figure 19 is an example of the X-ray diffraction pattern obtained from a nitrogen implanted sample. Although the diffraction lines for  $Ti_2N$  and  $AlN$  were observed, the formation of  $TiN$  was not recognized. Even for a sample of heat treatment for 1.8 ks at 773–973 K in an Ar atmosphere after the implantation, it was not possible to confirm the formation of  $TiN$ . The formation of  $Ti_2N$  is not due to insufficient nitrogen, but the presence of the defects by irradiation has something to do with it.

### (3) Elimination of Surface Microcracks and Improvement of Corrosion Resistance

The microcracks that are generated by the corrosion of the surface of a buffed material are considered to be stress corroded cracks caused by the stress at the time of surface working. Photograph 4 [not reproduced] shows that the generation of the microcracks that appear in the 48at%Al material is prevented with the implantation of nitrogen (Photograph 4(b)), and the corrosion resistance is improved (Photograph 4(c)). This is considered to be the result of the action of obstruction of crack generation caused by the strong compressive stress in the neighborhood of the surface by the solid solution nitrogen, and the formation of large amounts of corrosion-resistant nitrides.

### (4) Bending Test and Rupture Behavior

A bending test was carried out to investigate the rupture behavior of the  $TiAl$  samples. Photograph 5 [not reproduced] shows the optical micrographs of the samples obtained by corroding the surface on the tension side after the rupture. In the unimplanted material, rupture occurs preferentially along the grain boundaries. On the other hand, in the ion implanted material, the rupture edge is rather smooth and the rupture penetrates through the grains, and there are observed local slips along the rupture edge and several cracks along the bending axis. In the ion-implanted material it is characteristic that no grain boundaries appear as a result of corrosion treatment, but the

above finding is an important result which shows the possibility that by ion implantation the rupture mode shifts from the grain boundary destruction to the in-grain destruction. Although there is yet no detailed explanation, it is expected that the strengthening of the grain boundaries is brought about by the modification of the grain boundary structure as a result of segregation of the implanted nitrogens to the grain boundaries or by the precipitation of the implanted nitrogens as fine nitrides.

The bending strength of the TiAl sample becomes lower than that of the unprocessed material as a result of nitrogen implantation. However, it was found that the bending strength is conspicuously recovered and improved when the bending test is given after corroding the implanted surface. In particular, for Ti-5at%Al in which ions are implanted at a relatively low level of  $2 \times 10^{17}$  ions/cm<sup>2</sup>, it was found that the bending strength of the corroded material can be improved to an extent that exceeds the bending strength of the unprocessed material. These results seem to indicate, as illustrated in Figure 20, that the bending strength is lowered with the irradiation damaged layer formed at the time of ion implantation and the oxide layer in the surface layer as the crack generation sites, but the truly modified layer by the nitrogen implantation can be made to appear on the surface side by the removal of these defect layers by corrosion, improving the bending strength. The degree of formation of the defect layer and the modified layer depends on the amount of implantation, but within the range of this experiment it is suggested that implantation of a small amount of the order of  $2 \times 10^{17}$  ions/cm<sup>2</sup> or below seems to be effective.

### 6.3 Brief Summary

For the intermetallic compound TiAl, the following effect of surface modification was observed by the implantation of nitrogen ions.

- (1) The surface hardness was increased by two to three times by nitrogen implantation.
- (2) The surface microcracks generated in the unimplanted material can be eliminated and corrosion resistance can sharply be improved.
- (3) The tendency of the bending rupture mode shifting from the grain boundary rupture type to the in-grain rupture type was observed. Further, an improvement of the bending strength was observed for a relatively low dose of implantation.

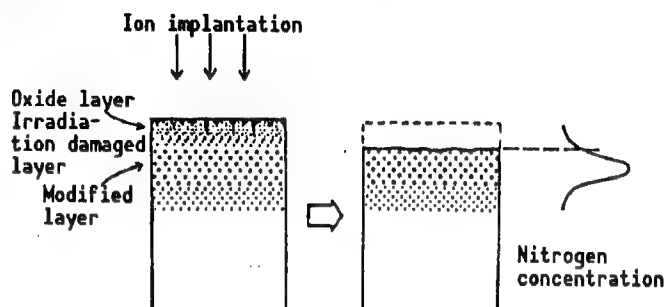


Figure 20. Schematic Diagram Showing Relationship Between Structural Change of Ion-Implanted Surface Layer and Change of Bending Strength

These effects are brought about by the introduction of internal strain or internal compressive strain due to supersaturated solid solution of the implanted nitrogens, and chemically stable Al-N and Ti-N bondings, or a uniform and fine distribution of Al nitrides and Ti nitrides.

## 7. Conclusion

This special research was carried out to establish an infrastructure to legitimize new TiAl intermetallic compounds as practical structural materials. Note that what is called basic here is meant for items that can directly be linked to practicality such as the performance or manufacturability of the materials.

As a result of this research it was predicted that the ductility at low temperatures which was the largest drawback as the material can be improved by about 3 percent in elongation. This is the value from which its use as a structural material starts to become an object of study, even according to the conventional design standards. The conclusion of the research which was carried out by active use of the alloy design techniques is that ductility can be achieved by the addition of Mn and dispersion of a small amount of  $Ti_3Al$ . The second drawback of TiAl, namely, the plastic workability at high temperatures, may be improved as a result of introduction of a simulating device of working at high temperatures. Great advances in the shape giving technology by plastic working is expected in the future along these lines. Although TiAl has an excellent high temperature strength and resistance to oxidation as a lightweight material, we attempted to improve resistance to oxidation with the attempted use at temperatures above 1073 K, and it was found that the addition of Si is effective in improving the resistance to oxidation. For melting of materials with a large amount of Ti, a vacuum arc melting furnace is ordinarily used which is suitable for melting large quantities. In order to give a flexibility to the production scale, a plasma arc melting method was developed as a method of obtaining ingots of about several kilograms. High frequency melting by a CaO crucible as a handy melting method was also studied, but there are problems in the quality of the materials obtained, and it became clear that further research is needed. On the other hand, in powder metallurgy, the combination of the cold powder pressing and sintering does not work, but it was found that a TiAl sintered body of a bulk material with a degree of filling of 100 percent can be obtained. However, there remains a problem in obtaining high quality TiAl powder. The surface modification by ion implantation was found to be effective for surface hardening and improvement of corrosion resistance. The utility of this technology depends on what purposes TiAl is used for in the future.

**Research on Properties of New Superconducting Wire Materials for Nuclear Fusion Reactor**

916C0048B Tokyo KENKYU HOKOKUSHU 12 in Japanese 1991 Issue pp 27-39

[Research on nuclear power, FY84-FY88]

**[Text] Abstract**

In this research, a testing technology for evaluating the characteristics of superconducting wire materials was developed, under conditions (superfluidic helium cooling, stress, and varying magnetic field) which simulated the environment in which the superconducting wire materials of a nuclear fusion reactor are subjected. Further, by evaluating the characteristics of various kinds of superconducting wire materials using the testing technology, the practicality as wire materials for a nuclear fusion reactor was examined.

As to the characteristic evaluating test in superfluidic helium, we developed a new superconducting alloy VTiTa which can generate a magnetic field up to 12 T by cooling with superfluidic helium. In the area of compound systems, it became clear that a V<sub>3</sub>Ga tape wire, and (Nb,Ti)<sub>3</sub>Sn and V<sub>2</sub>(Hf,Zr) superthin multiconductor wires are promising as materials for generating a magnetic field in the vicinity of 20 T in the superfluidic helium temperature region. In addition, a pressurized helium cooled device was trial manufactured to simulate the cooling operation of the actual magnet for the nuclear fusion magnet, and a simulation test was carried out.

In the characteristic evaluation test under stress, the critical temperature and the critical current of an Nb<sub>3</sub>Sn wire, obtained by the bronze method, were evaluated under a static stress. It was found that the volume ratio of the bronze matrix against the wire material strongly influences the superconductivity under stress. Further, the characteristics of superthin multiconductor NbTi, Nb<sub>3</sub>Sn, and V<sub>2</sub>(Hf,Zr) wires under repeated stress were tested. The influence of the repetitious strain load on the critical current characteristic was found to be small as long as the magnitude of the repetitious strain is within the range of reversible strain, even for the compound system wire materials which are susceptible to mechanical damage such as cracks.

In evaluating the characteristics in varying magnetic fields, we trial manufactured a device which measures the pulse loss, an energy loss which occurs in a superconductor in varying magnetic fields. Further, the alternating current loss was evaluated by measuring the magnetization for a superthin Nb<sub>3</sub>Sn multiconductor wire manufactured by composite working. As a result, it was made clear that the Nb<sub>3</sub>Sn wire material has small ac loss, and is promising as a wire to be used in varying magnetic fields.

Moreover, as a new superconducting wire material for nuclear fusion reactor, the manufacturing method of the Nb<sub>3</sub>Sn wire material that shows stabilized characteristics under stress and the basic research for manufacturing wire material of YBaCuO oxide superconductor were carried out by utilizing hot or cold isostatic press.

## 1. Introduction

In nuclear power generation, whose history dates about 30 years, energies emitted in the fission reaction of heavy atomic nuclei are utilized. On the other hand, attempts to realize the fusion reaction of light nuclei as a power reactor are actively being pursued in many countries. In the Tokamak type fusion reactor, the most advanced so far developed, a high magnetic field is utilized for confining an extremely high-temperature plasma. If normally conducting copper magnets are used to generate a high magnetic field, an enormous amount of energy that exceeds the output from the nuclear fusion reactor will be consumed. Accordingly, in the actual reactor it is indispensable to use superconducting magnets which require almost no power consumption.

The superconducting magnet considered in the stage of experimental reactor or an actual fusion reactor is much larger compared with a magnet of laboratory scale, is more than several meters in diameter, generates a magnetic field higher than 12 T (tesla), etc. As a result, a gigantic electromagnetic force acts on the superconducting wire material wound around the coil. In this case, a high pulse magnetic field—in addition to a stationary magnetic field—works so that a repetitious force is applied and an energy loss (pulse loss) due to variations of the magnetic field takes place. Further, since the superconducting wire is used in the nuclear fusion reactor in a high magnetic field which is close to the limit, it is necessary to examine the magnet, not in ordinary liquid helium (4.2 K), but in a pressurized superfluidic helium (near 1.8 K) where the characteristics of the magnet are improved. Moreover, irradiation with a large amount of neutrons generated in the nuclear fusion reaction also markedly influences the superconducting characteristics. For the above-mentioned reasons, we hope the superconducting wire material for nuclear fusion reactors can satisfy the following conditions:

- (1) The critical current density at high magnetic fields is high for the temperature range of 4.2~1.8 K.
- (2) The superconducting characteristics are stable under the presence of a stress, in particular a repetitious stress.
- (3) The pulse loss in a varying magnetic field is small.

(4) The degradation of the superconducting characteristics by the irradiation of neutron beams is small.

The superconducting wire materials put to practical use are NbTi alloy, Nb<sub>3</sub>Sn compound, and V<sub>3</sub>Ga compound. In various countries, NbTi and Nb<sub>3</sub>Sn which have low manufacturing cost and satisfactory performance are being examined for nuclear fusion reactors.

However, NbTi has insufficiently high magnetic field characteristics, though the resistance to stress and neutron irradiation is excellent, and the upper limit of the generated magnetic field is 8-9 T. On the other hand, Nb<sub>3</sub>Sn and V<sub>3</sub>Ga have excellently high magnetic field characteristics and a magnetic field generation of 12-18 T can be expected, and it is said that they have mechanical brittleness of chemical compounds and have problems in resistance to neutron irradiation. None of the superconducting wire materials that are now put to practical use can be called suitable for the manufacture of magnets for a nuclear fusion reactor, thus the development of new superconducting wire materials having high performance for nuclear fusion reactors is awaited.

In our Institute, we have been studying optimization of the manufacturing conditions of the wire materials and other problems in order to improve the high magnetic field characteristics of superthin multiconductor wire materials, and the development of new alloy system wire materials. In the compound system, we studied using V<sub>2</sub>Hf system Laves phase compound—which has a resistance to neutron irradiation more than 10 times that of Nb<sub>3</sub>Sn or V<sub>3</sub>Ga and has superior high magnetic field characteristics—as a wire material, and succeeded in the trial manufacture of superthin multiconductor wire of V<sub>2</sub>(Hf,Zr) by a compound working method. On the other hand, we studied the effect of adding a third element to improve the high magnetic field characteristics of superthin multiconductor wire Nb<sub>3</sub>Sn, and showed that the addition of Ti is particularly effective in improving the characteristics in high magnetic fields. In addition, we developed new in-situ type wire materials which have extremely stable characteristics under stress, various new wire materials of superthin multiconductor type which have small pulse loss. However, what kind of behavior these new wire materials will show under severe conditions in which the superconducting magnet will be placed in the actual nuclear fusion reactor has not been clarified. Moreover, optimization of the performance of the wire material in such an environment is a problem yet to be solved.

The object of this research was the development of the technology for the evaluation test of the superconducting wire materials under the nuclear fusion reactor environment, and examination of the possibility of putting to practical use the various kinds of new superconducting wire materials developed in our laboratory by applying the testing technology developed.

## 2. Evaluation Tests in Superfluidic Helium Temperature Region

It has been reported that by cooling the NbTi alloy wire material—whose use is limited to the magnetic field generation of below 9 T at 4.2 K—to 1.8 K the upper critical magnetic field H<sub>C2</sub> can be raised sharply so that it becomes possible to generate a magnetic field of about 12 T. For this reason, cooling

with superfluidic helium and the use of alloy wire material for the fusion reactor is now being examined in many countries. Under these circumstances, this research was aimed at developing an evaluation and testing technology of the superconducting wire materials in superfluidic helium, and carrying out evaluation of various superconducting wire materials for a fusion reactor.

### 2.1 Alloy System Superconducting Wire Material

Of the alloy system superconducting wire materials known so far, the NbTi alloy shows the best superconducting characteristics at 4.2 K. However, for use in the temperature range of the superfluidic helium of around 2 K, it is possible to find alloys whose characteristics are comparable or even superior to those of NbTi. In this research, as an alloy with such possibilities we focused our attention on VTi alloy which is known to have a theoretical value of 20 T for  $H_{c2}$  at 0 K, and exceeds the value for NbTi, and developed an alloy wire material which is suited for use in the superfluidic helium temperature region, by adding a heavy element (Ta) which can weaken the Pauli paramagnetic effect which is suppressing  $H_{c2}$ , and has the effect of raising  $H_{c2}$ .

Figure 1 shows the change with temperature of  $H_{c2}$  for V-60at%Ti(0,3,6,9)at%Ta and Nb-(56,60)at%Ti. The value of  $H_{c2}$  was measured at the measured constant current density of 10 A/cm<sup>2</sup> by the resistance method, and it was defined as the magnetic field that corresponds to one-half the resistance when it made transition to normal conductivity. For VTi, by the addition of Ta  $H_{c2}$  showed only a small increase at 4.2 K, but it was sharply increased at 2.0 K. The value of  $H_{c2}$  for V-60at%Ti-9at%Ta exceeded that for Nb-60at%Ti at 2.5 K, and the extrapolated value at 0 K was 16.3 T. This value is comparable to the maximum value reported (for NbTiTa) for the alloy system superconducting materials. By the addition of Ta to VTi the  $H_{c2}$  at 4.2 K and below is improved markedly, and it is anticipated that it will be a superconducting material suitable for use in the superfluidic helium temperature region (in the vicinity of 2 K). In the future, research on raising the critical current density  $J_c$  is needed.

### 2.2 Compound System Superconducting Wire Materials

Figure 2 shows the magnetic field dependence of  $J_c$  per total cross sectional area of the wire at 4.2 K and 1.8 K for the V<sub>3</sub>Ga tapes by the surface diffusion

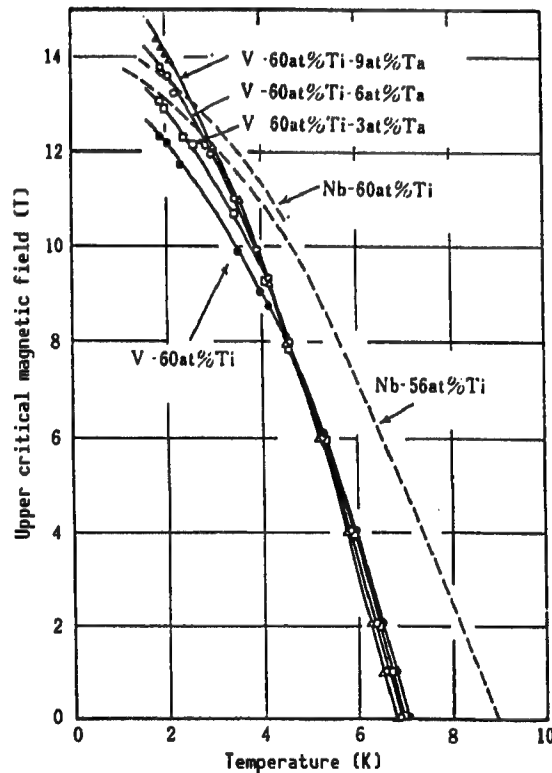


Figure 1. Comparison of Changes With Temperature of the Upper Critical Magnetic Field of VTi Alloy and NbTi Alloy

method and the in-situ method, a superthin multiconductor  $(Nb, Ti)_3Sn$  wire by the bronze method, and a  $V_2(Hf, Zr)$  superthin multiconductor wire by the compound working method. For all of the wire materials it can be seen that the  $J_c$  per total cross-sectional area of the wire material is increased markedly by going from 4.2 K to 1.8 K by cooling. The magnetic field characteristic of  $J_c$  at 1.8 K roughly corresponds to the result of shifting the magnetic field characteristic of  $J_c$  at 4.2 K by the percentage of increase in  $H_{c2}$  for each wire material to the high magnetic field side, indicating that lowering the temperature is very effective for improving the high magnetic field characteristics of  $J_c$ . The magnetic field for which  $J_c$  per total cross-sectional area of the wire material at 1.8 K equals  $2 \times 10^4 A/cm^2$  is 21.5 T for a  $V_3Ga$  tape by the surface diffusion method, and is 19.5 T for a superthin multiconductor  $(Nb, Ti)_3Sn$  wire and a superthin multiconductor  $V_2(Hf, Zr)$  wire, which shows that these wire materials show promise in generating a magnetic field of 20 T in the superfluidic helium temperature region.

### 2.3 Trial Manufacture of Pressurized Superfluidic Helium Cooling Device

For the characteristic evaluation test in superfluidic helium described above, the superfluidic helium was obtained by decreasing the ordinary liquid helium using a pump. However, when cooling the actual fusion reactor magnet by superfluidic helium, the state of reduced pressure with pumps is unstable so that cooling with pressurized superfluidic helium must be adopted. This is because the state is more stable and has excellent cooling efficiency. For this reason, a device cooled with pressurized superfluidic helium which can be used for characteristic test of superconducting wire materials in pressurized superfluidic helium and for cooling a superconducting magnet was designed and trial manufactured, and carried out a cooling test of a simulated magnet. A diagram showing the principle is shown in Figure 3. This device can generate pressurized superfluidic helium of temperature of 1.8 K in a 30 cm-diameter space by the use of a vacuum pump that has evacuation power of 3000 l/min.

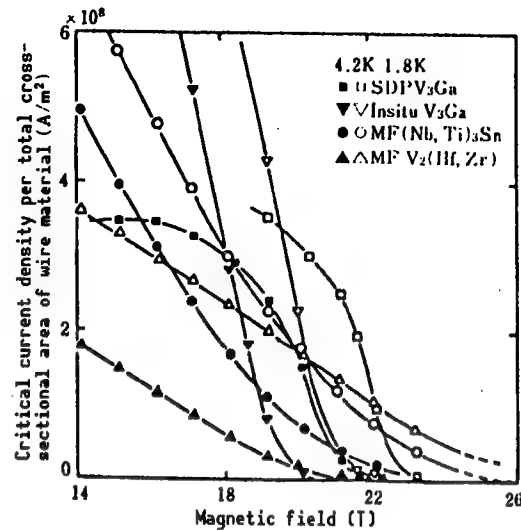


Figure 2. Magnetic Field Dependence of Critical Current Density per Total Cross-Sectional Area of Wire Material of Various Kinds of Compound System Superconducting Wire Materials, at 4.2 K and 1.8 K

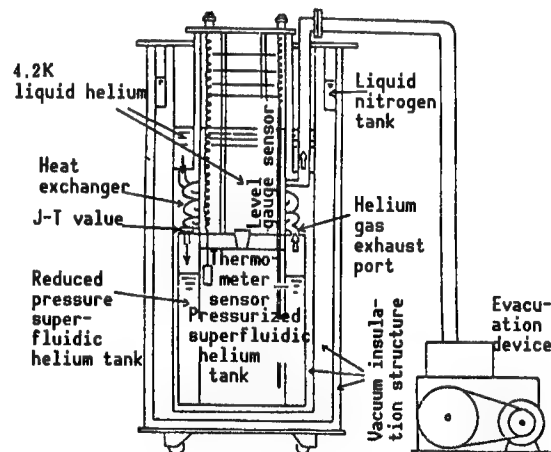


Figure 3. Diagram Showing Principle of Cryostat for Pressurized Superfluidic Helium

The simulated cooling test was carried out by incorporating a simulated stainless steel magnet 30 cm in diameter and 30 cm high in the cooling device. In addition, in order to simulate the coil current, a current of 400 A or 200 A, is introduced to the pressurized superfluidic helium, tank and a cooling test was also carried out for the case when such a heat source exists in the tank. As a result, we succeeded in cooling it from 4.2 K to 1.7 K in about 1.5 hours. By incorporating a superconducting magnet in a cryostat, it is possible to realize a state close to the environment of the actual fusion reactor, and moreover, to carry out a characteristic test of a superconducting wire material in it.

### 3. Characteristic Evaluation Test Under Stress and Strain

When a superconducting wire material is used for a magnet, the stresses applied to the superconducting wire material include mainly the bending and tension at the time of winding, thermal stress due to cooling to the magnet operating temperature, and the electromagnetic force at the time of magnetization. A superconducting magnet for a fusion reactor will become an extremely large high magnetic field magnet which has a coil diameter of several meters. Because of this, in such a large magnet, the electromagnetic force whose magnitude is proportional to the coil radius becomes especially large, so that the deterioration of the superconducting wire material due to stress is of concern. Therefore, this research was aimed at creating a testing technology that can evaluate the characteristics of the superconducting wire materials under stress and strain.

#### 3.1 Characteristic Evaluation Tests Under Static Stress and Strain

At present, the most promising compound system superconducting material is the Nb<sub>3</sub>Sn wire material by the bronze method. In a wire material manufactured by the bronze method, there is a big difference in the thermal contraction coefficient of the bronze matrix and Nb<sub>3</sub>Sn so that at the magnet operating temperature of 4.2 K, Nb<sub>3</sub>Sn receives a compressive stress from the bronze matrix. The compressive stress strongly affects the superconducting characteristic when an external tensile stress is applied to the wire material. In order to investigate the influence of the bronze matrix on the stress and strain effect, wire materials with various values of the bronze/Nb volume ratio were prepared. For these wire materials, the critical temperature T<sub>c</sub>, the critical current I<sub>c</sub> when the bronze matrix is removed were measured under an external tensile stress.

Figure 4 shows a schematic diagram of a sample holder for measuring T<sub>c</sub> of a superconducting wire material under a tensile stress. In this system, T<sub>c</sub> was measured by the four-terminal resistance method. On the 30-mm end of a sample about 11 cm in length was soldered to a copper block fixed to the bottom part of the sample holder, and the other 30-mm end was soldered to a copper block linked to a draw bar. These copper blocks also play the role of electrodes. A voltage lead wire was soldered to the sample with a spacing of about 5 mm. Tensile stress was applied manually. The strain was obtained by measuring the displacement of the draw bar with a dial gauge and was calibrated by a strain gauge. The temperature of the sample was changed by adjusting the output of

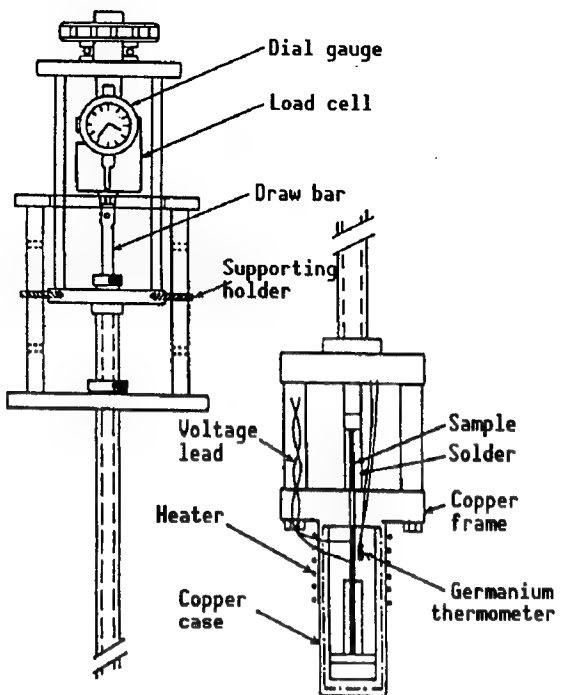


Figure 4. Schematic Diagram of Sample Holder for Critical Temperature Measurement Under External Tensile Stress

the heater of manganese wire wound around a copper case that surrounds the sample, and the distance between the sample and the liquid helium level.

Figure 5 shows a block diagram for a device for measuring  $I_c$  of a superconducting wire material under tensile stress. The details of the device will be presented in the item for evaluation tests of characteristics under repeated stress given below.

The sample is prepared as follows. Compound bodies (with the bronze/Hb volume ratios of about 3/1, 5/1, and 9/1) obtained by inserting Nb into Cu-7at%Sn alloy pipes (outer diameter 6 mm; inner diameters 3.1 mm, 2 mm, and 1.6 mm, respectively) were worked to wires with an outer diameter of 0.5 mm while giving them intermediate annealing at 600°C. By vacuum-sealing these wires in quartz cylinders and heat treating for 48 hours at 750°C,  $Nb_3Sn$  layers with a thickness of 5-6  $\mu m$  were formed.

Figure 6 shows the  $T_c$  characteristic of wires with bronze/Nb ratio of 9/1 under tensile stress. The value of  $T_c$  increases

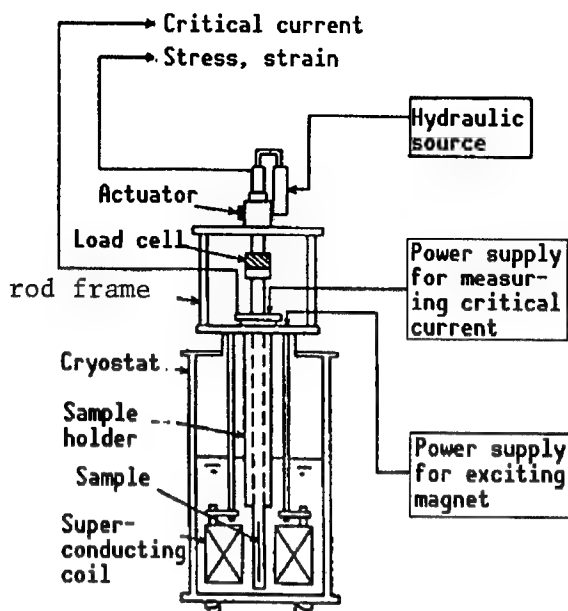


Figure 5. Block Diagram for Critical Current Measurement Device Under Tensile Stress

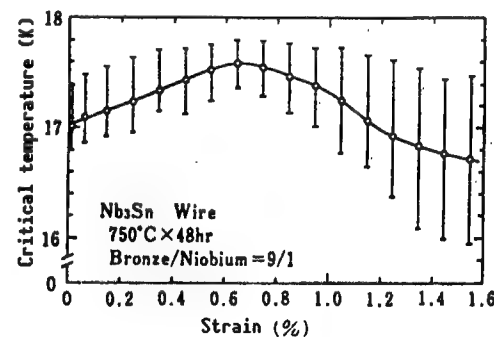


Figure 6. Change in Critical Temperature of  $Nb_3Sn$  Wire Materials of Bronze/Nb Volume Ratio of 9/1 Due to Externally Applied Tensile Stress

initially with the strain, and falls down after reaching a maximum. The initial increase of  $T_c$  is believed to be due cancellation of the compressive stress in the  $\text{Nb}_3\text{Sn}$  layer by the thermal contraction of the bronze matrix, by the externally applied tensile stress. Namely, it is believed that the  $\text{Nb}_3\text{Sn}$  layer is applied a compressive stress up to the maximum strain, and a tensile stress is applied for the strain beyond that. The  $T_c$  of  $\text{Nb}_3\text{Sn}$  decreases with both a compressive stress and a tensile stress. In addition, the midpoint of transition showed a similar rate of decrease for the strain on both the compression side and the tension side. The width of the transition increases rapidly when the strain passes 0.8 percent, and this is believed caused by a nonuniform strain generated in the  $\text{Nb}_3\text{Sn}$  layer by a nonhomogeneous plastic deformation of the bronze matrix.

Figure 7 shows the strain dependence of the midpoint of the transition of  $T_c$  of samples with bronze/Nb ratios of 3/1, 9/1, and 15/1. The values in the unstrained states prior to the application of an external tensile stress were 17.55 K, 17.05 K, and 16.95 K for samples of 3/1, 9/1, and 15/1 bronze/Nb ratio, respectively, showing that the value decreased with the increase of the ratio. With the application of an external tensile stress  $T_c$  increased with the stress for all samples, and decreased after attaining a maximum. The values of the stress that show the maximum  $T_c$  values were 0.4 percent, 0.64 percent, and 0.75 percent for samples with the ratios of 3/1, 9/1, and 15/1, respectively, showing an increase with the increase in the bronze/Nb ratio. Figure 8 shows the strain dependence of the critical current of the samples with the bronze/Nb ratios of 3/1, 5/1, 9/1, and 15/1, normalized by the value  $I_c$  (t<sub>0</sub>, 4.2 K) in the unstrained state prior to the application of the external tensile stress. Analogous to the case of  $T_c$ ,  $I_c$  increased initially with the increase in the strain, and decreased after attaining a maximum, for all samples. In addition, the value of the strain which gives the maximum value of  $I_c$  increased with the increase of the bronze/Nb ratio.

The value of the strain which gives a maximum  $T_c$  or  $I_c$ , namely, the compressive strain  $\epsilon$  generated in the  $\text{Nb}_3\text{Sn}$  layer, is with the increase in the bronze/Nb ratio.

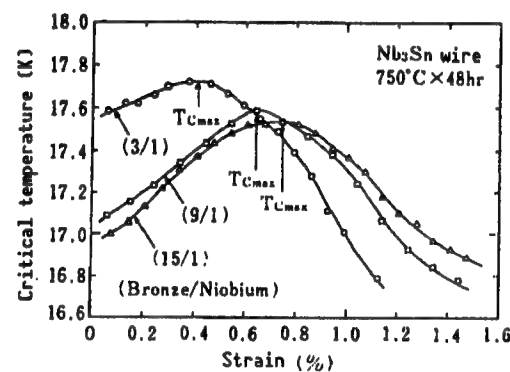


Figure 7. Change of Midpoint of Critical Temperature of  $\text{Nb}_3\text{Sn}$  Wires Having Various Volume Ratios of Bronze/Nb Due to External Tensile Stress

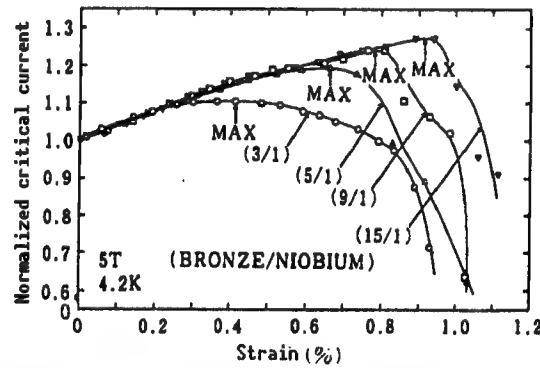


Figure 8. Change in Critical Current of  $\text{Nb}_3\text{Sn}$  Wires Having Various Volume Ratios of Bronze/Nb Having Externally Applied Tensile Stress

However, if one assumes that  $\epsilon$  is due to the elastic deformation of bronze, Nb<sub>3</sub>Sn, and Nb which are the constituent elements of the wire which forms a composite material, then it is given from the balance of the forces of Nb<sub>3</sub>Sn and Sn by

$$\epsilon = \Delta\alpha \Delta T (E_m E_c) (R^{-1} + E_m/E_c)^{-1}$$

In this equation,  $\Delta\alpha$  is the difference between the thermal absorption coefficients of bronze and Nb<sub>3</sub>Sn,  $\Delta T$  is the temperature difference in the heat treatment temperature of Nb<sub>3</sub>Sn and 4.2 K,  $E_m$  is the Young's modulus of bronze,  $E_c$  is the Young's modulus of Nb, and  $R$  is the volume ratio of bronze to Nb. Further, it is assumed here that the thermal contraction coefficient and the Young's modulus are equal for Nb<sub>3</sub>Sn and Nb. As shown in Figure 9, the computed value and the measured value agreed qualitatively. That the difference between the computed and measured value is with the decreasing value of  $R$  is believed due to the fact that the strength of bronze decreases with the decrease of the volume ratio of bronze, and plastic deformation takes place during the time it is cooled from the temperature of heat treatment to 4.2 K.

What is presented in the above is the result of measuring changes in the superconducting characteristic for the case of applying an external tensile stress to the wire. Next, the result of measurement of  $I_c$  before and after removal of the bronze matrix by etching in the magnetic field up to 21 T is shown in Figure 10. As can be anticipated from the value of  $T_c$  in the unstrained state prior to the application of an external tensile stress, the sample with the bronze/Nb ratio 3/1 showed  $H_{c2}$  which is higher by several tesla than that of the sample with the ratio 15/1. With the removal of the bronze matrix the values of  $H_{c2}$  and  $I_c$  increased sharply for both samples, and the value of  $H_{c2}$  for the sample with the ratio of 15/1 approximately equalled that of the sample with the ratio 3/1.

The superconducting characteristic of Nb<sub>3</sub>Sn wires with different bronze/Nb ratios was investigated by applying an external tensile stress or by removing the bronze matrix, and it was made clear that the size of the volume ratio of the bronze matrix sharply influences the superconducting characteristic of the Nb<sub>3</sub>Sn wires.

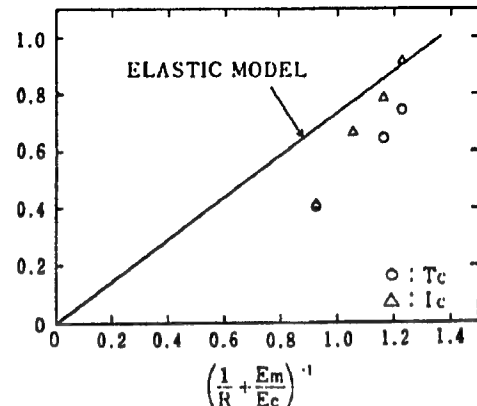


Figure 9. Relationship Between Compressive Strain Generated in Nb<sub>3</sub>Sn Wires at 4.2 K, and Bronze/Nb Volume Ratio R, Young's Modulus  $E_m$  of Bronze, and Young's Modulus  $E_c$  of Nb

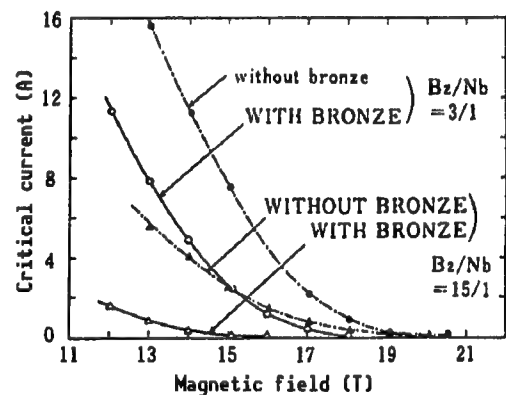


Figure 10. Magnetic Field Characteristic of Critical Current Before and After Removal of Bronze Matrix in Nb<sub>3</sub>Sn Wires With Bronze/Nb Volume Ratios of 3/1 and 15/1

### 3.2 Characteristic Evaluation Tests Under Repeated Stress

The electromagnets of a Tokamak type fusion reactor which is the most advanced at the present time consist of a toroidal magnet for keeping the plasma in doughnut shape and a poloidal magnet for heating and stabilizing the plasma. The toroidal magnet is operated by a direct current. Since the diameter of the coil is large, reaching 8~12 m, and the maximum magnetic flux density is also high, about 12 T, it is necessary to have a structure that can withstand a huge electromagnetic force. On the other hand, the poloidal magnet has a smaller magnetic flux density than that of the toroidal magnet, but it is a large pulse magnet for which is required a fast magnetic flux change of about 10 T/sec; thus a coil structure which can withstand mechanical fatigue of about 100,000 repetitions of strain is required. Accordingly, in order to use a superconducting wire material as the wire material for a fusion reactor magnet, it is necessary to investigate the change in the superconducting characteristic of the wires not only for a static load but also for a repetitious load.

As a device for evaluation tests of the wires for a repeated load, we developed a compact, handy device based on experience in developing the test method for characteristics evaluation for the conventional application of a static load. Although the conventional device uses the system of applying a load to a testpiece by means of a lever, this device has a load frame assembled on a cryostat, an actuator, and applies a repeated load by means of an electrohydraulic servo mechanism. In addition, workability is also improved such as facilitating the bringing in and out of a sample holder from the cryostat by making the load frame turnable. The measuring method was to examine the change of  $I_c$  by applying a magnetic field of 6~5.5 T by a split magnet perpendicularly to a sample held in vertical direction in liquid helium at 4.2 K, while applying a repeated load via draw bar of the sample holder by means of an electrohydraulic fatigue test machine. The length of the sample is about 17 cm, and the portions of 40 mm from its respective ends are soldered to the respective copper blocks to form chucks for the sample. With these chucks of solder, no slip of the chucking parts up to a load of 30 kg-weight for a sample 0.6 mm in diameter was seen. One of the copper blocks was fixed to the bottom part of the sample holder and the other was linked to the draw bar. These copper blocks also served as current terminals. A voltage lead wire was soldered to the sample with an interval of 20 mm, and  $I_c$  was defined as the current value where a voltage of 1  $\mu$ V per centimeter is generated. The strain was determined by measuring the displacement of the draw bar with a differential transformer attached to the fatigue testing machine, and was calibrated by a strain gauge stuck on the tape-shaped sample. The evaluation test for characteristics under the repeated load was done by applying a load of sinusoidal waveform, of displacement controlled and zero stress-tensile stress mode, at a repetition rate of 0.5 or 10 Hz, and after a repetition of a predetermined number of times, the change in  $I_c$  was measured under the state of application of the load. The fracture of wires ruptured by the repetitious application of the load was observed by a scanning electron microscope to examine the connection between the fine structure and the superconducting characteristic. In this research, an evaluation test was carried out for three kinds of wire materials, namely, NtTi and Ti-doped Nb<sub>3</sub>Sn obtained by the bronze

method as the representative wires of the alloy system and the compound system superconducting materials, respectively, and  $V_2(Hf, Zr)$  which is especially promising as the wire material for a fusion reactor.

Figure 11 shows the dependence on the static and repeated strains on  $I_c$  of the NbTi wire. First, when a static tensile stress is applied,  $I_c$  starts to decrease along with the load, and it decreased uniformly with the increase of the stress. With a strain of 3 percent,  $I_c$  was reduced to about 70 percent of the value for the unstrained state. The value of  $I_c$  was reversible within the measured range of strain of 3 percent, without showing permanent deterioration. Next, the evaluation of the characteristic under the existence of a repetitious load was carried out as follows. First, a strain of 0.7 percent is loaded to a separate testpiece of the same NbTi wire. The relationship between the strain and  $I_c$  in this case corresponds to the point "a" in Figure 11(a). When the load is removed, the wire showed a plastic strain of 0.26 percent. Next, a repeated strain between stresses of 0.26 percent (corresponds to no load) and 0.7 percent was applied  $10^5$  times. The application of the repeated strain was given at a repetition rate of 0.5 Hz up to 1000 times, and at a rate of 10 Hz beyond 1000 times. The measurement of  $I_c$  was taken by examining the change from the value of  $I_c$  when a strain of 0.7 percent is applied, measured periodically by interrupting the load test of the repeated strain. The result of applying a larger strain in such a test is shown in Figure 11(b). As shown in the figure, none of the strain levels was caused by a degradation of  $I_c$  due to the repeated strain observed. A sample for the repeated strain between 0.26 percent and 0.7 percent was ruptured by fatigue after  $9 \times 10^4$  times, and a sample for the repeated strain between 0.34 percent and 1.1 percent was ruptured after  $3 \times 10^4$  times.

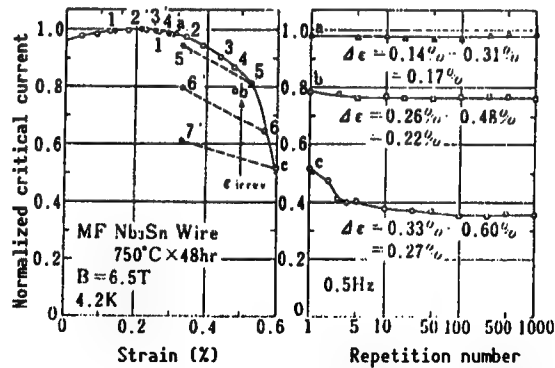


Figure 12. Critical Current Characteristic of  $Nb_3Sn$  Wires Under Static or Repeated Stress

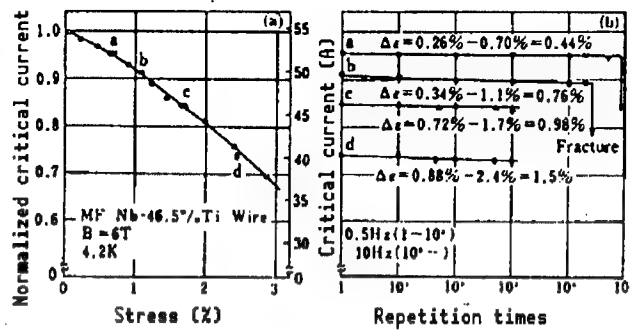


Figure 11. Critical Current Characteristic of NbTi Wire Under Static and Repetitious Stresses

Figure 11(b) shows the critical current characteristic of NbTi wire under static and repetitive stresses. The graph plots Critical current [A] (y-axis, 30 to 55) against Repetition times (x-axis, logarithmic scale from 1 to  $10^5$ ). It shows a series of points corresponding to different strain ranges. The points are labeled with their respective strain ranges:  $\Delta\epsilon = 0.26\% - 0.70\% = 0.44\%$ ,  $\Delta\epsilon = 0.34\% - 1.1\% = 0.76\%$ ,  $\Delta\epsilon = 0.72\% - 1.7\% = 0.98\%$ , and  $\Delta\epsilon = 0.88\% - 2.4\% = 1.5\%$ . A horizontal line labeled 'Fracture' indicates the point where the critical current drops to zero.

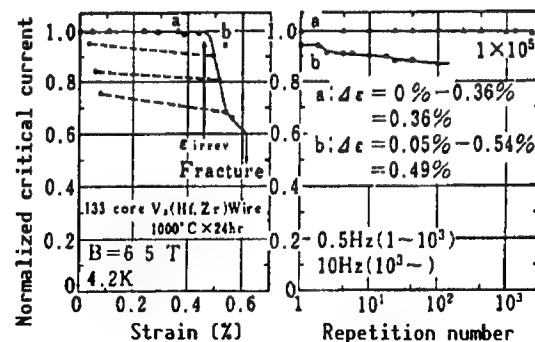


Figure 11. Critical Current Characteristic of NbTi Wire Under Static and Repetitious Stresses

As to the compound system superconducting material, from the research on evaluation under a conventional static strain, it was found that the  $I_c$ -static strain characteristic can be divided into two concerning the strain range. When the load strain is small,  $I_c$  shows a behavior which is reversible with respect to the strain (range of reversible strain), and the value of  $I_c$  is determined mainly by the strain dependence of  $H_{c2}$  of the superconducting wire material. When the load strain exceeds a certain value,  $I_c$  starts to permanently deteriorate (irreversible strain range). This is caused by fine cracks generated in the superconducting compound layer because of the mechanical brittleness of compound materials. Figures 12 and 13 show the test results for  $I_c$  for  $Nb_3Sn$  and  $V_2(Hf,Zr)$  wires under static or repetitious stress. Both  $Nb_3Sn$  and  $V_2(Hf,Zr)$  wires showed similar behavior in the reversible and irreversible strain ranges. In the reversible strain range determined by the evaluation test of characteristics under a static strain, no deterioration of  $I_c$  due to the repeated load was observed. In the irreversible strain range,  $I_c$  deteriorated initially with the increase in the number of repetitions. However, the progress of this deterioration accounted for by the first 10~100 repetitions, and beyond that the value of  $I_c$  settled at a constant value.

From the above measurements, it was found that the loading of a repeated stress does not seriously affect the characteristics of the superconducting wires except for the problem of deterioration of stabilized copper. In particular, it became clear that even in the compound system wire materials that are susceptible to mechanical damage such as cracks, the repeated stress will not give rise to a large deterioration of the characteristics provided that its magnitude is limited within the range of reversible strain.

#### 4. Characteristic Evaluation Tests in Varying Magnetic Fields

If there is no variation in the magnetic field, a superconductor has zero electric resistance below  $H_{c2}$  so that there is no energy loss, but if there is a change as in a pulse magnetic field, there is an energy loss due to the following:

- (1) Hysteresis of motion of the magnetic flux line within the core of the superconducting part of the wire.
- (2) In a superthin multiconductor wire, separation between the conductors is small so that coupling of currents is generated, and a current flows in the normally conducting portions between the conductors.
- (3) An eddy current is generated in stabilized copper in the periphery of a superconducting conductor.

When the rate of change of a magnetic field is large, these losses become significant which in turn generates a large quantity of liquid helium and destabilizes a superconducting magnet. In the poloidal magnet of the Tokamak type fusion reactor the variation with or the rate of variation of the magnetic field is large. How to suppress the loss to a low level is a problem

to be solved. In this research we tried to establish a basic technology for measuring the energy loss under varying magnetic fields, for various superconducting wires for a fusion reactor.

#### 4.1 Trial Manufacture of Pulse Loss Measuring Apparatus

Figure 14 shows the circuitry of a trial manufactured pulse load measuring apparatus. The external magnetic field to be applied to a measurement sample is generated by partially adapting the existing instantaneous high magnetic field generator, and discharging the energy stored in its capacitor bank to the field coil (copper wound solenoid type and liquid nitrogen immersed). It is characteristic that the magnetic field in which a sample is set has a large value of 45 mm, and a strong magnetic field up to 11 T can be applied to the sample instantaneously. The magnetic field is applied approximately sinusoidally, and becomes a single pulse with a width of one-half period. The sample is made into spiral form and is placed at the central part of the magnet. The pulse loss is determined by integrating the voltage generated by the pickup coils placed on the outside and the inside of the sample, and by computing its product with the waveform of the magnetic field. The successive recording of the data and data processing are carried out digitally by computer. It should be mentioned that this apparatus was designed to allow experiments concerning slow change of magnetic field by combining with the existing superconducting magnet, for the purpose of separation and extraction of the component due to hysteresis in the pulse loss.

#### 4.2 Magnetization of Superthin Multiconductor Nb<sub>3</sub>Al Wire

The compound Nb<sub>3</sub>Al has a critical magnetic field higher than 40 T that is superior to Nb<sub>3</sub>Sn and an excellent stress characteristic, and shows great promise as a suitable superconducting material for a nuclear fusion reactor. The technology for making practical wires includes the powder metallurgical method of packing the mixed powder of Nb and Al and processing it, the jelly roll method in which foils of Nb and Al are stacked alternately and the laminate is processed by rolling it like a jelly roll, etc. However, sufficient superconducting characteristics cannot be obtained, and there are problems regarding stability and mechanical properties. In our laboratory we recently succeeded in the trial manufacture of a superconducting wire which has a  $J_c$  that exceeds  $10^5 \text{ A/cm}^2$  at 10 T by cold processing a large number of bundles of composites of Nb tube and Al alloy bar. This wire is made of an extremely thin Nb<sub>3</sub>Al core of about 0.1  $\mu\text{m}$ , and it is expected to have extremely small ac loss due to magnetic hysteresis. We evaluated the ac loss by measuring the magnetization of the Nb<sub>3</sub>Al wire manufactured by the above method, and examined it as a possibility for use in a fusion reactor.

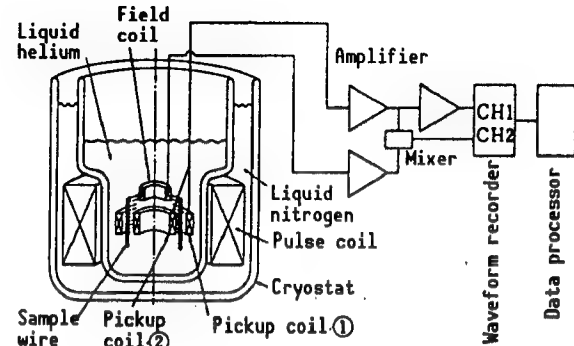


Figure 14. Circuit Diagram for Measuring Pulse Loss

The wire used for the measurement is a multiconductor wire that includes about 1.8 million lines of Nb<sub>3</sub>Al cores in an Nb matrix. The method of manufacturing the wire is to repeat the process of extruding a composite body obtained by inserting Al-lat%Cu-lat%Ge alloy conductor in an Nb matrix, and further inserting about 120 lines of this single conductor wire to an Nb tube and extruding it. The final wire diameter of 0.5 mm, 0.75 mm, and 1.0 mm were selected, and the heat treatment for manufacturing Nb<sub>3</sub>Al was conducted for 70 minutes, 4 hours, and 20 hours at 850°C. The magnetization measurement was carried out by a sample vibration type magnetometer by using a bundle of 5-20 lines about 5.5 mm in length as the sample.

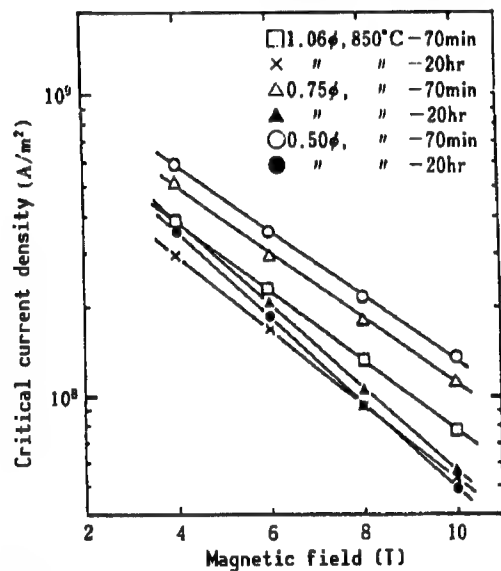


Figure 15. Magnetic Field Characteristic of Critical Current Density of Nb<sub>3</sub>Al Wire (wire radius of 0.55 mm, 0.75 mm, and 1 mm; heat treatment at 850°C for 70 min and 20 hr)

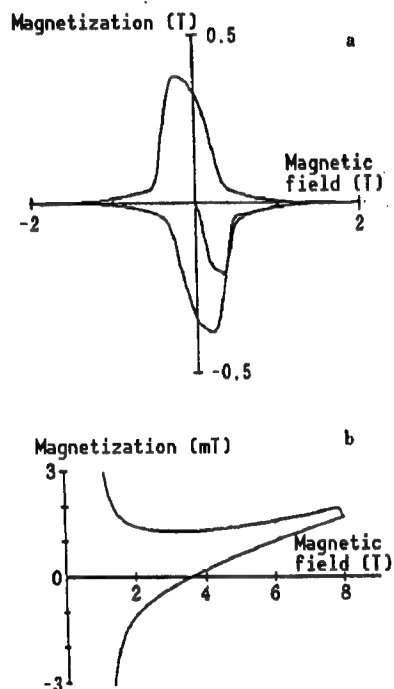


Figure 16. Examples of Magnetization Curve of Nb<sub>3</sub>Al Wire

Figure 15 shows the magnetic field dependence of  $J_c$  per total cross sectional area of the wire. The value of  $J_c$  is higher for smaller wire diameter and shorter heat-treatment time, and it was highest for the 0.5 mm sample treated for 70 minutes. Figure 16 shows an example of magnetization loop per total volume of the wire obtained by the magnetization measurement. Figure 16(a) is an example of measurement for a magnetic field swing of  $\pm 2$  T, where the large magnetization hysteresis that appears within  $\pm 0.5$  T is due to the Nb matrix that occupies about 90 percent of the wire volume, and its shape and size were fixed irrespective of the conditions of the heat treatment and the wire diameter. Figure 16(b) is an example of measurement at 0~8 T, and the magnetization hysteresis at magnetic fields above 1.5 T is due to Nb<sub>3</sub>Sn.

In accordance with the critical state model, there exists a relationship

$$\Delta M = (r/3 \pi) d_{\text{eff}}$$

between  $J_c$  and the difference  $\Delta M$  between the magnetizations at the times of rise and fall of the magnetic field. In the above,  $d_{\text{eff}}$  is the equivalent diameter of the superconducting conductor which is equal to the actual diameter of the superconducting conductor if physical or electromagnetic coupling between the superconducting conductors does not exist. The equivalent conductor diameter is an important index for evaluating the performance of a superconducting wire, where the stability as a superconducting wire is higher and the ac loss is lower when its value is smaller. Figure 17 shows the magnetic field dependence of the equivalent conductor diameter determined by the above equation. The equivalent conductor diameter at 8 T is 2-4  $\mu\text{m}$  which is considerably smaller than the value obtained by the conventional powder metallurgical method (equivalent conductor diameter of 4-6  $\mu\text{m}$ ) or the jelly roll method (20  $\mu\text{m}$ ). However, this value is considerably larger than the anticipated  $\text{Nb}_3\text{Al}$  conductor diameter (about 0.1  $\mu\text{m}$ ), and is a value that corresponds to the size (about 1.8  $\mu\text{m}$  for a wire with outer diameter of 0.5 mm, and about 3.8  $\mu\text{m}$  for a wire of 1 mm) of a bundle of 120 composite single conductor wires. Considered electromagnetically, the individual  $\text{Nb}_3\text{Al}$  cores are not mutually isolated but the bundle of 120 conductors seems to behave as a united body. It seems to be possible to further reduce the equivalent conductor diameter by varying the composition ratio Nb/Al in the stage of composite single conductor wire, or by reducing the number of wires formed into a bundle. It can be seen from Figure 17 that the equivalent conductor diameter tends to increase on the low magnetic field side, but the reason for this is yet unknown.

The  $\text{Nb}_3\text{Al}$  wire under development in our laboratory has a small equivalent conductor diameter and is promising as a wire for a fusion reactor compared with other compound system superconducting materials, but there remain problems to be overcome before it can be put to practical use. Even limiting these problems to the stability and the ac loss, it will be necessary to reduce the Nb matrix which is the cause of high ac loss at low magnetic fields, to reduce the equivalent conductor diameter at high magnetic fields, enhance the stability by combining Cu, etc.

## 5. Development of New Superconducting Wires

### 5.1 New Method of Manufacturing $\text{Nb}_3\text{Sn}$ Wires

The hot isostatic pressing (HIP processing) is being utilized to improve the toughness of sintered bodies of ceramics, etc. This research aims at improving  $J_c$  and the stress characteristic by applying the HIP processing to the manufacture of the  $\text{Nb}_3\text{Sn}$  wire.

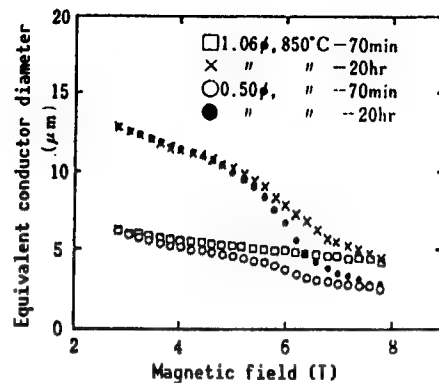


Figure 17. Magnetic Field Dependence of Equivalent Conductor Diameter of  $\text{Nb}_3\text{Al}$  Wires

In the bronze method which is being put to practical use as a manufacturing method of superthin multiconductor  $\text{Nb}_3\text{Sn}$  wire, there is mutual diffusion of the Sn atoms within the Cu-Sn alloy and the Nb atoms in the conductor for the formation of the nuclear fusion reactor superconducting compound phase. In this case, the Sn atom diffuses faster than the Nb atom so that the excess voids flow into the Cu-Sn alloy, and it is reported that the aggregation of these voids form microscopic voids (Kirkendall voids) at the interface between the  $\text{Nb}_3\text{Sn}$  phase and the Cu-Sn alloy or its proximity. When a load is applied to the wire, such voids become the starting points of cracks, and cause deterioration of the characteristic for the stress and strain of the wire. According to conventional research, an example of annihilation of the Kirkendall voids by subjecting the sample to HIP processing following heat treatment is repeated. This research examined the effect of formation of the homogeneous superconducting phase, etc., in addition to the suppression of formation of the Kirkendall voids, by conducting the heat treatment itself in the HIP device and forming the  $\text{Nb}_3\text{Sn}$  phase under an isostatic pressure at high temperature.

The samples used are composite single conductor wires having an outer diameter of 0.4 mm, a conductor diameter of about 0.2 mm, and a matrix composition of Cu-7at%Sn, and three kinds of conductors, Nb, Nb-2at%Ti, and Nb-4at%Ti. For these samples,  $T_c$  and  $I_c$  were measured by subjecting them to HIP processing of 750~850°C, 100 hours, and pressure of 1 GPa. The thickness, the diameter of crystal grains, and the composition of the  $\text{Nb}_3\text{Sn}$  layer were examined using an optical microscope and an X-ray microanalyzer.

As to the influence of adding Ti on  $T_c$ , it is reported  $T_c$  increases, but according to the result of this experiment not much influence was observed. For the relationship between  $T_c$  and pressure, a slight decreasing tendency of  $T_c$  was observed with the increase in pressure at 750°C and 800°C. At the heat treatment temperature of 850°C,  $T_c$  showed a maximum value in the vicinity of 10 MPa.  $T_c$  showed a complex change for the heat-treatment temperature and the pressure.

On the other hand, the formation of the  $\text{Nb}_3\text{Sn}$  phase was suppressed by heat treatment under an isostatic pressure for all samples, and the thickness of the  $\text{Nb}_3\text{Sn}$  layer decreased rather uniformly. This shows that the diffusion of atoms is suppressed under an isostatic pressure.

As to the composition of the  $\text{Nb}_3\text{Sn}$  layer, the Ti concentration in the layer is increased by the addition of Ti to the Nb core. Although no change was observed in the Nb concentration with the increase of the Ti concentration in the layer, the Sn concentration clearly decreased. It seems that Ti is replaced by Sn, not by Nb, though it cannot be concluded from this experiment alone. The isostatic pressure up to 1 GPa did not have much effect on the composition of the  $\text{Nb}_3\text{Sn}$  layer formed, but there was observed a tendency that the Nb concentration is decreased and the Sn concentration is increased with the increase in pressure. It is interesting to see which diffusion of the Nb atom and Sn atoms is influenced by isostatic pressure.

Figure 18 shows the dependence of  $I_c$  on the isostatic pressure under various heat-treatment conditions for wires in the magnetic field of 12 T. The addition of Ti to the Nb core improved the value for  $I_c$ . Samples heat treated in an isostatic pressure showed higher values of  $I_c$  than samples heat treated without pressurizing, and showed a maximum value in the neighborhood of 10 MPa for heat-treatment temperatures at 750°C and 800°C, and a maximum value at 100 MPa for 850°C. In this manner, heat treatment under isostatic pressure was effective for improving the  $I_c$  characteristic of the wires. In the future, it will be necessary to evaluate the  $I_c$  characteristic of HIP processed wires under stress.

## 5.2 Manufacturing Method of Y-System Oxide Superconductors

The Y-system oxide superconductor discovered by Chu, et al., following the discovery of the La-system oxide high-temperature superconductor by Benortz and Mueller, shows an extremely high  $T_c$  of higher than 90 K. For this reason, wideranging analysis of the crystal structure and measurements of the properties such as the material properties and specific heat of this material was done and microscopic properties were determined to a considerable degree. However, the value for  $J_c$  at the liquid nitrogen temperature (77 K) is rather low. This fact has been a big stumbling block in putting this material to practical use.

The effect of the cold isostatic pressing (CIP) for the manufacture of the Y-system oxide superconductor was examined in view of the result that the  $J_c$  characteristic can be improved for the  $\text{Nb}_3\text{Sn}$  wires subjected to isostatic pressure processing. In that connection, the effect of mixing part of the component material as the binder at the time of sintering was also examined.

The powders of  $\text{Y}_2\text{O}_3$ ,  $\text{Ba}(\text{NO}_3)_2$ , and  $\text{CuO}$  are mixed in the ratios of  $\text{Y}:\text{Ba}:\text{Cu} = 1:2:3$ , and the mixture was calcined for 15 hours at 900–950°C. The calcined sample was pulverized and divided into five parts, and  $\text{Y}_2\text{O}_3$ ,  $\text{Ba}(\text{NO}_3)_2$ ,  $\text{CuO}$  and powder of metallic copper were added to each portion at the rate of 10 mol% in the equivalent of Y, Ba, and Cu. The mixed powder was made into plate form under mechanical pressure of 150 MPa, and sintered for 15 hours at the same temperature as the calcination in an oxygen flow ( $20 \text{ m}^3/\text{sec}$ ). After the sintering the sample was gradually cooled in the furnace. The values of  $T_c$  and  $J_c$  at the liquid nitrogen temperature (77 K) were measured by the four-terminal resistance method.

For  $T_c$ , values higher than 80 K were obtained for all samples. For  $J_c$ , only samples added with  $\text{CuO}$  showed improvement compared with samples without addition of  $\text{CuO}$ . From this result,  $\text{CuO}$  was selected as an addition, and the effect of the added amount and CIP was investigated in detail.

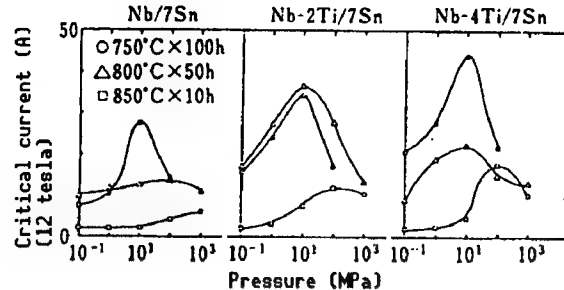


Figure 18. Pressure Dependence of Critical Current of HIP Processed  $\text{Nb}_3\text{Sn}$  Wires

Samples mixed with CuO in the amount of 0, 2.5, 5.0, 7.5, and 10 mol% in Cu equivalent were calcined, and after being pressed they were pressurized isotropically. Finally, they were sintered for 15 hours at 900 or 950°C, and after holding them for 15 hours at 700°C, they were cooled in the furnace. From the result of X-ray diffraction of the sintered samples, it was found that the samples consist of the orthorhombic and cubic  $(Y, Ba)_3Cu_3O_{7-x}$ .

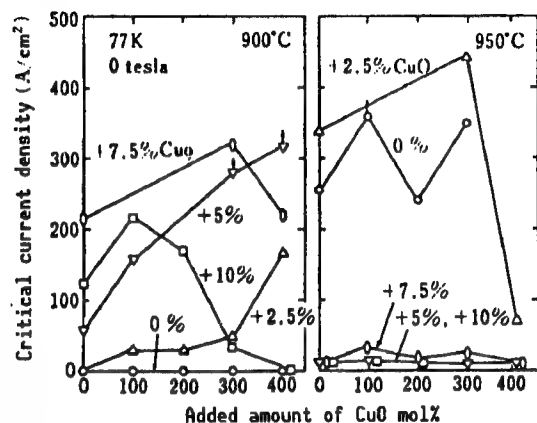


Figure 19. Change With CIP Pressure, of Critical Current Density at 77 K of  $(Y, Ba)_3Cu_3O_{7-x}$  Sintered Bodies Added With 0~10% of CuO

Figure 19 shows the change of  $J_c$  by the CIP pressure by CuO added samples. The value of  $J_c$  depended strongly on the added amount of CuO and the CIP pressure. For the samples sintered at 900°C, a maximum  $J_c$  of about  $300 \text{ A/cm}^2$  was obtained under the conditions of 7.5 mol% of CuO addition and 300 MPa of CIP pressure. For the samples sintered at 950°C, a maximum  $J_c$  of about  $440 \text{ A/cm}^2$  was obtained under the conditions of 2.5 mol% and 300 MPa.

Figure 20 shows the volume fraction of  $(Y, Ba)_3Cu_3O_{7-x}$  at 77 K as a function of added CuO. The volume fraction was determined from the slope of the magnetization curve in the vicinity of zero magnetic field by disregarding the diamagnetic field effect. The addition of CuO showed the effect of increasing the amount of  $(Y, Ba)_3Cu_3O_{7-x}$  for both sintering temperatures of 900 and 950°C, but the CIP processing was effective only for 900°C. In addition, through scanning electron microscopic observation it was clear that the addition of CuO has an effect of increasing the size of the crystal grains.

As a result of this research it was found that the use of CuO as the bonding assistant in the formation of the Y-system oxide superconductor has an effect of improving the value of  $J_c$ .

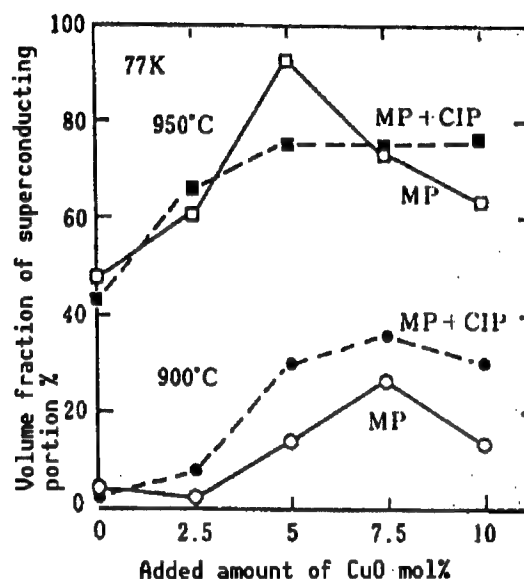


Figure 20. Change in Volume Fraction Due to Added Amount of CuO, of  $(Y, Ba)_3Cu_3O_{7-x}$  Oxides at 77 K and Zero Magnetic Field

## 5. Conclusion

In this research, a basic testing technology was developed for evaluating the characteristics of superconducting wires in the environment (cooling by superfluidic helium, stress, varying magnetic field, etc.) to which the superconducting wires are exposed in the nuclear fusion reactor, and the characteristics of various kinds of superconducting wires were evaluated by the technology developed.

(1) Concerning the evaluation of characteristics in the superfluidic helium temperature region, VTiTa superconducting alloy which can generate a magnetic field up to 12 T by cooling with superfluidic helium was developed. As to the compound systems,  $V_3Ga$  tape wire by the surface diffusion method, superthin multiconductor  $(Nb,Ti)_3Sn$  wire by the bronze method, and superthin multi-conductor  $V_2(Hf,Zr)$  wire by the compound processing method can possibly be used to generate a magnetic field up to 20 T.

(2) Concerning the evaluation of the characteristics under stress, it was found that the volume ratio of the bronze matrix to the wire has a strong influence on the critical temperature and the critical current of the  $Nb_3Sn$  wire by the bronze method under a static stress. A repeated strain gives rise to deterioration of the stabilized copper for the superthin multiconductor wires of NbTi alloy,  $Nb_3Sn$  compound, and  $V_2(Hf,Zr)$  compound, but it does not seriously affect their superconductivity. Even for the compound system wires that are susceptible to mechanical damage such as cracks, a large deterioration in their characteristics will not be generated so long as the magnitude of the repeated stress is confined within the range of reversible strain.

(3) In the evaluation tests of characteristics in varying magnetic fields, a device for measuring the pulse loss was trial manufactured. It was found that the superthin multiconductor  $Nb_3Sn$  wire by the compound processing method has a small effective conductor diameter evaluated by magnetization measurement, and that it is promising as a pulse wire for a nuclear fusion reactor.

(4) For  $Nb_3Sn$  wire subjected to heat treatment in hot isostatic press (HIP) the critical current was increased higher than heat treatment under no pressure. It was found that a heat treatment under isostatic pressure is effective for the improvement of the stress resistant characteristic as well as the critical current characteristic of the wire.

(5) The effect of cold isostatic pressing (CIP) in the manufacture of  $(Y,Ba)_3Cu_3O_{7-x}$  oxide superconductors was investigated. It was found that the critical current density of  $(Y,Ba)_3Cu_3O_{7-x}$  can be improved by applying appropriate heat treatment and CIP processing using CuO as a bonding assistant.

**Research on Manufacturing Intermetallic Compounds by Self-Propagating High-Temperature Syntheses**

916C0048C Tokyo KENKYU HOKOKUSHU 12 in Japanese 1991 Issue pp 113-120

[Article on priority basic research by Science and Engineering Promotion Adjustment Fund in FY88]

**[Text] Abstract**

The NiTi shape memory alloy is ordinarily manufactured by the high frequency vacuum melt method. This alloy shows a variation of the martensitic transformation temperature of about 10 K for a change of 0.1 mass% so that it is very difficult to control the transformation temperature to control the composition in a precise manner.

In this research, an ingot of the NiTi shape memory alloy was manufactured by one of the new manufacturing methods, the combustion synthesis method, using elemental powders of Ni and Ti which can control the composition relatively easily. In this method, Ni and Ti powders were blended to have Ni50at%, and mixed by a dry ball mill. This mixed powder filled a graphite crucible, and was combustion synthesized by igniting one end of the upper part of the sample by heating with a tungsten heater in a vacuum ( $10^{-4}$ Pa) and in argon gas. After subjecting the synthesized ingot to HIP processing, plate material and wire material were formed by plastic working.

An ignition experiment was carried out for the sample temperature ranging from room temperature to 873 K. It was found that ignition can be achieved surely in a high vacuum as well as in argon gas, and the reaction propagated on its own. It was confirmed by X-ray diffraction test that the combustion synthesized was in the form of NiTi intermetallic compound for all temperatures irrespective of the sample temperature at the time of ignition. Although the ingot immediately after the combustion synthesis was porous with a relative density of 50-60 percent, it was possible to enhance the relative density to 100 percent by subjecting the sample to hot isostatic pressing (HIP) processing (temperature of 1023 K and pressure of 100 MPa). The possibility of giving plastic processing to the high density ingot was investigated by subjecting it to hot rolling, hot groove rolling, hot and cold swaging machining, and cold drawing. For oxygen content of over 0.5 mass% of the

synthesized samples it was possible to work it to wires of up to  $\phi$ 0.25 mm. On the other hand, samples with oxygen content of 0.07 percent it was possible to process it to wires less than  $\phi$ 0.09 mm. The wires have shape memory ability, and the shape memory temperature was about 370 K.

## 1. Introduction

The NiTi shape memory alloy is ordinarily manufactured by the high frequency vacuum melt method. Since the martensitic transformation temperature of this alloy varies by about 10 K for a small composition change of 0.1 mass%, it is said to be difficult for the vacuum melt method to control the transformation temperature by a precise control of the composition. As the method for relatively easily controlling the composition, the alloy powder sintering method and the elemental powder sintering method are proposed. In the alloy powder sintering method, the molten metal alloyed by the arc melt method is formed into powder by the gas atomization method, and plastic processing is given after the sample is subjected to an HIP sintering. This method makes the plastic processing up to the manufacture of wires possible, but the method has not been commercialized because the manufacturing cost runs too high. In the elemental powder sintering method, it is reported that the manufacturing cost is low but the plastic processing is not feasible because the oxygen concentration of the sintered material is too high, thus wires and plate materials cannot be produced.

In this research, we tried to produce a porous sintered body of NiTi shape memory alloy by the so-called self-propagating high-temperature synthesis method (or combustion synthesis method) which utilizes the heat produced in the formation of the intermetallic compound of NiTi. This produces a sintered body with relative density of 100 percent by subjecting the sample to HIP, and forming plate materials and wire materials by plastic processing (rolling, swaging, and drawing). As a result, we were able to construct for the first time the basis of a process which makes it possible to industrially produce wire materials and plate materials of NiTi shape memory alloy that can be put to practical use by means of a new elemental powder sintering method which is different from the conventional powder metallurgical technique. The method of production follows.

## 2. Raw Material Powder

The raw material powders used for the experiment are commercially available and have the chemical composition and the powder grain size as shown in Table 1. The mixed powder was classified into two kinds of mixed powder A (Ni powder containing 0.12 mass% of oxygen and Ti powder containing 0.34 mass% of oxygen) and mixed powder B (Ni powder containing 0.052 mass% of oxygen and Ti powder containing 0.072 mass% of oxygen) depending upon the oxygen content of the raw material powder. The role of the oxygen content that affects the plastic processing for producing wire materials and plate materials and the feasibility itself of plastic processing, after the combustion synthesis of the powder, were examined. Photograph 1 [not reproduced] shows the scanning electron microscope (SEM) photographs of the raw material powder and the mixed powder. The Ni powders used for the mixed powder A and for the mixed powder B

Table 1. Chemical Composition and Grain Size of Ni and Ti Powders

Sample	O	C	Ni	Ti	Na	Grain size	Production method of metallic powder
A	Ni	0.12	0.20	>99.8	—	—	3~5 μm Carbonyl nickel
	Ti	0.34	0.009	—	>99.5	0.078	<350 mesh Sodium reduction method
B	Ni	0.052	0.057	>99.8	—	—	5~20 μm Carbonyl nickel
	Ti	0.072	0.005	—	>99.5	0.050	<200 mesh Sodium reduction method

are spherical in shape because both are carbonyl Ni powders. The Ti powders used for both are irregular in shape because they are pulverized powders, but B makes the oxygen content small so that the grain size of A is large.

### 3. Experimental Method

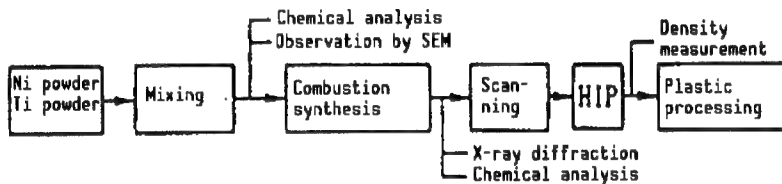


Figure 1. Flow Chart of Manufacturing Process of NiTi Shape Memory Intermetallic Compound by Combustion Synthesis

The manufacturing process of NiTi alloy by the combustion synthesis method is shown in Figure 1. The experimental method and the experimental conditions will be shown in accordance with this manufacturing process. First, the elemental powders of Ni and Ti are weighed so Ni is 50 at%. These powders were mixed in a dry ball mill under the conditions of 0.6~2 kg at one time, and processing time of 36~180 ks by sealing argon gas. The mixed powder was subjected to chemical analysis and SEM observation to confirm the state of mixing. Next, the mixed powder was filled in a graphite crucible (inner diameter 30~40 mm and inner length 70~150 mm) in an amount of 100~400 g. The crucible was placed in argon and in a vacuum ( $10^{-4}$ Pa), and one end in the upper part of the mixed powder was ignited in noncontact manner by strong heating with a tungsten heater, to initiate the combustion synthesis. The sample was placed in an electric furnace, and it was arranged in such a way that the sample can be kept at a desired temperature in advance. The present experiment was carried out by varying the sample temperature in the range of room temperature to 873 K. When the sample caught fire, the synthesis reaction self-propagated from the lighted point to the other end, and the whole sample was synthesized by combustion, the phases of the sample were identified by X-ray diffraction, and the relation between the blending value and the chemical composition after the combustion synthesis was investigated by chemical analysis. Next, a sample which went through the combustion synthesis was subjected to HIP in order to enhance the relative density. Before HIP processing, the combustion synthesized sample was sealed in a titanium container at a vacuum of  $10^{-4}$ Pa. The sealed sample was subjected again to HIP processing under the conditions of temperature of 1203 K, pressure of 100 MPa, and holding time of 10.8 ks to manufacture a cylindrical sample (diameter of

30~60 mm and length of 80~150 mm), and measurement of the relative density and optical microscopic observation were carried out.

The HIP-processed NiTi sample was removed from the titanium container, and the possibility of plastic processing such as rolling and drawing were investigated. The heating temperature of the sample at the time of hot processing and the annealing temperature at the time of cold processing were in the range of 1173~1223 K, and these were carried out in a flow of argon gas.

The plastic processing to obtain plate materials, a special hot atmosphere rolling mill was used. The processing conditions for using the mill were: an atmosphere of argon gas flow, rolling speed of about 17 mm/s (or 1 m/min), and depression of 1 to 0.5 mm/pass.

For the plastic processing to obtain wire materials, a general hot rolling mill was used. The processing conditions for using the mill were: normal atmosphere; rolling speed of about 0.28 m/s (17 m/min); and depression of 0.75 mm/pass. This rolling mill was used to reduce a raw material with circular cross sectional shape 30 mm in diameter to a square bar of 14.5 mm per side. Next, the square bar raw material of 14.5 mm per side was plastically processed until a square bar of 6 mm per side was obtained by using a hot groove roll mill under the condition of depression of 0.5 mm/pass. Next, plastic processing from the square bar of 6 mm per side to a circular bar 2 mm in diameter was carried out by using a hot swaging machine under the processing condition of depression of 0.5~0.25 mm in terms of the diameter. Then, cold drawing was carried out until the desired size was obtained. Samples processed to wires were processed to have coil form, shape memory processing was applied, and the presence of the shape memory ability was confirmed in warm water and the transformation point was measured by a differential scanning calorimeter (DSC). The conditions for the shape memory processing were a temperature of 723 K in the air, a holding time of 3.6 ks, and the sample was air-cooled after the holding.

#### 4. Principle of Combustion Synthesis

Combustion synthesis is to synthesize a compound of two or more substances by utilizing their heat of formation, and the change in the enthalpy H for absolute temperature T of elements and their compound and the heat of formation  $\Delta H$  are shown schematically in Figure 2.

On the assumption that there is no exchange of heat from outside, the temperature to which the mixed powder reached the compound AB by combustion synthesis is adiabatic ( $T_{ad}$ ), the specific heat is  $C_p$ , and the heat of formation at an initial temperature ( $T_0$ ) is  $-\Delta H_{T_0}^o$ , relationship among these figures are as follows:

$$-\Delta H_{T_0}^o = \int_{T_0}^{T_{ad}} C_p(AB) dT.$$

In other words, the mixed powder is ignited at the initial temperature  $T_0$ , it discharges the heat of formation  $-\Delta H_{T_0}^{\circ}$  and arrives at the adiabatic temperature  $T_{ad}$ . If the adiabatic temperature  $T_{ad}$  is higher than the melting point  $T_m$  of the compound, the liquid phase during reaction at that time appears, thus the diffusion of the atoms is markedly accelerated, facilitating the combustion synthesis. Figure 3 is an explanatory diagram showing the combustion synthesis experiment.

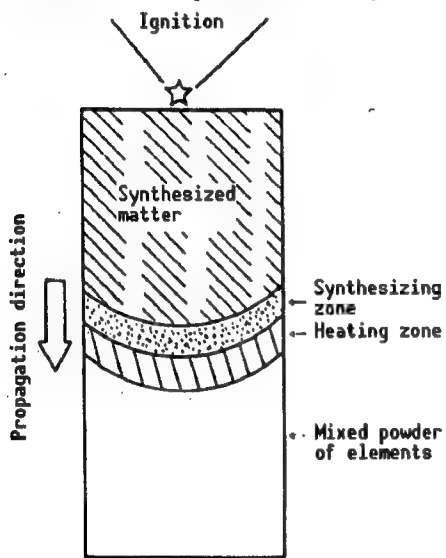


Figure 3. Schematic Diagram for Combustion Synthesis

of NiTi intermetallic compound by the combustion synthesis of the elemental powders of Ni and Ti were examined. Calculations to estimate the adiabatic temperature in this reaction is shown in Figure 4. The formation heat of NiTi intermetallic compound is 67.8 kJ/mol according to the measured value of Kubaschewski. This value is considerably smaller than for ceramics. Nonetheless, this value was sufficient to induce the combustion synthesis reaction. In addition, when the combustion synthesis was initiated by igniting the mixed powder at room temperature, theoretically, the adiabatic temperature reaches the vicinity of  $T_m$  of 1513 K which is the melting point of the NiTi alloy, as can be seen from Figure 4, forming the liquid phase. From what was said in the above it can be seen that the NiTi intermetallic compound is manufacturable by combustion synthesis.

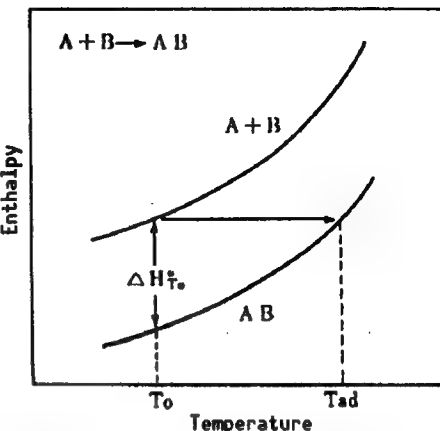


Figure 2. Enthalpy Changes in Elements and Their Compound and Heat of Formation

When one end in the upper part of the mixed powder of the raw materials is heated and ignited, chemical reaction takes place at the ignition point and formation heat is generated. This heat is transmitted around the ignition point, inducing the chemical reaction which generates anew the formation heat. This process continues in the form of a chain reaction throughout the mixed powder, eventually converting the entire sample to the compound.

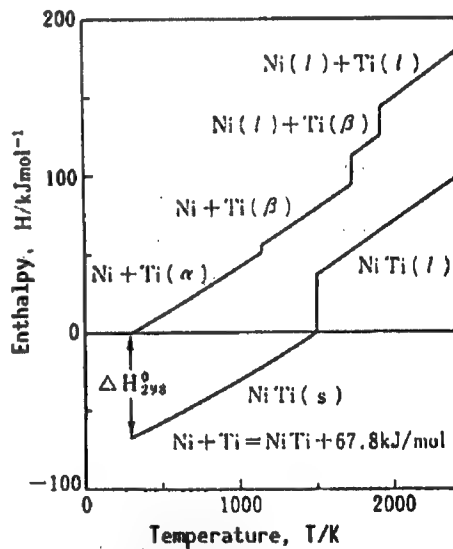


Figure 4. Enthalpy Change Between Ni+Ti and NiTi and Heat of Formation of NiTi

## 5. Ignition and Propagation Reaction

A sample mixed in the dry ball mill had small Ni powder covering large Ti powder, as shown in the SEM photograph in Photograph 1 [not reproduced]. Further, chemical analysis for various parts of the mixed powder of the raw materials revealed that there was no difference due to the spots, and it was confirmed that the mixing was sufficiently uniform. The mixed powders A and B were filled in predetermined crucibles, and were ignited in the two environmental conditions of in-argon-gas and in-a-vacuum.

The mixed powder A in either argon gas or a vacuum and at onset temperatures ranging from room temperature to 873 K was confirmed to ignite easily, and to reach self-propagation in combustion.

On the other hand, in the mixed powder B, when the initial temperature of the sample is room temperature, it was not possible to ignite the sample in either condition of in-argon-gas or in-a-vacuum. Therefore, the ignition experiment was carried out by heating and holding the mixed powder in an electric furnace to raise the initial temperature higher than room temperature. In argon gas, the reaction propagated at about 453 K, but this propagation reaction stopped in the midst of the sample. At 473 K, the propagation reaction was sustained, progressed to the last part of the mixed powder, and the combustion synthesis covered the entire sample. On the other hand, in-a-vacuum, the propagation reaction stopped midway in the case of the initial temperature of 503 K, but when the initial temperature was above about 523 K, the propagation reaction was stable, and the entire sample formed a synthesized body.

The grain sizes are different for the mixed powder of raw materials A and B, but the experimental conditions such as the filling factor to the crucible, method of ignition, etc., were completely identical. However, the mixed powder A could be ignited at a lower temperature than mixed powder B, and the propagation reaction occurred. The reason for this is that the mixed powder A has smaller grain size than mixed powder B, the specific surface area of powder A is greater, thus the mutual contact of the powders is satisfactory, the ignition and heat transmission at the time of propagation are more satisfactory, and the diffusion between the different powders during the reaction is easier.

Further, in the case of mixed powder B, the initial temperature of the sample at which ignition and combustion synthesis are possible varies with the environment that surrounds the sample, that is, whether the sample is in-argon-gas or in-a-vacuum. The reason for this is due to the difference in the thermal conduction. In-a-vacuum, the transmission of heat between powders is done mainly by heat conduction in a solid via the contact point of the particles and radiation. In contrast, in-argon-gas, heat conduction by convection of gas is added to the above-mentioned heat transmission modes, thus heat transmission to the adjacent powder becomes far more efficient than in the case of heat transmission in-a-vacuum, and the ignition and propagation reaction are facilitated.

The minimum temperature at which stable ignition and propagation reaction can take place in the mixed powder B was 473 K in-argon-gas and 523 K in-a-vacuum. The heating time for ignition was 5~10 seconds for both cases. The reason that the ignition in mixed powder B takes places in the range of room temperature to about 500 K, but the propagation reaction stopped in the midst, is as follows: Because of heating for several seconds with the heater, the temperature only in the proximity of the ignition point reached a temperature which can initiate the propagation reaction, but the temperature of the mixed powder of the raw materials in the lower part is at low temperature, so the propagation reaction cannot be continued. On the other hand, in the mixed powder A, the grain size of the powders is small and the contact area between the powders is large, so the heat transmission is satisfactory in-a-vacuum as well as in-argon-gas, permitting propagation of reaction even at room temperature.

Photograph 2 [not reproduced] shows the vertical section views of the samples when ignition is started in vacuum at the end on the lefthand side and the combustion synthesis progressed in the direction of the arrow. This photograph makes it possible to see the propagation of the reaction. The speed of self-propagation varied with the grain size of the powder, the packing density, and the sample temperature at the time of ignition. In the case of the mixed powder A shown in Photograph 2, the propagation speed was about 4 mm/s for the case of ignite at room temperature of the initial temperature and in vacuum. In addition, the result of measuring propagation reaction temperature by burying in the sample a PR thermocouple 0.2 mm in diameter showed that it agreed with the melting point (1513 K) of NiTi alloy. This agrees with the material shown in Figure 4 that when the initial temperature of combustion synthesis is from room temperature to 900 K, the adiabatic temperature reaches the melting point of NiTi.

#### 6. Characteristics of Combustion Synthesized Samples

Photograph 3 [not reproduced] shows the optical microstructure and SEM microstructure of the samples shown in Photograph 2. As can be seen from the top photos in Photographs 2 and 3 [not reproduced], samples that underwent combustion synthesis alone are in porous condition. When these samples are observed by scanning electron microscope of high magnification, as can be seen from the SEM photographs in Photograph 3, a dendritic structure for both powders A and B is observed, indicating that the propagation reaction progressed while being melted. When the sample temperature at the time of ignition is raised, the adiabatic temperature does not change even if the initial temperature of the sample is raised, as can be seen from Figure 4. It is believed that the enthalpy is raised, the reaction

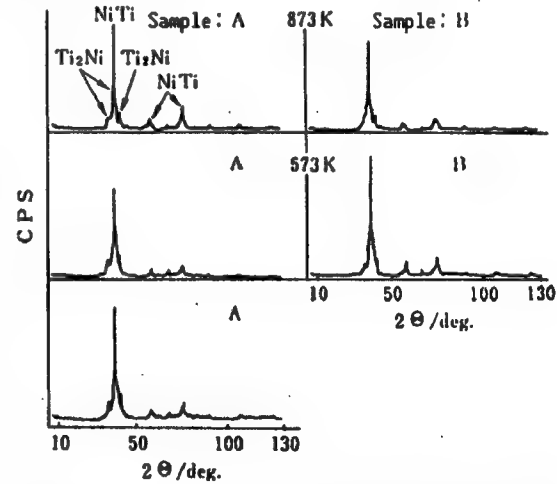


Figure 5. X-Ray Diffraction Patterns of NiTi Ignited at Various Temperatures, and Combustion Synthesized

becomes violent, and large voids are left behind. The phases of the combustion synthesized samples were identified by X-ray diffraction. As shown in the several examples in Figure 5, a peak of the intermetallic compound phase of NiTi was confirmed in every one of the combustion synthesized samples irrespective of the sample temperature at the time of ignition. From what has been said, it is believed that the initial temperature of the sample at the time of ignition should be lower in order to obtain a sample of NiTi with high relative density.

Table 2. Chemical Compositions of the Mixed Powder (Ni+Ti) for Samples A and B, and of Combustion Synthesized Powder NiTi

Sample	Chemical composition			
	Mixed powder	Synthesized powder	Ni	Ti
A	Ni	55.0	Ni	55.10
	Ti	45.0	Ti	44.20
	O	0.45	O	0.36~0.45
B	Ni	55.0	Ni	54.90
	Ti	45.0	Ti	44.33
	O	0.10	O	0.05~0.07

fact that in the process up to ignition, a thorough degassing was carried out by raising the sample temperature to 873 K in a high vacuum ( $10^{-5}$ Pa), and then the combustion synthesis reaction took place in a high vacuum, so that oxygen adsorbed to the surface in the mixing processing, etc., was disturbed. In the so-called elemental powder sintering method, this degassing action cannot be observed, and the oxygen content is increased in every process eventually to the point higher than 0.6 mass%, making plastic processing impossible. In contrast, in the combustion synthesis method, degassing action takes place, making the oxygen content lower, as was clarified in this research. This degassing action is considered to be a big advantage of the combustion synthesis method. The reason why the degassing action is not observed in the elemental powder sintering method, whereas degassing action takes place in the combustion synthesis method, may be that in contrast to the elemental powder sintering method where sintering takes place in such a way as not to generate the liquid phase, in the combustion synthesis method, the liquid phase appears which facilitates the detachment of oxygen.

## 7. Possibility of Plastic Processing

Samples that are combustion synthesized are porous ingots with relative density of 50~60 percent as shown in Photographs 2 and 3 [not reproduced]; both the A and B materials cannot be plastically processed. Therefore, the samples were subjected to HIP processing in order to raise the density by eliminating numerous voids that exist in the sample. The HIP processing was carried out by sealing a sample in vacuum in a container, and under the conditions described in "Experimental Method." As a result, a satisfactory ingot with 100 percent microscopic relative density was obtained as shown in

Table 2 shows the change from the chemical composition of the mixed powder and the composition after the combustion synthesis (ignition in vacuum). For both samples A and B, the change in the Ni composition after combustion synthesis was within 0.1 percent of the blended value. On the other hand, the oxygen content decreased to a considerably lower level compared with that at the time of mixing, approaching the oxygen content of the original material. This is due to the

Photograph 4 [not reproduced]. Using such an ingot, an experiment on plastic processing was carried out.

For rolling, an ordinary hot rolling machine (rolling speed of 17 m/min) and a hot atmosphere rolling machine with low rolling speed (rolling speed of 1 m/min, in argon gas flow) were used. For an ingot of sample A (oxygen content of 0.35~0.45 mass%), it was possible to process a material 30 mm in diameter to eventually form a rod 2.5 mm in diameter by the processes of hot rolling→hot grooved rolling→hot swaging, but it was not possible to perform the swaging process and the cold drawing process. The reason for this is that the ingot of sample A is brittle due to the large oxygen content of 0.35~0.45 mass%.

For the ingot of sample B (oxygen content of 0.05~0.07 mass%) plastic processing was easy, thus it was possible to obtain a plate material 1.7 mm thick, 45 mm wide, and 600 mm long by a hot atmosphere rolling machine. Next, in the processing experiment to obtain wires, plastic processing was feasible for each process of ordinary hot rolling→hot grooved rolling→hot and cold swaging→cold drawing, under predetermined conditions, and wires with diameters up to 0.9 mm could be obtained. A summary of the above result for plastic processability along with the oxygen content before and after HIP processing and the measured values of the relative density are given in Table 3. Further, examples of samples which were subjected to the actual plastic processing are shown in Photograph 5 [not reproduced].

Table 3. Oxygen Concentration, Relative Density, and Plastic Processing Characteristics of Samples A and B Before and After HIP

	Before HIP			After HIP		
	Oxygen content	Relative density*	Plastic processing characteristics (rolled at 1173K)	Oxygen concentration	Relative density*	Plastic processing characteristics
A	0.36mass%~0.45mass%	50%~60%	Impossible	0.36mass%~0.45mass%	99.9%~100%	Hot processing is possible
B	0.05mass%~0.07mass%	50%~65%	Impossible	0.05mass%~0.07mass%	99.7%~100%	Possible

\* Computed with true density =  $6.45 \times 10^3 \text{ kg/m}^3$

In order to examine whether the samples obtained from the material B have actual shape memory property, the wires obtained were made into coil form and subjected to shape memory processing under the conditions of heat-treatment temperature of 723 K and holding time of 90 ks. As a result of tests in warm water, it was confirmed that the shape memory temperature is about 370 K and the recovery force is sufficiently large, and the sample has sufficient shape memory property. This situation is shown in Photograph 6 [not reproduced]. In order to accurately examine the transformation temperature of the material, the same sample was studied with a differential scan calorimeter (DSC) and the result is shown in Figure 6. The transformation temperatures obtainable from the figure agreed with the result of examination of the actual shape changes.

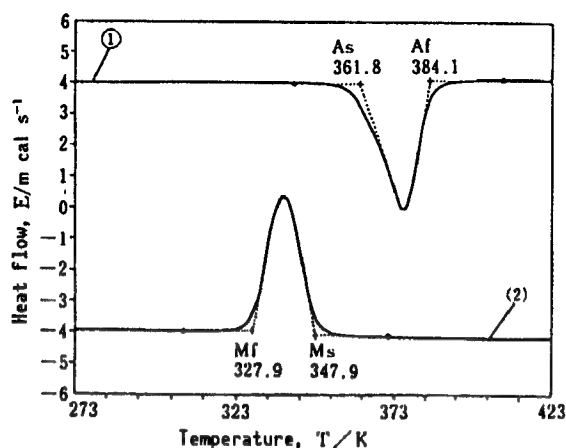


Figure 6. Measurement Result by Differential Scanning Calorimeter of NiTi Intermetallic Compound Manufactured by Combustion Synthesis Method and Formed Into Wires by Plastic Processing, and Various Kinds of Transformation Temperatures

## 8. Conclusion

Using commercially available elemental powders of Ni and Ti the possibility of manufacturing NiTi shape memory alloy by a new manufacturing method of combustion synthesis was studied, and the following results were obtained:

- (1) It was possible to combustion synthesize a mixing powder of Ni and Ti in a high vacuum and in argon gas at temperatures ranging from room temperature to 873 K.
- (2) It was confirmed by X-ray diffraction that the combustion synthesized samples were formed into NiTi intermetallic compound regardless of the sample temperature at the time of ignition.
- (3) It was possible to raise the relative density of the combustion synthesized samples to 100 percent by HIP processing.
- (4) Even when the oxygen content of the combustion synthesized samples is higher than 0.5 mass%, it was possible to process them to wires of up to  $\phi 2.5$  mm. On the other hand, samples having oxygen content of 0.07 mass% were processable to wires of up to  $\phi 0.9$  mm.
- (5) Wires manufactured by combustion synthesis and plastic processing have sufficient shape memory property.

## **Composite Materials R&D**

916C0048D Tokyo KENKYU HOKOKUSHU 12 in Japanese 1991 Issue pp 125-134

[Research funded by other agencies, FY82-FY88]

### **[Text] Abstract**

In recent years, for use in aircraft, etc., Ti (or its alloy)-based fiber-reinforced metals (FRMs) that are lightweight and high strength and can be used at intermediate to high temperatures such as 500~600°C are attracting attention. Composite materials are in a thermodynamically nonequilibrium state because of the coexistence of two or more kinds of materials. Accordingly, reactions occur frequently between the fibers and the base material at the time of formation or use at high temperatures, which can become the starting points of fracture. As basic research aimed at suppressing these reactions, we examined the problem of enhancing the adaptability of the composites to high temperature environment by their modification based principally on alloying the base metals. It was found, for heating single bodies of fiber, that SCS-6, which is a fiber of the SiC system, has the smallest deterioration. In addition, both Ti and Ti-6Al-4V that are the base metals showed the smallest deterioration.

When an FRM having pure Ti as the base metal is heated, TiC is formed in the neighborhood of the fibers, and  $Ti_5Si_3$  is formed on its outside. A deterioration in the strength of FRMs was observed together with the increase in the thickness of these reacted layers.

As elements to be added to suppress the surface reactions and the deterioration in the strength—used at high temperatures, by means of modification of the base materials—Al, V, Mo, etc., which stabilize the  $\alpha$ -phase and the  $\beta$ -phase of Ti were found to be effective. Addition of these elements showed an increased effect of suppressing the reactions when a number of them are used together. The reaction products in the case of using alloys as the base material are basically TiC and  $Ti_5Si_3$ , being approximately the same as when using pure Ti as the base material, having Al, V, Mo, etc., as solid solution in addition.

Although the deterioration in the strength of FRMs is closely related to the thickness of the reacted layers, it was found that there are cases in which the deterioration cannot be understood in terms of thickness alone.

## 1. Introduction

Part of the R&D Project of Basic Technology for Future Industries, MITI, included a research project related to metallic and composite materials that covered the period FY81 to FY88. This project consisted of research on the metallic materials and composite materials. Of those mentioned in "Composite Materials Research and Development," comprehensive research was done on advanced composite materials. In the field of fiber-reinforced plastic based composites (FRPs) which are advanced in connection with their practical applications, research was carried out starting with the investigation of the basic dynamic characteristics, covering the development, forming method, and construction of database, of the plastic base materials, aimed at further enhancing the characteristics.

On the other hand, of the similarly advanced composites of the metal based composites (FRMs), approaches from various directions were tried for the development, forming method, suitability, etc., of the materials. The metallic composites are now being studied based on the success of the FRPs to improve their high temperature characteristics, weatherability, etc. The reinforcing fibers used for FRMs can be classified into ceramic fibers and metallic fibers. The ceramic fibers can further be subdivided into precursor fibers that have diameters smaller than 20  $\mu\text{m}$  and chemical vapor deposition (CVD) fibers and whiskers that have diameters greater than 100  $\mu\text{m}$ .

The base metal is selected according to the target characteristics, but when light weight and high strength are the targets, Al, Mg, or their alloys are used. The temperature limit of the FRMs that have these metals or alloys as base material over long use will be about 300°C.

On the other hand, the requirements for materials for aircraft have become sophisticated in recent years. Required are materials that are light weight and high strength and yet can withstand intermediate and high temperatures such as 500~600°C, higher than what Al and Mg can withstand. As the material for FRMs that can be used under these conditions it is appropriate to use Ti (or its alloys) as the base material, and composites thus obtained are expected to be materials for the next generation. In addition, for FRMs for turbine blades, etc., of jet engines where heat resistance to temperatures higher than 1000°C is required, super heat-resistant alloys will likely be used.

The forming methods of industrial FRMs can be classified into the solid phase method and the liquid phase method. The liquid phase method is a method of formation at temperatures above the melting point of the base metal, and it is necessary to have the fiber and the metal at a high temperature for a certain length of time. In the solid phase method in which formation takes place at a temperature below the melting point of the base metal, it is necessary to fill the gap between the fibers with plastic deformation of the base metal, and

metals are bonded by diffusion. A rather high temperature and long time are required for the formation, although the material is in a solid state. FRMs are aimed at enhancing the high temperature characteristics that are the weakness of the FRPs, thus conditions for use are often at high temperatures.

On the other hand, composites are created to promote the advantages of each material or help overcome weaknesses, but such materials are in a thermodynamically nonequilibrium state. When formation and use are at high temperatures, mutual melting often occurs between the fiber and the base material, and the fiber or base material deteriorates. Further, depending upon the combination of the fiber and the base material, brittle reaction products sometimes form. In this case, the reaction products can become the starting point of fracture.

The basic approaches for suppressing the surface reaction include:

- (1) To modify the fiber to gain higher wettability with the base metal, and yet have small reactivity.
- (2) To form an intermediate layer that has similar effects as in the above between the fiber and the base material.
- (3) To modify the base material so it will have the similar effect.

Under such a background our laboratory participated in the research project. In view of the "R&D Project of Basic Technology for Future Industries" goals, we focused our attention on composites having Ti or a Ti alloy as the base material and reinforced by CVD fiber as light weight and high strength FRMs which can be used at intermediate and high temperatures. As our basic research goal, we tried to enhance the high temperature suitability based mainly on modification by alloying the base metal.

## 2. Experimental Method

### 2.1 Raw Materials

#### 2.1.1 Kinds and Characteristics of CVD Fibers

There are two kinds of CVD fibers as the reinforcing material for FRMs: B system and SiC system. There are three kinds of B system fibers: a fiber with no treatment on its surface (referred to as B fiber hereafter), a fiber obtained by covering the surface of the B fiber with  $B_4C$  to a thickness of about 10  $\mu m$  (referred to as  $B_4C/B$  fiber), and a fiber obtained by covering the surface of the B fiber with SiC to a thickness of about 2  $\mu m$  (referred to as SiC/B fiber).

Among the SiC system fibers, a fiber which is not surface treated (referred to as SiC fiber hereafter) was commercially available in the beginning. Among the SiC fibers one has W (diameter of about 12  $\mu m$ ) as the conductor, and one has C (diameter of about 30  $\mu m$ ) as the conductor. These fibers have SiC on the surface, and the strength characteristic and their reactivity with the base

metal are roughly equal so that these two types can be described as being the same.

Although of the same SiC system fibers, one fiber with the trade name SCS-2 (referred to as SCS-2) that takes Al or Al alloy as the base material, and another fiber with the trade name SCS-6 (referred to as SCS-6) that takes Ti or Ti alloy as the base material were developed. The structure of these fibers has a C core about 30  $\mu\text{m}$  in diameter, and the surface is covered with SiC that is deposited by CVD. What should be noted is that SCS-2 and SCS-6 are given special surface coat treatment aimed at enhancing matchability with the base metal. The composition distribution of the surface portion is shown in Figure 1. The figure shows the relationship between the distance toward the center of the fiber, with the surface of the fiber as the origin, and the composition, as determined by Auger analysis. As can be seen, the interior of SCS-2 and SCS-6 has the composition of SiC with the ratio of Si:C approximately equal to 1:1, but the fiber surface has a C-rich composition for both samples, with the maximum concentration being roughly equal for both fibers. However, SCS-6 has a C-rich layer whose thickness is about twice as large as SCS-2, and at the midsection in the direction of thickness of the C-rich layer, that portion about 2  $\mu\text{m}$  from the surface has a slightly larger amount of Si than in SCS-2.

Table 1. Kinds and Characteristics of CVD Fibers

Kind	Density $\text{Mg/m}^3$	Tensile strength $\text{GPa}$	Elastic modulus $\text{GPa}$	Dia- meter $\mu\text{m}$	Manufac- turer
B	2.31	3.24	402	142	AVCO
B <sub>4</sub> C/B	2.34	3.42	402	142	AVCO
SiC/B	2.32	3.24	402	142	CTI
SiC	3.44	3.43	358	142	AVCO
SCS-2	3.44	3.43	358	142	AVCO
SCS-6	3.44	4.08	358	142	AVCO

However, the strength of the SCS-6 fiber was slightly higher than other fibers.

### 2.1.2 Metals for Base Material

As the base metals, basically two configurations were used. One is used mainly for the manufacture of single fiber composites, which is shot-formed pure Ti which is fully degassed for HCD type evaporation of the PVD method. As the alloying element in the formation on the fiber surface with Ti alloys as the

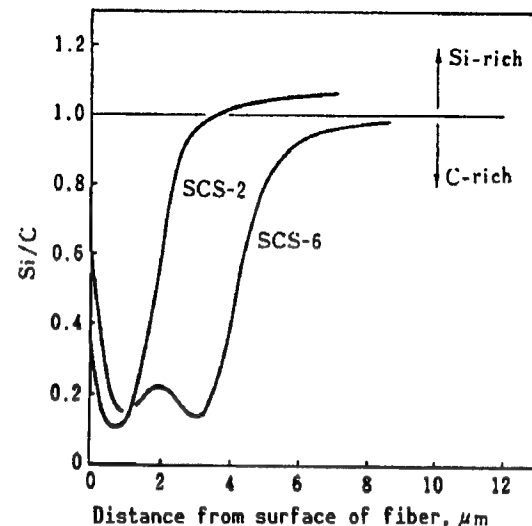


Figure 1. Composition in the Neighborhood of Fiber Surface by Auger Analysis

The mechanical characteristics of these CVD fibers are shown in Table 1. The density of the B system fiber is about 2.3  $\text{g/cm}^3$  and the density of the SiC system is about 3.4  $\text{g/cm}^3$ . In brittle fibers such as the CVD fibers, there were large irregularities in the strength measurements, giving different values for different samplings. How-

base material by the above-mentioned method, Ni of 4-nine, Cu and Al of 5-nine, and V and Mo of 3-nine were used. For the manufacture of composites by double coating, an electroless plating solution that uses nickel sulfate and copper sulfate as the base was used.

For the manufacture of Ti based massive composites, it is not possible to use the liquid phase method because Ti is active and the melting point of Ti is as high as 1670°C. The solid phase method must be used, but in this method it is necessary to prepare the foil or powder of the metal that serves as the base material. As the base material, pure Ti foils made domestically and the U.S.-made Ti-6Al-4V foils as alloy foils are readily available. In this research both types of foils with a thickness 70 μm were used.

The Ti alloys (except for Ti-6Al-4V) are not readily available for both foil and powder. Therefore, in studying the effect of Mo, a layer containing Mo was arranged on a Ti-6Al-4V alloy foil. To manufacture this sample, a Ti-6Al-4V alloy foil was first thinned by 12 μm by chemical polishing that uses a mixture of nitric acid and hydrofluoric acid. Next, both the front and rear surfaces of the alloy film were coated with Ti-Mo alloy 6 μm thick to yield a total thickness of 70 μm, which is the same as the thickness of the original alloy foil. This coating was done by the PVD method. The concentration of Mo in the coated layer obtained was 7.5 wt%.

## 2.2 Manufacturing Method of Composites

### 2.2.1 Manufacture of Single Fiber Composites

In order to examine the compatibility between the CVD fiber and the metallic or alloy base material, it is necessary to manufacture composite materials. For the industrial manufacture of FRMs the solid phase method or the liquid phase method can be used. In these methods, it is usual to form powder or foil in which a large number of fibers are appropriately dispersed by hot press or HIP. In these techniques it is difficult to control the surface conditions of the fibers and the metal, and severe damage may possibly be done to the fibers at the time of the formation. It is also possible that the fiber surface could be contaminated in the preparatory stage for formation or at the time of the formation, and this contamination impedes the examination of the surface reactions.

In order to avoid these problems, Ti or Ti alloy was deposited on the surface of the CVD fiber by using a hollow cathode discharge (HCD) type physical vapor deposition (PVD) system as shown in Figure 2. for the case of coating with an alloy, a predetermined amount of alloying metallic element to be mixed with Ti

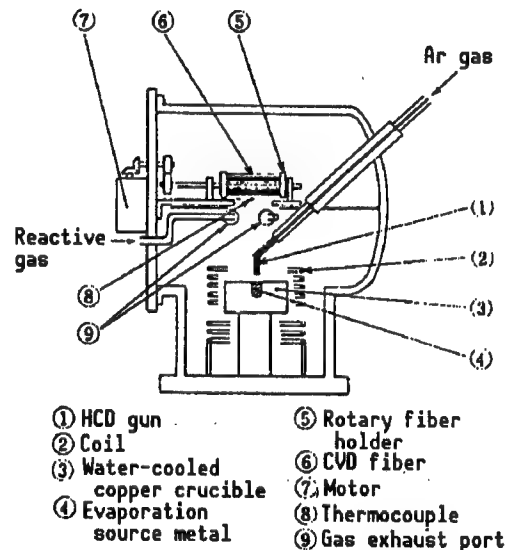


Figure 2. HCD Type PVD System

is melted along with Ti in a water-cooled copper crucible prior to evaporation, and held until a sufficiently homogenized mixture is obtained. The fiber is set in a holder, and it is uniformly coated with the metal by rotating the holder. The coated fiber is a single fiber composite which contains just one thread of the fiber.

In manufacturing a composite of double coating, a metal such as Ni or Cu was deposited on the fiber by electroless coating. Next, a composite whose base consists of two layers was manufactured by coating the surface of the sample with Ti (or its alloy) by the PVD method.

### 2.2.2 Manufacture of Massive Composites

As the reinforced fiber of massive composite, only the case of SCS-6 which yielded satisfactory results in the single fiber composite was studied. By arraying the fibers equidistantly at  $142 \mu\text{m}$  intervals, a cord-fabric-shaped sample was obtained.

A massive composite was formed by alternately laminating the arrayed SCS-6 fabric and a Ti or Ti alloy foil, and hot pressing the sample in a vacuum of about  $2 \times 10^{-3}\text{Pa}$  under the conditions of 1183 K, 30 MPa, and 1.8 ks.

The FRM thus obtained has high strength, and if an ordinary shaped testpiece is used for tensile test, testing will be difficult. Therefore, a pure Ti plate 1 mm thick was arranged on the upper and lower surface when forming the composite to join by diffusion the portions that serve as tabs. The dimensions of the formed material are: 110 mm long x 50 mm wide x 3 mm thick. Of the 3 mm thickness, each 1 mm on the upper and lower surfaces containing Ti alone is the portion that makes up the tab, and the reinforcing fiber is contained only in the portion 1 mm at the center. A testpiece for the tensile test was prepared by segmenting a portion 10 mm wide from the above material, and scraping off the pure Ti portion while taking care not to damage the fiber portion. The planar and side shapes of the testpiece is shown in Photograph 1 [not reproduced].

## 3. Results and Consideration

### 3.1 Change in Strength of the Material Due to Heat Processing

#### 3.1.1 Reinforced Fibers

To study the influence of heating on the mechanical characteristics of a composite it is necessary to first know about the change in the strength in the case of heating the single fiber alone. For this reason, the relationship between the heating temperature and the strength was studied in the case where such a fiber alone was heated in a vacuum of  $1 \times 10^{-3}\text{Pa}$ , over the temperature

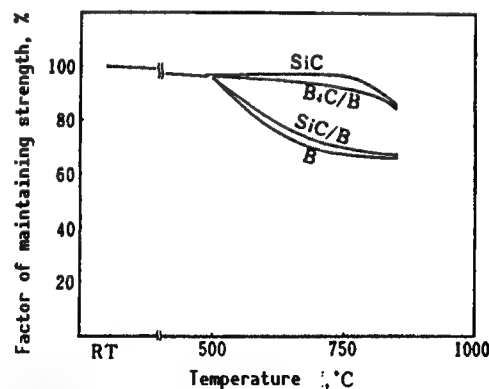


Figure 3. Change in Strength by Heat Processing of Fiber Alone (Holding time of 3.6 ks)

range up to 1123 K ( $850^{\circ}\text{C}$ ) which is the manufacturing temperature of the Ti (or its alloy)-based FRM, for 3.6 ks. The result is shown in Figure 3. The SiC system fiber in the figure is one without surface treatment. In the figure, the fiber strength after heating is represented by the relative strength based on "as-received" fiber strength of 100 percent. As seen in the figure, the strength deteriorates by heat processing in all the fibers. In particular, the B fiber and the SiC/B fiber show conspicuous deterioration, and the strength maintaining factor at  $750^{\circ}\text{C}$  is about 70 percent of the original fiber strength. In contrast, the  $\text{B}_4\text{C}/\text{B}$  fiber and the SiC fibers show smaller degrees of deterioration, showing a strength maintaining factor of 85~90 percent even at  $850^{\circ}\text{C}$ . The SCS-2 and SCS-6 have basically the same structure as the SiC fiber which is not surface treated except for the surface treatment aimed at enhancing capability, and the maximum deterioration of the strength during the high temperature heat processing is comparable to that of the SiC fiber without surface treatment, which means that ordinarily no deterioration occurs.

This situation is illustrated in Figure 4. This figure shows the result of the fiber strength distribution against the heating time when the SCS-6 fiber is heated in a vacuum of  $2 \times 10^{-3}\text{Pa}$  at a constant temperature of 1123 K for the change of heating time up to 360 ks. As shown, no deterioration in strength is observed even when heating for 360 ks, and the Weibull coefficient shows an increase. In other words, the change in the strength of the SCS-6 fiber single body by heating is extremely small.

### 3.1.2 Metals for Base materials

For the single body base metals, the change in the strength by heating was similarly studied. In this case, the sample was heated in a vacuum of  $2 \times 10^{-3}\text{Pa}$  at the constant temperature of 1123 K by changing the time up to 360 ks. The result is shown in Figure 5. As can be seen from the figure, "as-received" pure Ti foil has a strength of 500 MPa and the Ti-6Al-4V alloy foil has the strength of about 105 MPa. When these materials are heated, a gradual deterioration of the strength occurs up to the time of heating of 126 ks, but up to 360 ks hardly any change was observed. The eventual strength maintaining factor was about 84 percent for the pure Ti and about 88 percent for Ti-6Al-4V alloy foil. It was made clear that by heating metallic single bodies no deterioration is generated which will significantly affect the strength of the FRMs.

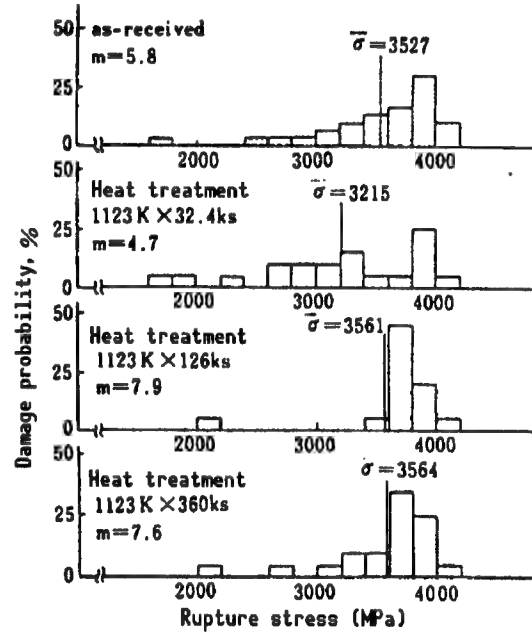


Figure 4. Strength Distribution of SCS-6 Fiber (Dependence on heat treatment; gauge length is 50 mm)

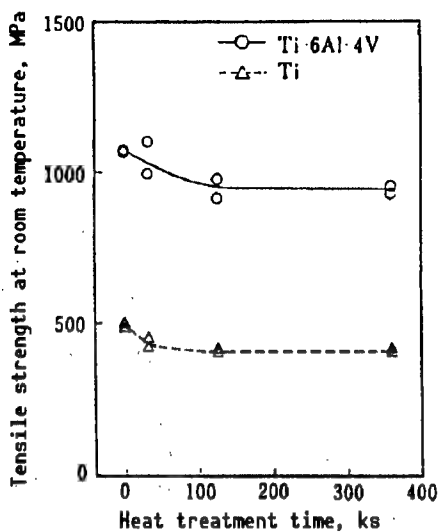


Figure 5. Strength Characteristics of Matrix Metals

(Heating temperature: 1123 K)      3.2 Single Fiber Composites

As described in the above, the deterioration in strength of the B fiber and the SiC/B fiber is conspicuous even in the heat treatment of the fiber single body. With this basic knowledge, we studied the change in strength by heat treatment of single fiber composites. The conditions of heat treatment were: change of temperature up to a maximum of 850°C and a constant heating time of 3.6 ks. These conditions of 850°C and 3.6 ks correspond to the thermal conditions when forming the CVD fiber reinforced Ti (or its alloy) composite. Figure 6 shows the result of measuring the strength of the single fiber composites versus heating temperature. As seen from the figure, the B fiber has the strength maintaining factor of only 80 percent at 500°C and about 50 percent at temperatures above 750°C.

On the other hand, in the SiC/B fiber, a strength of more than 90 percent is maintained at 500°C, but it drops to about 60 percent at 750°C and about 50 percent at 850°C. In contrast, the B<sub>4</sub>C/B fiber and the SiC fibers maintain the strength of 70~75 percent even at 850°C. In the case of coexistence with Ti, similar to the case of heating the fiber separately, the latter two materials show a strong resistance to strength deterioration. In either case, heating the composites yields considerably more deterioration than heat treatment of single fibers. Such a deterioration is caused by the surface reactions. Although there is a more detailed discussion about the surface conditions in the section on massive composites to be presented later, it can briefly be mentioned that the deterioration of the strength is more conspicuous when the thickness of the reaction layer is larger.

### 3.2.2 Modification of Base Material in Single Fiber Composites

In the composites that use pure Ti as the base material there is induced surface reactions when they are subjected to heat treatment in combination with any kind of fibers, which results in a marked deterioration of strength.

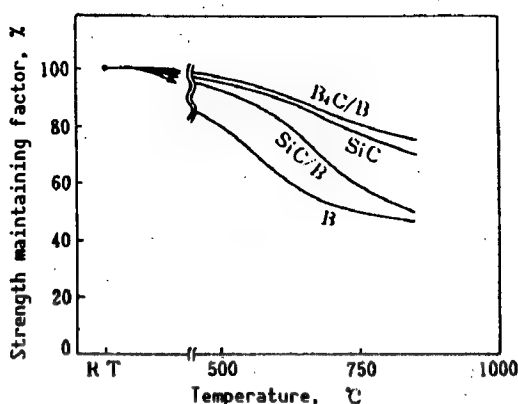


Figure 6. Change in Strength Due to Heat Treatment of Ti-Based Single Fiber Composites

In this subsection we will describe the modification of the base materials aimed at improving resistance to strength deterioration and the suppression of the surface reactions. What is meant by modification here is to reduce the reactivity to the fiber by changing the characteristics of the base material by adding an alloying element, etc., to the Ti base material. In this case, it is desirable that the added element form a solid solution with all of the Ti crystal grains, and reduce the reactivity uniformly over the entire Ti base material. The reduction of the activity includes:

- (1) To have the reaction with Ti completed in advance by adding elements that constitute the fiber.
- (2) To stabilize Ti by adding an alloying element which has a bonding force stronger than the affinity between Ti and the constituent element of the fiber.
- (3) To form a protective film for the fiber by adding an element which can form a compact compound with the constituent element of the fiber.
- (4) To reduce the reactivity of Ti by adding an element which has smaller affinity than Ti has for B, Si, and C of the constituent elements of the fiber, etc.

As a possible element to be added, one may first consider the constituent element of the fiber listed in (1) above. However, B does not form a solid solution with Ti, and C and Si form a solid solution with  $\alpha$ -Ti only 0.5 and 0.4 wt%, respectively. The constituent elements of the fiber mentioned above form compounds with Ti, such as  $TiB$  (decomposition temperature  $2060^{\circ}C$ ),  $TiB_2$  (MP  $2790^{\circ}C$ ),  $Ti_5Si_3$  (MP  $2120^{\circ}C$ ),  $TiSi$  (decomposition temperature  $1760^{\circ}C$ ),  $TiS_2$  (MP  $1540^{\circ}C$ ), and  $TiC$  (MP  $3250^{\circ}C$ ) that are hard and brittle. These melting points are rather high which suggests that their bonding force is also rather strong. When the constituent elements of the fiber are added at Ti, a state in which compounds are dispersed in the Ti base material tends to form. Accordingly, Ti in the portions where the compounds are not formed is not affected by the added element, thus reduced reactivity cannot be expected. It is likely that these compounds are distributed rather nonuniformly, and may become the starting points of fracture. In order to aim at reducing the reactivity by converting Ti to compounds by adding elements other than the constituent elements of the fiber, it is necessary to turn the entire Ti to compounds in which case no Ti alloy base material is obtained. From the above, addition of the constituent elements of the fiber, etc., is considered inappropriate.

In the case of (2), there can be found no element for which one can expect to suppress the formation of compounds by alloying. The reason for this is that the bonding force in alloying is smaller than the bonding force in the formation of the ordinary compounds.

In order to form a protective fiber as mentioned in (3), the element to be added to Ti must have an affinity which is greater for the constituent elements of the fiber than for Ti. As such an element, for C which is a

constituent element of the fiber, one can think of Zr at room temperature. The difference in the formation energies is small. In addition, for temperatures of 1600~1700°C one can think of Ta and Mo, but this temperature range far exceeds ordinary temperature formation, thus such elements are not practical.

As to (4), examples of elements which form solid solutions with Ti, and do not weaken the characteristics of Ti, are Al, Cr, Mo, Sn, V, Zr, etc., These are the elements to be added to Ti to form ordinary alloys. In addition, Cu and Ni are limited to forming solid solutions in  $\alpha$ -Ti, but they form solid solutions with  $\beta$ -Ti to maximum values of 17 and 13 wt%, respectively. The result of selecting these elements which make it possible to form alloys for the single fiber composites by electroanalysis or HCD type PVD method, and studying the surface reaction rates is shown in Figures 7(a) to 7(d). The doubly coated samples of Cu and Ni, obtained by first coating the fiber with these elements by electroless deposition method, then coating the samples with Ti by a PVD method is also included in the figure. In the figure, the sample obtained by coating with x wt% of an element A is represented by Ti-xA, and the sample obtained by double coating is represented by A+Ti.

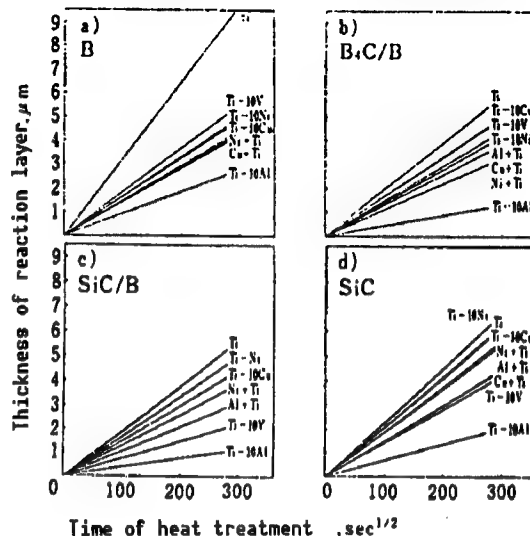


Figure 7. Change in Thickness of Reaction Layer Against Heating Time of Single Fiber Composites (heating temperature of 850°C)

Table 2. Reaction Products of Single Fiber Composites

Base material Fiber	Ti	Ti-10Al	Ti-10V	Ti-10Cu	Ti-10Ni
B	TiB <sub>2</sub>	(Ti, Al)B <sub>2</sub>	(Ti, V)B <sub>2</sub>	(Ti, Cu)B <sub>2</sub>	(Ti, Ni)B <sub>2</sub>
	TiB	(Ti, Al)B	(Ti, V)B	(Ti, Cu)B	(Ti, Ni)B
B <sub>4</sub> C/B	TiB <sub>2</sub>	TiC	(Ti, V)B	(Ti, Cu)C + (Ti, Cu)B	TiC + (Ti, Ni)B
	TiB(C)		(Ti, V)+(C)		
	TiC(B)				
SiC/B	TiB	Ti(C)	(Ti, V)C + (Si)	(Ti, Cu)B	TiC(B)
	TiB+TiC	(Ti, Al)(C)	(Ti, V) <sub>5</sub> Si <sub>3</sub>	(Ti, Cu) <sub>5</sub> Si <sub>3</sub> + (Ti, Cu)C	(Ti, Si))
	TiC(B)				
SiC	TiC + Ti <sub>5</sub> Si <sub>3</sub> (C)	TiC (Ti, Al) <sub>5</sub> Si <sub>3</sub>	(Ti, V)Si + (Ti, V)C (Ti, V) <sub>5</sub> Si <sub>3</sub>	(Ti, Cu) <sub>5</sub> Si <sub>3</sub> + (Ti, Cu)C	(Ti, Ni) <sub>5</sub> Si <sub>3</sub> + TiC

Note: TiB(C) means that "C is dissolved solidly in TiB." (Ti, Al)B means that "a part of Ti sites of TiB is replaced by Al." Similarly for others.

As can be seen, addition of Al into Ti is effective for the B fiber and the B<sub>4</sub>C/B fiber, and addition of Al or V into Ti is effective for the SiC/B fiber and the SiC fiber. These are the elements which stabilize the  $\alpha$ -phase or three-point bending phase of Ti.

The result of electron probe microanalysis (EPMA) on these surface reaction products will be described in detail in the section on massive FRMs that will be presented later. Here, we will simply list the kinds of compounds from the composition ratios obtained by EPMA.

The reaction products have the compound of Ti and the constituent elements of the fiber as a base, and have a composition in which the added element is dissolved solidly into the compound.

The reactivity of the SiC, SiC/B, and SiC fibers is low, but the first two are not readily available now. A highly stable fiber that is now available is the SiC fiber. Similar examination was carried out for SCS-2 and SCS-6 which are the fibers of the SiC system. The result is shown in Figure 8. Shown also in the figure is the result of adding a number of alloying elements to Ti. As can be seen, the reactivity of SCS-6 is low and hence stable. The effect is stronger when these alloying elements are combined.

### 3.3 Massive Composites

The result regarding single fiber composites is applicable to composites that are manufactured in ideal conditions. However, in the actual composites, contamination of the interfaces at the time of formation and interference between the fibers at the time of reaction are involved. In order to apply the result of the single fiber composites to the actual composites, it is necessary to examine the relationship between the surface conditions and the strength of the massive composites which include numerous fibers of different configurations similar to the actual composites.

#### 3.3.1 Surface Conditions of Massive Composites

##### 3.3.1.1 Structure of the Interface

A sectional view of a pure Ti-based composite obtained by hot-pressing is shown in Photograph 2 [not reproduced]. Photograph 3 [not reproduced] is a high magnification photograph of a cross section of a composite in which Mo is arranged. In this photograph, the area surrounding the fibers and the central part of the base material which is light gray and gently undulating is the Mo-Ti alloy layer with Mo arranged in it. Although the interface conditions in this case will be described in detail later, we will simply mention that several reaction products are seen.

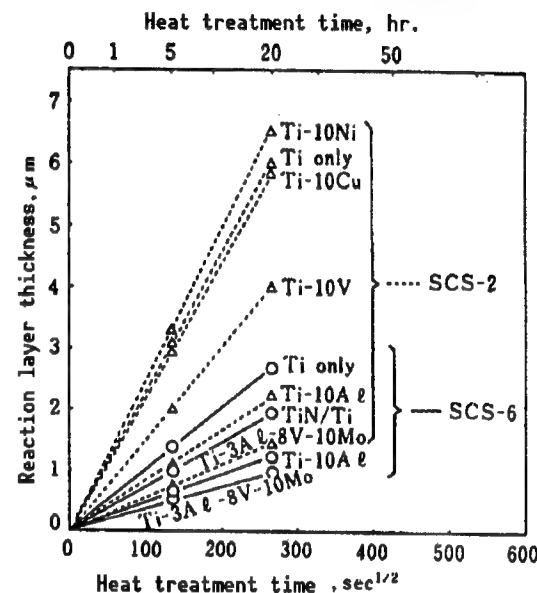


Figure 8. Change in Thickness of Reaction Layer Vs. Heat Treatment Time of Single Fiber Composites (heating temperature of 1123 K)

The above testpiece was heat treated in a vacuum of  $2 \times 10^{-3}$  Pa at 1123 K for 32.4 ks, 126 ks, and 360 ks. The cross section of the testpiece was polished, observed by optical microscope and scanning electron microscope (SEM), and the reaction products at the interface of the fiber and the base material were examined by EPMA. After cooling, the testpiece was subjected to a tensile test.

The interface between the fiber and the base material when the FRM is given heat treatment is shown in Photograph 4 [not reproduced]. The black portion on the right-hand side of each photograph is part of the fiber, and the white portion on the left-hand side is part of the base material. The thin white line in the vicinity of the surface of the fiber is the boundary of the areas with different compositions in the interior of the C-rich portion on the surface of SCS-6 that will be described later. In massive composites are also seen gray reaction layers at the interface of the fiber and the base material. The thickness of the reaction layer increases with the lapse of time. However, the distribution of Mo in a composite with Mo arranged in it hardly changed even after heat treatment for 360 ks as may be observed from Photograph 3. A comparison of the thickness of the reaction layer for various kinds of base material shows, in the Ti-6Al-4V alloy foil base material and the base material obtained by arranging Mo to the Ti-6Al-4V, that the growth of the reaction layer was smaller than in pure Ti, showing an apparent reaction suppressing effect of the added element. For all base materials where the formation of a reaction layer was observed, fluctuations of about 20 percent in thickness were seen.

### 3.3.1.2 Composition Distribution in the Vicinity of Interface

The result of identification of the conditions of these interfaces by means of EPMA is shown in Figure 9. First, the structure of the surface of the SCS-6 fiber will be described. As can be see in the as-fabricated sample, a portion with high C concentration about 4  $\mu\text{m}$  thick is clearly formed. The concentration of C is not uniform within the range of 4  $\mu\text{m}$ , and a three-layer structure with an area of somewhat smaller concentration of C in the mid-section is formed. Corresponding to this it is observed that the detected concentration of Si also has a three layer structure. This result approximately corresponds to the situation shown in Figure 1.

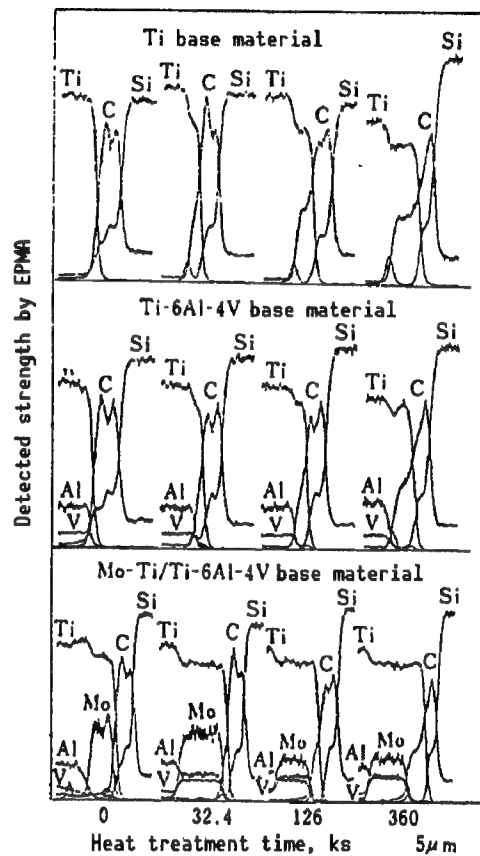


Figure 9. Change in Interface Composition as Function of Heating Time of SCS-6 Fiber Reinforced Ti (or its alloy)-Based Massive Composites (heating temperature of 1123 K)

When these samples are subjected to heat treatment at 1123 K for 32.4 ks, a shoulder appears in the detected line of Ti in the pure Ti base material, and a peak of Si is observed at the corresponding position. From the analysis of the detected intensities by EPMA it was seen that this portion has a composition corresponding to a compound  $Ti_5Si_3$ . In addition, there exists a compound that corresponds to  $TiC$  at the interface of  $Ti_5Si_3$  and the  $SiC$  fiber. For  $Ti-6Al-4V$ , the thickness of the reaction layer is smaller than in pure Ti. Small amounts of solid solution of Al and V were observed in the reaction layer. The situations for C, Si, and Ti are approximately the same as in the case of pure Ti. When Mo is arranged, it was observed that Al and V diffused to positions where Mo existed in the interface with lapse of heating time. In the layer where Mo exists, the concentration of  $SiC$  which is a constituent element of the fiber is small. On the other hand, the concentration of Mo showed a tendency to decrease over time, but the change is small, and the diffusion of Mo  $Ti-6Al-4V$  and the fibers is small.

These results correspond to what is shown in Photograph 4 [not reproduced] thus it is possible to show the range of the reaction layer. Figure 10 shows the mean thickness of the reaction layer as a function of the square root of the reaction time ( $t$ ). Within this range of time, the relation can tentatively be regarded as a straight line, and the thickness of the reaction layer is small compared with the fiber diameter, thus it is suggested that this reaction determines the diffusion rate.

### 3.3.2 Strength of Massive Composites

Next, the influence of heat treatment on the strength of massive composites will be described. The change in the strength as a function of the holding time in the case of holding in vacuum at 1123 K is shown in Figure 11. As can be seen from the result, the strength of the as-fabricated composites is 1500 MPa for pure Ti, 1900 MPa for  $Ti-6Al-4V$  alloy foil, and 2050 MPa for  $Mo-Ti/Ti-6Al-4V$ . When these samples were heat treated at 1123 K, the change was minor for

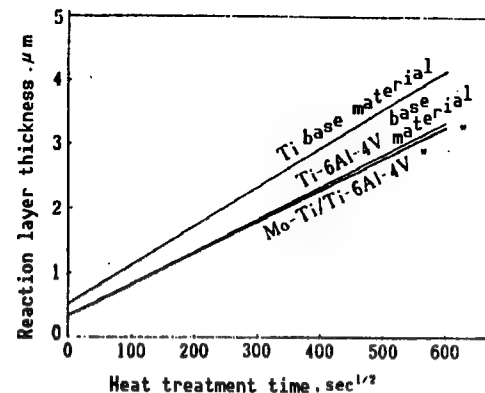


Figure 10. Change in Thickness of Reaction Layer as Function of Heat Treatment Time of SCS-6 Fiber Reinforced Ti (or its alloy)-Based Massive Composites (heating temperature of 1123 K)

the first 300 seconds of heat treatment.

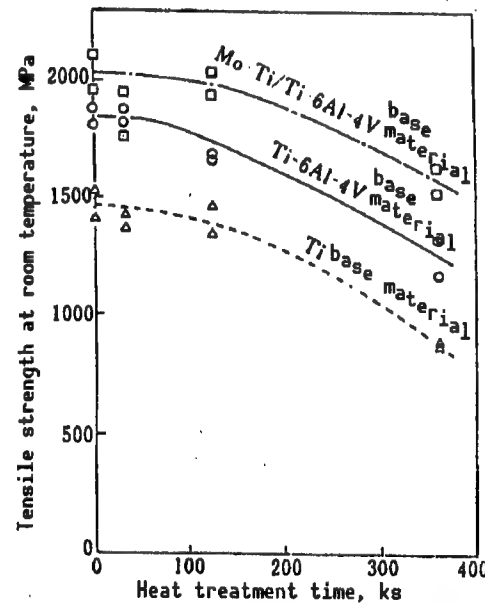


Figure 11. Strength Change at Room Temperature as Heat Treatment Time of SCS-6/Ti (or its alloy) Massive Composites (heating temperature of 1123 K)

all base materials up to 126 ks, but strength deterioration was conspicuous at 360 ks. It can be seen that the degree of deterioration is relatively small when Mo is arranged.

When the deterioration in strength is represented with the strength of the as-fabricated sample as 100 percent, the strength maintaining factor at 360 ks is about 60 percent for pure Ti, about 70 percent for Ti-6Al-4V, and about 80 percent for Mo-Ti/Ti-6Al-4V. That is, modifying the base material by the addition of alloying elements has a large effect in suppressing the deterioration of FRMs. According to Figure 9, there is little difference between the reaction layers of Ti-6Al-4V and Mo-Ti/Ti-6Al-4V. At present, the reason for this is not clear, but it is definite that the case of arranging M has smaller deterioration than the case of Ti-6Al-4V alone.

#### 4. Conclusion

By focusing attention on CVD fiber reinforced composites as FRMs that are light weight and high strength and have resistance to heat of medium intensity, basic study was done on the compatibility between the fiber and the base material which was modified.

As a result, in heating single body fibers it was found that SCS-6 which is a fiber of the SiC system, has the smallest deterioration. Both of the base materials of Ti and Ti-6Al-4V showed small deterioration.

With FRMs that have pure Ti as the base material, TiC in the proximity of the fibers and  $Ti_5Si_3$  is generated on its outside. The strength of the FRMs tended to decrease as the thickness of these reaction layers increased.

As elements to be added to suppress the surface reactions and deterioration at high temperatures, Al, V, Mo, etc., which stabilize the  $\alpha$ -phase and the  $\beta$ -phase of Ti were effective. The addition of a number of these elements enhanced the suppression of the reactions. The reaction products in the case of alloy base materials are approximately the same as the case of using pure Ti as the base material, basically TiC and  $Ti_5Si_3$ , and those having Al, V, Mo, etc., as solid solution in these basic products.

The deterioration of the strength is closely related to the thickness of the reaction layer, cases which cannot be discussed in terms of the thickness of the layer alone also exist.

## **High-Performance Crystal Control Alloy R&D**

916C0048E Tokyo KENKYU HOKOKUSHU 12 in Japanese 1991 Issue pp 135-152

[Research funded by other agencies, FY82-FY88]

### **[Text] Abstract**

This research is part of the "R&D Project of Technology for Future Industries," MITI, and our Institute carried out alloy development in items (1) and (2) below and evaluation tests in items (5) and (6).

**(1) Superhigh heat-resistant single crystal alloys (Ni-based):** To construct an alloy designing method based on component analysis of the equilibrium phases by electron probe microanalysis (EPMA), and proposed alloys which exceed the official goal by considering the lattice constant mismatch, etc.

**(2) Oxide particle dispersed reinforced alloys (Ni-based):** Developed alloys with  $\gamma'$  quantity of 55 and 65 percent, etc. These alloys have creep fracture strength that far exceeds the goal, but the elongation is somewhat less than the goal. Alloys of this system are defective in that their creep fracture strength at an intermediate temperature of about 1073 K is lower than that of the single crystal alloys, but alloys with higher  $\gamma'$  content were more advantageous in this respect.

**(3) Ni-based heat-resistant superplastic alloys:** Tried to develop superplastically processable alloys with materials to be used for a gas turbine disk. Although a large number of alloys that are superplastically processable were obtained, it was not possible to achieve the goal of strength at 1033 K which is the temperature at which it will be used. However, much information was accumulated on the influence of the  $\gamma'$  quantity, amount of B addition, HIP, etc.

**(4) Ti-based superplastic alloys:** Designed alloys with the ratio of 1:1 for the ratio of quantities of the  $\alpha$ - and  $\beta$ -phases in order to obtain alloys which are superplastically processable in the range of 973~1073 K, and have a high specific strength at 573 K. For estimating the composition of the phases, thermodynamic techniques in addition to a technique that uses empirical formulas were used. Several alloys which far exceed the goal were obtained.

(5) Evaluation of fatigue characteristic at high temperatures: Various information was obtained by evaluating low cycle fatigue characteristics of Ni-based single crystal alloys and Ti alloys. For example, in the Ni-based single crystal alloys, the fatigue strength decreases when the compatibility of the interface between the  $\gamma$  and  $\gamma'$  phases is lost.

(6) Evaluation of corrosion resistance: Corrosion resistance by sulfiding at high temperature Ni-based single crystal alloys was evaluated by a burner rig tester. It was shown that Mo has less negative effect in corrosion resistance than W. In cooperation in this project, research on manufacturing proposed alloys was carried out by other research organizations, and many valuable results were obtained. We also helped put these results into a database.

## 1. Introduction

As a national project related to materials, research was done on "high-efficiency gas turbines" and "high-performance crystal control alloys." In the first project, research on two kinds of Ni-based superhigh heat-resistant alloys was carried out from FY78 to FY84. In the latter, research on three kinds of Ni-based alloys and one kind of Ti-alloy was carried out from FY81 to FY88. Both projects were sponsored by the Science and Technology Agency. In the first project, research on Ni-based ordinary cast alloys for moving blades and stationary blades that are components of the highest temperature in gas turbines and research on the manufacture of air-cooled moving blades and air-cooled stationary blades using these components were carried out. Research on Ni-based unidirectionally solidified columnar crystal alloys and on the manufacture of the air-cooled moving blades made of unidirectionally solidified columnar crystal alloy was also carried out.

In the second project which relates to this report, this Institute was in charge of developing higher performance Ni-based single crystal alloys and Ni-based particle dispersed reinforced alloys for the moving blades of gas turbines and jet engines, similar to the first project, and other organizations carried out research on the manufacture of turbine blades by using the alloys developed by our Institute.

Research on Ni-based superplastic alloys and the process aimed at the manufacture of the turbine disk for gas turbines or jet engines, and research on the development and the process of superplastic high strength Ti alloys aimed at manufacturing disks for the compressor of gas turbines, were carried out. Similar to the above two cases, this Institute was in charge of developing alloys.

## 2. R&D on Superhigh Heat-Resistant Single Crystal Alloys

### 2.1 Foreword

Ni-based superhigh heat-resistant single crystal alloys are alloys developed in the 1970s, and their strength at high temperatures is far superior to that of the columnar crystal alloys that have the highest strength.

The characteristic of the process is that after unidirectionally solidifying a single crystal, it is possible to completely melt the solidified structure and eliminate the solidified segregation by subjecting the sample to heat treatment at high temperature, then uniformly reprecipitate and disperse the  $\gamma'$  particles. Because of this, the content of the interface reinforcing elements (C, B, Zr, and Hf) which are contained in the polycrystalline and columnar crystal alloys and obstruct the complete melting can be regulated to the order comparable to that of the impurities.

In the R&D Project for Future Industries, a goal was set "to develop alloys which can withstand a stress of 137.3 MPa for longer than 3.6 Ms in a high-temperature of 1313 K, and which has a fracture elongation greater than 10 percent at that time" which was a development goal that exceeded the world level when the project began. The research was aimed at developing alloys that satisfy the target performance by using a testpiece component in the first half of the period and a complex shape component in the second half of the period. For alloy development, the alloy design method developed for ordinary cast Ni-based heat-resistant alloys was applied. In the beginning, alloy design was carried out by focusing attention on the volume fraction of the  $\gamma'$  phase which strongly affects the creep fracture strength, the amount of Ta, W, and Mo in the  $\gamma'$  phase, the solution index (SI) which strongly affects the structure stability, etc. In the latter half, alloy design was carried out by considering the lattice constant mismatch which was shown to have a strong influence on the strength on the high temperature side, and aimed at reducing the specific gravity of the alloys. We succeeded in developing a large number of alloys that have performance that exceeds the development goal.

Moreover, the composition of the  $\gamma$  and  $\gamma'$  phases in the heat-treated phase of 30 kinds of alloys including the newly developed and already available alloys using EPMA was analyzed. We succeeded in refining the part in the phase equilibrium computation of the old alloy design program. With this success, the formula for estimating longevity before creep fracture for single crystal alloys was updated, and we obtained a new version of the alloy design method. We succeeded in developing alloys effectively with excellent specific strength by the new alloy design method.

## 2.2 Experimental Method

A single crystal of designed alloy was prepared by pouring molten metal at 1820 K obtained by melting raw materials or a melting stock into a casting mold having a lower opening heated at 1773 K held on a water-cooled copper plate, then unidirectionally solidified by a method which draws the mold downward at a speed of 0.056 mm/s. After measuring the temperature range for solution treatment and confirming the presence/absence of harmful phases through observing the structure of heat-treated materials, a creep fracture test was carried out to test pieces that were subjected to solution annealing and through heat treatment under the conditions of 1073 K and 735.5 MPa, and 1313 K and 137.3 MPa.

### 2.3 Influence of $\gamma'$ Volume Fraction and Ta/W Ratio in $\gamma'$ Phase

Ten kinds of alloys based on the high strength alloy TM-210 developed for ordinary cast alloys and having different  $\gamma'$  volume fraction and Ta/W ratio in the  $\gamma'$  phase were designed, and their characteristics were evaluated. The result is shown in Figure 1. In TMS-15 and 18 alloys on the high W side of the alloy system with  $\gamma'$  volume factor of 75 percent, the precipitation of the  $\alpha$ -W phase was observed and the equilibrium between the  $\gamma$  and the  $\gamma'$  phases was destroyed. In the alloy system with  $\gamma'$  volume factor 65 percent, the precipitation of the  $\alpha$ -W phase took place during solution heat treatment of TMS-2 on the high W side, lowering the stability of the two-phase equilibrium structure. The creep fracture of TMS-1, 2, 6, 12, 16, and 17 exceeded the development goal. Of these, TMS-1 had an excellent creep fracture strength which exceeds the characteristic of the first generation single crystal alloys. Alloy 454 and NASAIR100 over the wide range of 1073~1313 K (Figure 2).

### 2.4 Influence of the Solution Index

The TMS-1 and TMS-12 which have excellent structure stability and strength characteristic were proposed for evaluation in the first half period. These alloys are strengthened by the precipitation of the  $\gamma'$  phase and their maximum strength for solid solution was achieved by using Ta and W.

As a result, the structure became unstable depending upon the conditions of the charger for manufacturing, therefore, the quality of test-manufactured alloys turned out to be far inferior to the quality anticipated. As a result of observing the composition and analyzing the constituents, it was clear that the reason for this is caused by the variation in the solution index (SI). Therefore, we designed alloys which have the same Ta/W ratio but have three values 1.4, 1.3, and 1.2 of the SI by varying the amounts of Ta and W, and evaluated the alloys. After a solution treatment, precipitation of  $\alpha$ -W was observed in the three alloys of TMS-31, 32, and 12-1. The amount of the precipitation was the highest in TMS-31, and the amounts in TMS-32 and 12-2 were small and comparable. The creep fracture strength characteristic is shown in Table 1. At 1313 K, the strength of the

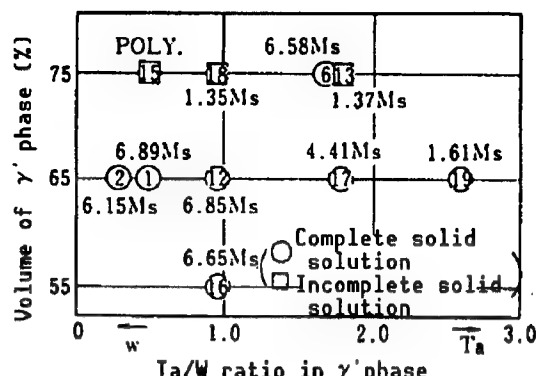


Figure 1. Solution Conditions of Developed Alloys and Influence of  $\gamma'$  Amount and Ta/W Ratio in  $\gamma'$  Phase on the Creep Fracture Life Under 1313 K and 137.3 MPa

of these, TMS-1 had an excellent creep fracture strength which exceeds the characteristic of the first generation single crystal alloys. Alloy 454 and NASAIR100 over the wide range of 1073~1313 K (Figure 2).

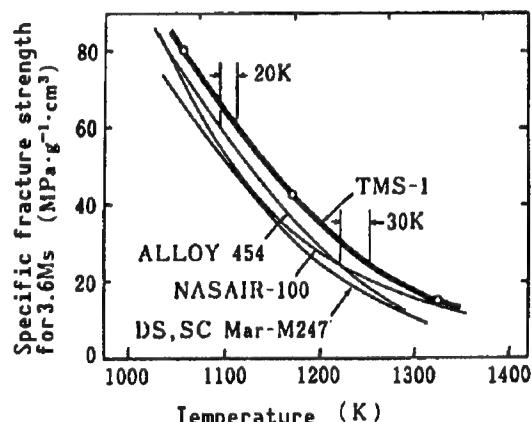


Figure 2. Comparison of Specific Strength Between Developed Alloy TMS-1 and Existing Alloys Alloy 454 and NASAIR100

Table 1. Creep Fracture Strength of Improved Alloys

Alloy	1073 K, 735.5 MPa			1313 K, 137.3 MPa		
	Life (ks)	Elonga- tion (%)	Contraction factor of cross section (%)	Life (ks)	Elonga- tion (%)	Contraction factor of cross section (%)
TMS-31 SI = 1.4	885.6	16.3	19.3	4114.8	17.3	47.6
	849.6	23.7	32.7	4690.8	16.0	49.5
TMS-32 SI = 1.3	414.0	32.3	29.9	5292.0	18.3	42.7
	1494.0	26.3	29.9	5385.6	19.9	44.9
TMS-33 SI = 1.2	1090.0	24.7	25.8	3142.8	18.7	56.3
	813.6	25.7	29.4	3366.0	27.0	48.9
TMS-12-1 SI = 1.4	565.2	30.0	36.5	10414.8	14.3	49.6
				10717.2	15.5	51.8
TMS-12-2 SI = 1.3	507.6	33.7	38.4	8377.2	11.7	51.9
				7938.0	7.7	42.2
TMS-12-3 SI = 1.2	565.2	34.3	36.7	3366.0	17.3	56.6
				3625.2	26.0	60.2

TMS-12 alloy was higher than the strength of the TMS-1 alloy. It was found that for both alloys the strength sharply increased together with the increase of the SI value. The strength also decreases with the increase of the amount of  $\alpha$ -W, though there was hardly any effect when there is little amount of  $\alpha$ -W. At 1073 K, the strength of the TMS-1 alloy was higher than the strength of the TMS-12 alloy, contrary to what happens on the high temperature side. The strength of the TMS-12 alloy was approximately constant without depending upon the precipitation of  $\alpha$ -W and the SI value.

Among the alloys obtained TMC-32 and TMS-12-2 satisfied the target performance for obtaining the intermediate shape.

Next, for the purpose of clarifying the optional value of the Ta/W ratio when the solution index is kept constant, we designed improved alloys based on TMS-32 (SI = 1.3). The creep fracture strength of these alloys is shown in Table 2. The strength went up with the increase of Ta/W from 0.49 to 0.63 (TMS-34), but dropped sharply when the ratio was further increased. From the fact that the fracture life of the TMS-12 alloy is 8.38 Ms when the SI is 1.3 and Ta/W is 1.0, it was found that the value of Ta/W at which the maximum strength is obtained differs very much from one alloy system to another. The strength at 1073 K is independent of Ta/W.

Table 2. Influence of Ta/W in  $\gamma'$  phase on Creep Fracture Strength of Developed Alloys

Alloy	1073 K, 735.5 MPa			1313 K, 137.3 MPa		
	Life (ks)	Elonga- tion (%)	Contraction factor of cross section (%)	Life (ks)	Elonga- tion (%)	Contraction factor of cross section (%)
TMS-32 (0.49)	414.0	32.3	29.9	5292.0	18.3	42.7
	1494.0	26.3	29.9	5385.6	19.0	44.9
TMS-34 (0.63)	763.2	23.3	23.6	7315.2	12.0	37.3
				7351.2	14.7	37.1
TMS-35 (0.93)	1296.0	28.3	28.0	4820.4	27.7	51.6
				4705.2	18.3	48.8

## 2.5 Influence of Added Element Such as Mo and Ti

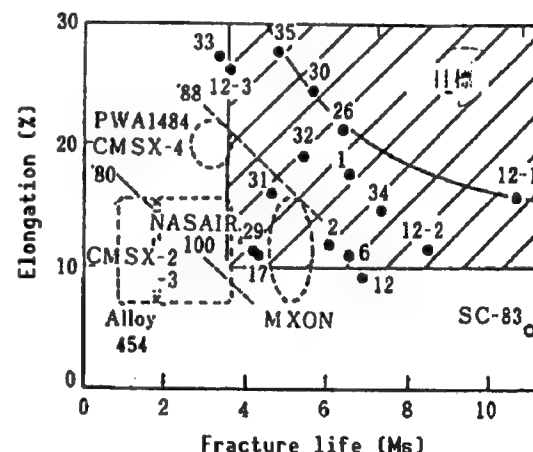
To develop alloys which have more stable structures of the two phases of  $\gamma$  and  $\gamma'$  and higher strength at high temperatures, alloys containing Mo(26), Ti(27), Mo and Ti(28), Mo, Ti, and Nb (29), and Re(30) were obtained with the alloy TMS-25 that contains Co as the base. In adding the alloying element, the amount of the  $\gamma'$  phase and the SI value of the  $\gamma'$  phase were kept constant. The added amount of each element was set at  $\Delta SI = 0.1$ , and Mo was replaced by W, and Ti and Nb were replaced by Ta. The computation for Re was not possible, so 2.5 wt% of Re was added for the entire composition and W was decreased by 2.5 wt%. In observing the structure of the heat-treated materials of the alloys, we saw that the  $\alpha$ -W phase was precipitated in the TMS-25, but the precipitation of the  $\alpha$ -W phase was not observed in alloys to which Mo, etc., is added. It became clear that the addition of such elements is an effective means for enhancing the stability of the structure. The result of the creep fracture test is shown in Table 3. Under the condition of 1313 K, the alloy added with Mo alone (TMS-26) had the best strength and ductility. The single addition of Ti was not an effective way to enhance the strength characteristic. The composite addition of Ti and Nb to the TMS-26 brought about a reduction of the strength. The single addition of Re showed a strength characteristic next to the alloy with single addition of Mo. Conditions of 1073 K and 735.5 MPa showed the most excellent strength characteristic similar to the case on the high-temperature side, but the alloy added singly with Re showed a large reduction of strength contrary to what happens on the high-temperature side. The single addition of Ti also brought about a reduction of the strength. The addition of Ti to TMS-26 did not result in such a strength reduction as at high temperatures, but the composite addition of Ti and Nb caused a drop in strength.

Table 3. Creep Fracture Characteristic of Alloys Added With Mo, Ti, etc.

Alloy	1073 K, 735.5 MPa			1313 K, 137.3 MPa		
	Life (ks)	Elonga- tion (%)	Contraction factor of cross section (%)	Life (ks)	Elonga- tion (%)	Contraction factor of cross section (%)
TMS-25	860.8 975.6	25.7 25.2	31.1 28.4	2156.4 2156.4	23.3 24.0	55.5 55.9
TMS-26 Mo	1242.0 910.8	26.3 27.7	29.4 27.8	6026.4 6390.0	27.0 21.3	46.7 46.2
TMS-27 Ti	511.2 651.6	22.7 20.7	29.0 29.6	2602.8 2667.6	37.7 16.8	49.7 50.8
TMS-28 Mo + Ti	784.8 1202.4	19.7 21.7	16.0 25.8	4820.4 4813.2	7.3 8.0	26.2 25.2
TMS-29 Mo+Ti+Nb	471.6 864.0	25.3 21.3	25.4 18.0	4212.0 4075.2	11.3 9.3	23.2 26.2
TMS-30 Re	565.2 630.0	31.3 34.2	18.0 34.3	5644.8 5529.6	24.7 17.0	40.2 39.1

A large number of alloys have strength characteristic that exceed the development goal. The relationship between the characteristic of these alloys and the development goal is shown in Figure 3 along with the characteristic of the existing single crystal alloys.

PWA 1484 is an alloy which is an improvement of Alloy 454 and it has Re of 3 wt%, but the rise in the strength is not so large. A series of the CMSX system alloys are improved alloys of the NASAIR100, and a feature of the CMSX-4 is that it contains 3 wt% of Re. The MXON is one of the CMSX series alloys. The SC-83 alloy contains a large amount of Mo and has an excellent fracture strength but its ductility is poor. It can be seen that the developed alloys have excellent strength characteristics compared with the existing alloys.



(●) represents an alloy developed by the present authors, and the hatched portion shows the development goal of the R&D Project, MITI

Figure 3. Comparison of Performance of Creep Fracture Life and Fracture Elongation Under Test Conditions of 1313 K and 137.3 MPa

## 2.6 Increasing the Accuracy of Alloy Design Method

The computational formula for the phase equilibrium in the alloy design method has been constructed on the basis of the composition of the  $\gamma$  and the  $\gamma'$  phases that have different heat treatments, so its accuracy is limited. Computation for Re was not feasible. For these reasons, we improved the computational formula for the distribution ratio of the equation for the  $\gamma'$  plane and each element to both phases in the old alloy design program by using the status analysis value through EPMA of the heat treated materials at 1173 K. A high correlation was found between the Al concentration in the  $\gamma'$  phase computed by using the new equation for the  $\gamma'$  plane and the experimental value obtained by EPMA. The constituents of the 40 kinds of alloy single crystal materials were analyzed and by using the result, the  $\gamma$  and  $\gamma'$  composition was separately computed by the above-mentioned phase equilibrium computational formula, and a formula was obtained for estimating longevity for treatment at 1313 K and 137.3 MPa. An estimation formula for lattice constant mismatch was also obtained.

## 2.7 Alloy Development by New Alloy Design Method

Using the new alloy design method, alloys with small specific gravity were designed under the conditions of the volume factor of  $\gamma' = 60$  at%, specific gravity  $<8.6$  ( $\text{g}/\text{cm}^3$ ), temperature range of heat treatment  $>40$  K, Cr quantity  $<7.0$  (at%), and SI value  $<1.1$ . The alloy TMS-64 (with an estimated life of 25.48 Ms) chosen from among the alloys of 8.5 specific gravity indicating structural stability, was used to obtain a single crystal by melting the raw materials, and the temperature range of heat treatment, specific gravity, and creep strength were measured. The temperature range of about 48 K and specific gravity of 8.48 agreed well with the computation. The fracture life was 17.89 Ms which was close to the estimated value (Figure 4). It was seen that the accuracy of the new alloy design method is very high.

## 2.8 Brief Summary

It was possible to develop many alloys which have strength characteristics that exceed the development goal. The representative compositions of the developed alloys are shown in Table 4. We succeeded in updating the alloy design method by which it was possible to enhance the accuracy of the alloy design and to design alloys which meet the required characteristics.

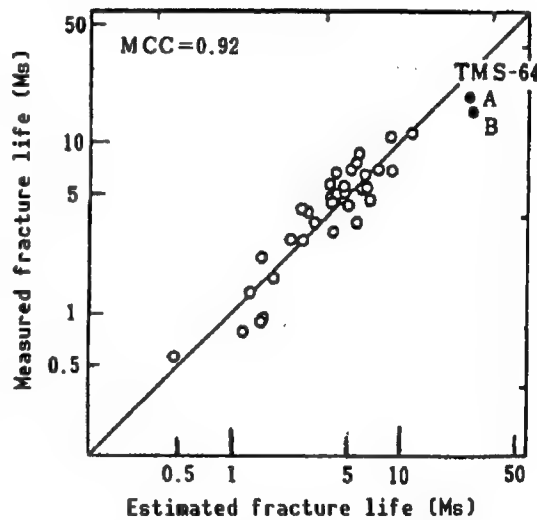


Figure 4. Comparison Between Creep Fracture Life by the Estimation Formula and the Experimental Value

Table 4. Composition of Representative Developed Single Crystal Alloys  
(mass%)

Alloy	Cr	Cr	Mo	W	Al	Ta	Ni
TMS-1	7.46	5.48	—	16.61	5.22	5.05	Bal
TMS-12-2	—	6.60	—	12.60	4.92	7.58	"
TMS-26	8.15	5.56	1.85	10.90	5.11	7.68	"
TMS-34	7.84	6.00	—	14.91	5.07	5.42	"
TMS-64	—	6.5	8.4	1.0	5.8	6.7	"

### 3. R&D on Oxide Dispersion Strengthened Alloys

#### 3.1 Foreword

The oxide dispersion strengthened (ODS) alloys are alloys that were developed to enhance the high-temperature strength of the heat-resistant alloys, and are manufactured by using an existing or developed superhigh heat-resistant alloy as the base and uniformly dispersing oxide particles. The manufacturing process consists of the mechanical alloying method and a subsequent extrusion processing and a heat treatment for unidirectional heat treatment.

The final goal of the present project is to "develop alloys which can withstand creep of over 3.6 Ms under conditions of 1373 K and 137.3 MPa (regarded as equivalent to creep of over 3.6 Ms under conditions of 1323 K and 156.9 MPa, considering the performance of the testing machine), and ensures a ductility of greater than 5 percent, and are also excellent in processability, recrystallizability, resistance to corrosion, etc." with higher strength performance than that of the existing alloy MA 6000.

In developing the ODS alloys, the alloy design method developed for the ordinary cast Ni-based heat-resistant alloys was applied, and alloy development was carried out by focusing attention mainly on the  $\gamma$  volume factor of the base alloy. As a result, several alloys that have strength characteristics that exceed the development goal were obtained.

#### 3.2 Alloy Design

The basic ideas for the design of the ODS alloys will be described following the process of R&D. The compositions of the designed alloys are shown in Table 5.

- 1) From the compositions of the ODS alloys, it will be seen that they have compositions equivalent to ordinary cast alloys except for the oxides (yttria:  $Y_2O_3$ ). For this reason, the alloy design method for Ni-based cast alloys is applied as is to the development of the ODS Ni-based alloys.

Table 5. Chemical Compositions of Alloys and Their Phases (mass%)

Alloy	$\gamma'$ (%)	Ni	Al	Co	Cr	Ti	Ta	W	Mo	Zr	C	B	$Y_2O_3$	Others
TM-220	65	58.9	4.9	9.0	5.2	1.0	3.7	14.6	1.8	0.05	0.11	0.01	0.8	Hf;0.8
TM-303	55	59.1	4.2	9.9	6.0	0.8	4.8	12.5	2.3	0.05	0.1	0.01	0.6	Hf;0.6
TMO-2	55	58.4	4.2	9.7	5.9	0.8	4.7	12.4	2.0	0.05	0.05	0.01	1.1	
$\gamma'$ phase(at%)		65.0	16.4	7.8	2.7	1.8	2.4	3.4	0.5					
$\gamma'$ phase(at%)		62.9	2.7	13.9	12.6	0.2	0.6	5.0	2.2					
TMO-19	0	55.8	1.1	12.4	9.9	0.2	1.9	14.3	3.2	0.05	0.05	0.01	1.1	
TMO-9	35	57.7	3.1	10.7	7.4	0.6	3.7	13.1	2.4	0.05	0.05	0.01	1.1	
TMO-8	45	58.3	3.7	10.2	6.6	0.7	4.3	12.7	2.2	0.05	0.05	0.01	1.1	
TMO-7	65	59.5	4.9	9.2	5.1	1.0	5.4	12.0	1.7	0.05	0.05	0.01	1.1	
TMO-20	75	60.1	5.5	8.7	4.3	1.1	6.0	11.6	1.5	0.05	0.05	0.01	1.1	
TMO-21	55	59.5	4.4	9.8	5.9	0.9	4.9	12.5	2.0	0.05	0.05	0.01	—	
MA 6000	52	68.4	4.6	—	15.2	2.5	2.0	4.0	2.0	0.15	0.05	0.01	1.1	
$\gamma'$ phase(at%)		72.8	15.5		3.9	5.2	0.8	0.8	0.5					
$\gamma'$ phase(at%)		62.7	3.5		29.6	0.5	0.2	1.4	1.9					

2) The compositions of the  $\gamma$  and  $\gamma'$  phases were computed by the use of the alloy design method from the composition (the base phase alloy) obtained by removing  $Y_2O_3$  from the existing ODS alloy MA 6000, and the solution index (SI = a grand total of values resulting from dividing the concentration of each element in the  $\gamma'$  phase by the solid solution of that element in the  $\gamma'$  phase) was determined, and the value was found to be 0.97. This value is small compared with the SI value 1.3 of the cast alloy developed by our Institute, revealing that the degree of solution strengthening is low. Utilizing this result, an alloy for casting TM-303 (SI = 1.27) was designed based on the high-strength cast alloy TM-220 developed for the ordinary cast alloy by paying attention to the ductility, reducing W, increasing Ta, and reducing the amount of the  $\gamma'$  phase from 65 percent to 55 percent. The product thus obtained was used for the base phase (alloy from which yttria is removed) for the alloy TMO-2. By casting the base phases of the TM-303 and the MA 6000, and testing them under creep conditions of 1273 K and 117.7 MPa, it was confirmed that the life of the TM-303 was 2934 ks (with elongation of 4.9 percent) which is greater than 698 ks (with elongation of 4.9 percent) of the MA 6000, and the former has a higher creep strength. The physical properties of the TM-303 and the MA 6000 computed by the alloy design method are shown in Table 6.

3) The ODS developed alloy TMO-2 was manufactured by adding yttria as a dispersant in the TM-303. The TM-303 has satisfactory secondary recrystallized structure, a high temperature creep fracture strength which is better than that of the MA 6000, achieving the target value, but the elongation was comparable to the MA 6000 which did not attain the target value. The strength in the medium to low temperature range was inferior to that of the Ni-based single crystal alloy so it cannot serve as a replacement alloy for single crystal alloys.

4) In order to obtain information for resolving the above-mentioned defects, alloys were designed that have  $\gamma'$  of 0, 35, 45, 65, and 75 percent without

Table 6. Values of Physical Properties Computed by Alloy Design Program

Parameter	TM-303	MA 6000C
S.l.	1.27( $\gamma'$ )0.79( $\gamma$ )	0.97( $\gamma'$ )0.61( $\gamma$ )
$N_V$	2.37( $\gamma'$ )1.83( $\gamma$ )	2.37( $\gamma'$ )2.27( $\gamma$ )
$N_V - N_V^C$	0.22	0.00
SFE	3.19	3.21
LM	-0.011(0.012*)	-0.0002

\* Measured value for TM0-2

S.l. : Solution index

$N_V$  : Decker's electron hole number

$N_V - N_V^C$  : Darrows' electron hole number (difference from the critical value)

SFE : Stacked layer mismatch energy

LM : Difference between lattice constants of  $\gamma$  and  $\gamma'$  phases

changing the composition of the  $\gamma$  and  $\gamma'$  phases of the TM0-2 (amount of the  $\gamma$ ; phase of 55 percent), and their characteristics were evaluated after the formation of the samples. In the case of the cast alloys it is known that maximum creep strength exists in the neighborhood of the  $\gamma'$  amount of 65 percent, and elongation decreases with the increase in the amount of  $\gamma'$ . The maximum creep of the ODS developed alloys with varying amounts of  $\gamma'$  under conditions of 1323 K and 176.5 MPa appeared in the vicinity of 65 percent of the  $\gamma'$ . In contrast, for 1123 K and 392.3 MPa, the creep increased with the increase of the amount of  $\gamma'$ . The elongation was small in the alloy with  $\gamma'$  of 35 percent, and no correlation with the amount of  $\gamma'$  was found. The creep of the alloy with  $\gamma'$  of 75 percent under the conditions of 1173 K and 392.3 MPa, was about four times as large as the single crystal alloy. These facts will be described in more detail.

### 3.3 Experimental Method

#### 1) Manufacture of ODS Materials

The ODS materials were manufactured using Benjamin's mechanical alloying method. The carbonyl nickel powder (INCO #123: 3~7  $\mu\text{m}$ , 0.1 wt% C), Mo, W, Ta, Co (~44  $\mu\text{m}$ ), and Cr (~77  $\mu\text{m}$ ), were used as the raw material powders, and Ni-46Al, Ni-18Al-28Ti, Ni-30Zr, Ni-4B (~77  $\mu\text{m}$ ), and yttria fine powder (20 nm) were used as the base alloy powder (numerals are for wt%).

These raw material powders were blended so as to have a composition as shown in Table 5. Three kg of the powder and 50 kg of steel balls (9.5 mm  $\phi$ ) were put in an attritor (in most cases, MA-3D made by Mitsui Miike, Co., with a capacity of 0.003  $\text{m}^3$ ), mechanically mixed for 180 ks in an Ar gas, to obtain composite powder.

The solid forming of the powder was done by extrusion. The composite powder was put in a soft steel can (outer diameter 70 mm, inner diameter 56 mm),

degassed for 10~15 ks at 723 K until the pressure became  $2 \times 10^{-3}$  Pa, and sealed by TIG welding. The soft steel can was held for 7.2 ks at 1323 K, and the ODS material was manufactured by extrusion at the extrusion ratio 15:1 and ram speed 400 mm/s.

The zone annealing (ZA) was carried out at the moving speed of 0.028 mm/s and at an appropriate temperature.

## 2) Testing Method

The hardness measurement was done at room temperature by heat treating the extruded materials at each annealing temperature. The creep testpiece was subjected to a solution and aging through heat treatment, after ZA, to 1573 K (or 1553 K) x 1.8 ks AC + 1353 K x 14.4 ks AC + 1143 K x 72 ks AC (AC: air cooled).

The testpiece was machine processed to be nonthreaded, 4 φ mm x 16 mm at the parallel section, and 10 R at the shoulder. The creep test was carried out, after holding at a specified test-temperature in air for 72 ks before loading, then applying a load at the shoulder. The hardness measurement was carried out using a micro Vickers hardness meter under the conditions of 500 g and 15 s.

## 3.4 Experimental Result and Consideration

### 1) Attritor Processed Compound Powder

By observing that the composite powder showed diffraction lines which are spread around the main diffraction lines of the BCC and FCC structures of the raw material powders, without showing diffraction lines like those of the FCC structure seen in extruded materials, it was concluded that it is a mixture of the BCC and the FCC structures.

### 2) Behavior of Secondary Recrystallized Particles

Since the ODS Ni alloy in extruded state consists of fine primary recrystallized particles, the strength as high-temperature structural materials is very low. This alloy has high-temperature strength for the first time when producing a structure with large grain aspect ratio (GAR) which extends in one direction as a result of formation of a secondary recrystallized structure by a subsequent zone annealing. Because of this, the behavior of the secondary recrystallization becomes important.

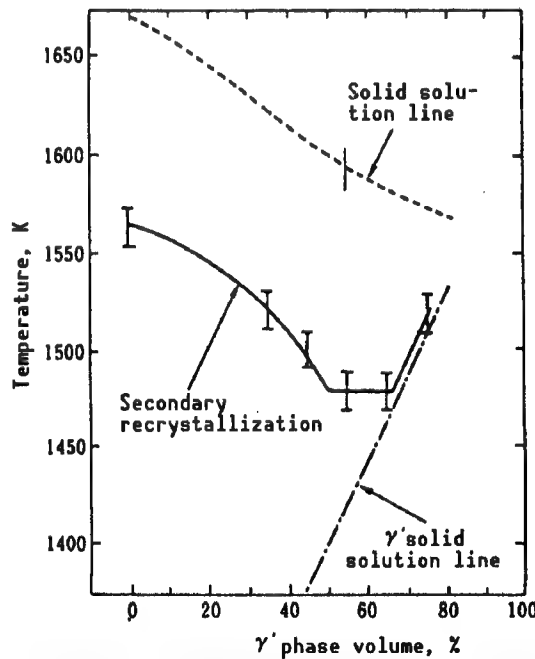


Figure 5. Relation Between  $\gamma'$  Phase Volume and Temperatures for Solid Phase Line, Second Recrystallization, and  $\gamma'$  Solid Solution Line

The relationship between the secondary recrystallization temperature and the amount of the  $\gamma'$  phase is shown in Figure 5. Let us consider triggering of the secondary recrystallization.

- (1) The secondary recrystallization temperature of the alloy for the  $\gamma'$  phase from 0–45 percent decreases with the increase of the  $\gamma'$  phase. The triggering of the secondary recrystallization is caused by the growth of the primary recrystallized grain boundary.
- (2) The second recrystallization temperature of the samples with  $\gamma'$  of 55 and 65 percent is constant, and it is plausible that yttria which is unchanged acts as a trigger.
- (3) The secondary recrystallization temperature of an alloy with  $\gamma'$  of 75 percent increases, but it coincides approximately with the  $\gamma'$  solid solution temperature, so that the solid solution of the precipitated  $\gamma'$  phase acts as the trigger of the secondary recrystallization.

Since the secondary recrystallization or the heat treatment of the ODS alloy is carried out at a temperature between the secondary recrystallization temperature and the melting temperature, for the alloy with  $\gamma'$  of 75 percent, the temperature range is very narrow. Therefore, the secondary recrystallization temperature for this alloy is difficult.

Figure 6 shows the X-ray diffraction patterns of a cross section perpendicular to the direction of the extrusion of the ODS alloys with various  $\gamma'$  amounts which is zone heat treated after extrusion. The alloys with  $\gamma'$  of 35 and 55 percent show mainly the  $<110>$  fiber aggregate structure, the alloys with  $\gamma'$  of 65 and 75 percent show mainly the  $<111>$  fiber aggregate structure. The strength at the medium to low temperature range is strengthened by the  $<111>$  fiber aggregate structure.

### 3) Creep Fracture

The result of the test under various creep conditions of the alloys TMO-9, 2, 7, and 20 with  $\gamma'$  of 35, 55, 65, and 75 percent is shown in Table 7. The creep temperature of ZA material of the TMO-9 with 35 percent of the  $\gamma'$  has far superior life and elongation in comparison to those of the materials processed under 1573 K and 3.6 ks, and there was an improvement in making rough and long crystal structures.

The TMO-2 alloy with  $\gamma'$  of 55 percent was not fractured after the lapse of more than 180 Ms (about six years) when processed under creep conditions of 1273 K and 117.7 MPa. The result of measuring the diameter of another testpiece which was subjected to the same conditions whose treatment was

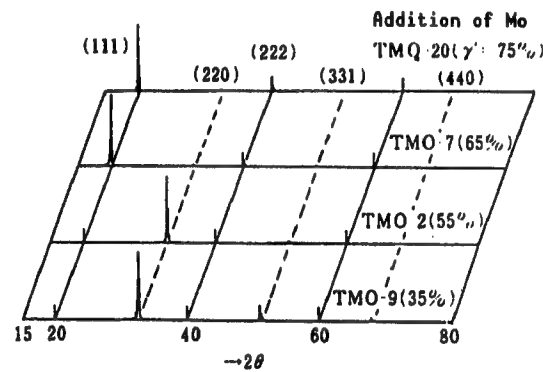


Figure 6. Relationship Between  $\gamma'$  Amount and X-Ray Diffraction Patterns of ODS Alloys

Table 7. Creep Fracture Characteristic  
of TMO-2 Series Alloys

Alloy	Testpiece	Temp. (K)	Stress (MPa)	Life (Ms)	Elongation (%)	Cross section contraction factor
TMO-9	25-2-4-1#	1323	156.9	0.0007	0.3	0.31%
$\gamma' = 35\%$	25-1-3-3##	1323	156.9	20.00	2.3	6.3
	25-1-3-2	1323	156.9	22.94	2.7	6.7
	25-2-4-2#	1123	343.2	0.44	0.4	0.2
	25-2-1-1##	1123	343.2	2.06	3.6	6.7
	25-1-3-1	1123	343.2	2.01	1.2	4.6
TMO-2	2-1	1323	156.9	12.60	3.7	7.0
$\gamma' = 55\%$	2-15	1173	245.2	16.87	3.6	12.6
	Z.A #### 2-12	1123	343.2	0.83	0.2	6.7
	2-38*	1273	117.7	194.91		
	2-8**	1273	117.7	180.04	0.98	3.3
TMO-2	S-5-	1323	176.5	5.72	4.6	8.2
$\gamma' = 55\%$	S-1	1323	156.9	26.91	4.1	8.8
	S-4	1233	225.6	5.84	3.6	5.7
	S-2	1123	343.2	4.05	4.7	8.7
	S-3	1123	392.3	0.37	4.6	8.5
	6-3-1	1323	156.9	33.96	1.7	3.1
TMO-7	7-1-1	1323	176.5	17.40	1.6	3.5
$\gamma' = 65\%$	35-2-2-3	1323	156.9	37.83	1.5	7.5
	40-1-1	1233	245.2	2.50	5.8	4.0
	35-2-2-2*	1123	343.2	106.69		
	40-1-2	1073	490.3	0.72	4.2	5.2
TMO-20	43-2-B-3	1323	176.5	12.81	1.0	1.8
$\gamma' = 75\%$	44-1-C-3*	1233	245.2	52.45		
	43-1-B-1	1173	392.3	16.96	1.5	2.1
	43-2-B-2	1123	392.3	24.26	1.4	3.0
	44-1-C-2*	1033	490.3	52.45		

\*Under test (as of 1-25-90      \*\* Test interrupted  
Heat treatment of testpieces with no special  
marks is: ZA+1300°C(1280°C)X0.5h+1080°CX4h+870°CX20h

# Heat treatment: 1300°C X1h      # means ZA alone

###[the table does not an      ZA:Zone annealing  
item with this mark]  
means various kinds of  
isothermal heat treatment  
(other than ZA)

interrupted at 180.04 Ms is shown in Table 7. This alloy is superior in resistance to oxidation at 1273 K having poor drawability with almost no thinning. This alloy has a large fracture elongation compared with others (in tests under higher stresses).

In the TMO-7 alloy with 65 percent of the  $\gamma'$  phase the life was 16.32 Ms under creep conditions of 1323 K and 176.5 MPa, showing the highest high-temperature strength.

The TMO-20 alloy with 75 percent of the  $\gamma'$  phase showed a life of 16.32 Ms under creep conditions of 1173 K and 392.3 MPa, and this is the alloy that has the highest strength at medium to high temperature. This value is over nine times compared with the life of 1.8 Ms of the existing single crystal alloy CMSX-4 under the same conditions, and is over four times compared with the life of 3.28 Ms of the single crystal alloy TMS-1 under the same conditions. From the relation between the  $\gamma'$  amount and the creep for 1123 K and 343.2 MPa, and 1323 K and 176.5 MPa determined from the relation in Figure 7, it was found that the life for the medium to low temperature of 1123 K increased with the increase of the  $\gamma'$ . This is because the amount of the  $\gamma'$  precipitate that is responsible for the strength at medium to low temperatures increased. From an electron micrograph of a sample fractured under the conditions of 1323 K and

176.5 MPa, it was seen that the dislocations at high temperature of 1323 K was shown by the sample with 65 percent of the  $\gamma'$ , but the reason for this is not known.

### 3.5 Brief Summary

1. The  $\gamma-\gamma'$  two-phase cast alloy design method developed by our Institute was applied to the development of the Ni-based ODS alloys. As a result, we succeeded in developing the TMO-2 alloy whose high-temperature creep strength is superior to that of the MA 6000.

2. Various ODS alloys ( $\gamma'$  of 55 percent) with varying  $\gamma'$  of 0~75 percent, without changing the composition of the  $\gamma'$  and  $\gamma$  phases, were developed. By examining the behavior of the secondary recrystallization it was determined what acts as the trigger for the secondary recrystallization.

3. The creep fracture characteristic was examined for the alloys with various  $\gamma'$  amounts described in the above. As a result, it was determined that the TMO-7 alloy with 65 percent of  $\gamma'$  is excellent for the high-temperature creep strength at 1323 K, and the TMO-20 alloy with 75 percent of  $\gamma'$  is excellent for creep strength at 1123 K. contrary to expectations, even for the alloy with 35 percent of  $\gamma'$ , the elongation was 3.6 percent at most, and it was not possible to obtain sufficient ductility for all alloys.

#### 4. R&D for Ni-Based Heat-Resistant Superplastic Alloys

##### 4.1 Foreword

The task regarding materials in this project is to design nickel alloys with tensile strength of 1569 MPa at 1033 K, and elongation of better than 20 percent, on the assumption that the powder obtained by solidification by HIP is superplastically forged.

In this design, the approach for developing the metallic materials was to apply the idea of the alloy design method to forged alloys that has been studied in the past to meet the required parameters for the forged alloys. The idea is that "In a two-phase nickel based alloy which is strengthened by the precipitated phases, various characteristics of the alloy are determined by the following five factors." The five factors are 1) amount of the  $\gamma'$  phase, 2) composition of the  $\gamma$  and  $\gamma'$  phases, 3) amounts of the trace doped elements such as carbon, boron, and zirconium, 4) conditions of heat treatment, and 5) the conditions of the manufacturing processes other than heat treatment such as preparation of alloy powder, HIP, and superplastic forging.

To design alloys based on this idea, it is necessary to establish the relation between these factors and the tensile test characteristics at 1033 K. In this research, of the five factors 3) and 4) were determined directly by experiments, and 1) and 2) were determined indirectly from the composition of the alloy as a whole by using the alloy design program.

The result is given in the following.

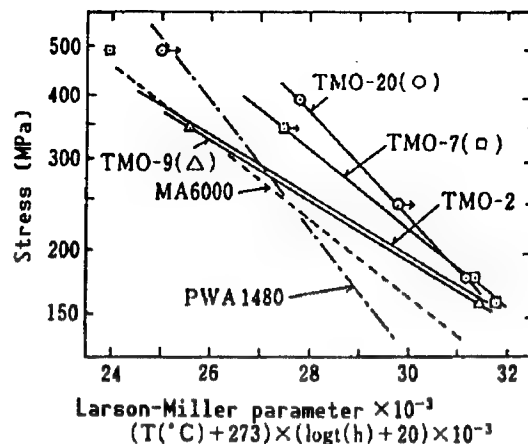


Figure 7. Larson-Miller Curves for TMO-2 Series ODS Alloys, MA 6000, and PWA 1480 Single Crystal Alloys

#### 4.2 Influence of the Amount of the $\gamma'$ Phase

In this alloy design, the optimum amount of the  $\gamma'$  phase was examined first.

This problem was studied, with the commercially available Rene-5 as the model, by keeping the composition of the  $\gamma$  and  $\gamma'$  phases constant and by studying a series of alloys which have different ratios of the two phases. Some sample alloys contain more than 100 percent of  $\gamma'$  phase. In such a case, the tie line which connects the composition of the  $\gamma$  phase alone is extended into the region of the  $\gamma'$  phase. For example, in an alloy with  $\gamma'$  phase of 125 percent, this represents the composition at the point where the length of the extension is 25 percent of the entire length of the tie line. The amount of the  $\gamma'$  phase varies with the temperature even for alloys with the same composition, the content of the  $\gamma'$  phase decreasing with the rise in temperature. Here, the nominal amount of the  $\gamma'$  phase of an alloy will be understood to mean the amount of the  $\gamma'$  phase at 1033 K unless otherwise noted. Therefore, even for an alloy with nominal amount of the  $\gamma'$  phase higher than 100 percent, it is possible to form an alloy with two phases of  $\gamma$  and  $\gamma'$  at temperatures higher than 1033 K. Note that the nominal amount of the  $\gamma'$  phase is the computed value and is not the measured value.

##### 4.2.1 Influence on the Superplastic Characteristics

As one necessary condition for an alloy to show superplasticity, the alloy should have the two-phase structure at a temperature where it exhibits superplasticity. For this reason, the influence of the amount of the  $\gamma'$  phase on the superplastic characteristic was studied as a part of the preliminary experiment.

In the experiment we used a method in which each alloy is pulverized by the rotary disk method, packed in a steel can, solidified by HIP; then the obtained block is worked into a cylinder, placed in a sheath, extruded to obtain a sample, and superplastic characteristic measured.

The superplasticity of the sample under certain conditions depended on the amount of the  $\gamma'$  phase. The influence of the amount of the  $\gamma'$  phase on the maximum value of the deformation resistance is not simple: it shows an increasing tendency up to 50 percent of the  $\gamma'$  phase, then falls off once up to 100 percent, and shows an increasing tendency again beyond 100 percent. By taking into account the fact that the amount of the  $\gamma'$  phase 1373 K where the superplasticity test was given is different from the amount at the standard temperature 1033 K of the nominal value, if one focuses attention only on the range of two-phase alloy at 1373 K, then one can say that the deformation resistance decreased with the increase of the amount of the  $\gamma'$  phase. As to the influence of the amount of the  $\gamma'$  phase on superplastic elongation, it was not possible to obtain data for the portion of the  $\gamma'$  phase which exceeds 80 percent. This is because reliable measurement on the superplastic elongation could not be obtained due to the fact that there were cracks in the extruded material for alloys with a large amount of the  $\gamma'$  phase. We surmise that the superplastic elongation increases uniformly with the amount of the  $\gamma'$  phase at 1373 K in the range of the  $\gamma'$  phase where the two-phase alloy is created.

The superplastic characteristic varied also with the extrusion conditions. According to the data for extrusion under various conditions, the superplastic characteristic of the material obtained was different depending upon the extrusion temperature, extrusion ratio, whether the powder was solidified before the extrusion, etc. If one uses the elongation at the time of deformation as the standard of the superplastic characteristic, it remained at around 500 percent when independent of the extrusion temperature up to 1423 K. But, when the temperature increased cases of decrease in the elongation appeared, there was almost no elongation at 1523 K for all alloys. In addition, the extrusion ratio also affected the superplastic characteristic, and it looked as if the extrusion temperature where it no longer shows the superplastic characteristic goes down by about 50 K when the extrusion ratio is high. For the same extrusion ratio and extrusion temperature, it seems that HIP processing before extrusion leads to deterioration in the superplastic characteristic.

#### 4.2.2 Influence on Superplastic Forging

Next, the relationship between the deformation resistance for superplastic forging and the amount of the  $\gamma'$  phase was studied. The deformation resistance at the time of superplastic forging generally varied with the degree of progress of the deformation. After a sharp increase in the beginning (up to deformation of 3 percent or so), it goes down somewhat, then it begins to increase from the vicinity of the deformation of 35 percent. In plotting the amount of the  $\gamma'$  phase and the deformation resistance at these inflection points (3 percent and 35 percent) and at the deformation of 70 percent which is close to the end point of the deformation, it was found that the deformation resistance did not depend strongly on the amount of the  $\gamma'$  phase except for the case of the alloy with  $\gamma'$  phase of 125 percent. A comparison between this result and the relationship between the  $\gamma'$  phase and the superplastic characteristic shows there is not necessarily a satisfactory correspondence and it was determined that the superplastic forging is possible even if a material does not show considerable superplasticity.

In addition, special defects among the products of superplastic forging were not observed except for the alloy with the  $\gamma'$  phase of 125 percent. The alloy with the  $\gamma'$  phase of 125 percent had many cracks so it was not possible to obtain a usable sample for tensile testing.

#### 4.3 Influence of Contents of Principal Elements

In determining the contents of the principal elements in an  $\gamma/\gamma'$  two-phase alloy, the  $\gamma'$  phase was given attention first by strengthening its composition by the solid solution method and by referring its properties to the previously obtained successive regression formula. Next, the composition of the  $\gamma$  phase which is an equilibrium with the  $\gamma'$  phase was computed. Finally, the composition of the alloy as a whole was determined. The procedure itself is the same as for cast alloys so the details will be omitted.

Figure 8 shows examples of comparison between the strength and the elongation by computation and the strength and the elongation by measurement. From the

figure, it can be seen that the correlation for UTS is satisfactory and the successive regression formula is sufficient for practical use. Regarding elongation, the correlation is somewhat less satisfactory, but it still seems to have some potential. Although the correlation of the regression formula does not necessarily mean that the regression formula can be used as is in the range outside of the actual measurement points. We trial manufactured alloys which should have been high performance alloys based on the computation, but the expected strength was not obtained.

#### 4.4 Influence of the Boron and Carbon Contents

It is usual to add a small amount of boron, carbon, hafnium, zirconium, etc., to cast or forged nickel alloys. This time, we examined the influence of adding elements by changing the contents of boron and carbon, in the range of boron content of 0.00~0.02 percent and carbon content of 0.02~0.20 percent. In the liquefaction treatment at 1523 K which is considered to be the optimum temperature for heat treatment, the maximum strength was seen momentarily with respect to the amount of boron when the carbon content is constant but, the strength fluctuated slightly in response to the carbon content when the boron content is kept constant. Further, the maximum elongation was achieved with respect to the amount of boron when the carbon content is constant. The elongation showed a tendency to decrease when the boron content is constant.

#### 4.5 Conditions of Heat Treatments

Concerning the influence of the heat treatments we studied the solution treatment, the aging treatment, and an intermediate heat treatment which is given once between the solution and the aging treatments.

##### 4.5.1 Solution Treatment

In the solution treatment, the three factors of temperature, time, and cooling rate after heat treatment are generally considered to be the most important, and sometimes the atmosphere for heat treatment is of concern. In this study, we fixed the atmosphere to an argon atmosphere, and studied the influences of the above three factors. To study the influence of temperature, samples which were superplastically forged after subjecting the powders to HIP processing were used. The heat treatment was done in two stages: the sample was held for one hour at a predetermined temperature, then cooled to room temperature by leaving the sample outside the furnace, and again held at 1033 K for 72 ks.

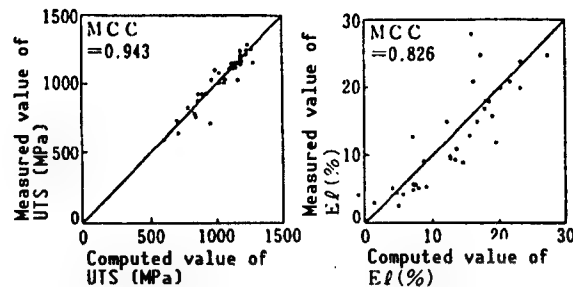


Figure 8. Comparison Between Computed Values and Measured Values for Verifying Correctness of Successive Regression Formula for Estimating Changes of Strength (UTS) and Elongation (El) Based on Addition of Elements

The maximum UTS was attained at a certain temperature through heat treatment, and beyond that temperature, the UTS inclined to decrease regardless of the amount of the  $\gamma'$  phase.

The solution temperature for which the maximum UTS was achieved varied with the content of the  $\gamma'$  phase. In alloys with a relatively small amount of  $\gamma'$  phase, this temperature is low, and it was almost independent of the content of the  $\gamma'$  phase. This is because the solution bath temperature is in the vicinity of the temperature for superplastic forging for alloys with a small amount of  $\gamma'$  phase, and melting and recrystallization are in progress before the solution treatment. In the region of a medium amount of the  $\gamma'$  phase which is slightly higher than the above, the temperature for which the maximum UTS is achieved moved rapidly toward the high-temperature side according to the increase of the amount of  $\gamma'$  phase. Comparison of the result of measurement carried out separately and the result of observing the structure shows that this temperature turned out to be somewhat higher than the solution bath temperature of the alloy. Further, the amount of the  $\gamma'$  phase at which the maximum UTS is achieved is in the neighborhood of 65 percent, and the sensitivity to the heat treatment temperature of the UTS was most conspicuous at this  $\gamma'$  phase. In the region where the amount of the  $\gamma'$  phase is higher the dependence in the heat treatment temperature of the UTS becomes small. In such alloys, the partial melting of the alloys started before the  $\gamma'$  phase was dissolved completely into the  $\gamma'$  phase.

The influence of the solution processing temperature and the amount of the  $\gamma'$  phase on the elongation were considerably different from the cases of the UTS or 0.2 percent yield strength. Except in the cases of extremely large or small amounts of  $\gamma'$  phase, when the amount of  $\gamma'$  phase is fixed, there were two solution processing temperatures at which the maximum elongation is obtained, with a greater maximum high temperature. The maximum low temperature was in the vicinity of 1323 K irrespective of the amount of the  $\gamma'$  phase, whereas the maximum high temperature increased with the amount of the  $\gamma'$  phase. When it comes to influencing the amount of the  $\gamma'$  phase by stabilizing the heat treatment temperature, the elongation reached the highest for the case of the  $\gamma'$  phase of 0 percent, with a tendency of decrease with the increase of the  $\gamma'$  phase, but the decreasing tendency was different depending on the time of heat treatment.

The problem of time was studied using alloys which contain a considerable amount of tungsten, and which presumably take a long time to reach equilibrium. The experiment was carried out by the method in which a sample was held at 1523 K for 3.6~14.4 ks, cooled in air to room temperature, then subjected again to heat treatment under 1023 K for 72 ks, and tensile strength characteristic at 1033 K compared. The result showed that the strength and the yield strength increased little by little with increasing length of time, but the elongation decreased with time when the time exceeded one hour. From this it was found that primary cooling for one hour is sufficient even for alloys that contain a large amount of tungsten (like the samples of this experiment) and longer cooling seems to be harmful.

#### **4.5.2 Cooling Rate**

The relationship between the cooling rate and the tensile strength was studied by measuring the characteristic of tensile strength of 1033 K for a sample obtained by holding a material of the same composition and the manufacturing method as in the above for 3.6 ks at 1523 K, then cooling the material to room temperature by four cooling speeds: water cooling; oil cooling; air cooling; and furnace cooling. Then the sample was again subjected to heat treatment at 1033 K for 72 ks.

In the case of water cooling, it was not possible to obtain a testpiece for tensile test because of the cracks in the sample. When the cooling rate was increased from furnace cooling to air cooling, both the strength and the yield strength increased, but the elongation was unchanged. When the cooling rate was further increased to the rate of oil cooling, the strength and the elongation tended to decrease, although the yield strength remained the same.

#### **4.5.3 Intermediate Heat Treatment**

This problem was studied by fixing the conditions of the solution and aging processing for the same alloys as in the above, and by adding one hour of heat treatment at varying temperatures between the above-mentioned two processes. In this case, the solution processing was carried out for 1.8 ks at 1523 K, and the aging processing was carried out for 72 ks at 1033 K. Except for the case of 1448 K, the intermediate heat treatment did not affect the strength and the yield strength, but the elongation decreased uniformly with the temperature of the intermediate heat treatment.

#### **4.5.4 Aging Processing**

As a result of processing for 72 ks at 1033 K which is the same temperature as the tensile test, the strength and the yield strength increased and the elongation decreased compared with the case where no aging processing was given.

### **4.6 Brief Summary**

During the project, we succeeded in developing alloys whose performance exceeds that of existing alloys. We did not succeed in developing alloys which far exceed the performance of the existing alloys. There seems to be many factors yet to be studied regarding elongation.

## **5. R&D of Ti-Based Superplastic Alloys**

### **5.1 Foreword**

The Ti alloys are light weight and have excellent toughness, and are most suitable as materials for aerospace equipment. The cutting workability of Ti alloys is poor, and in the case of components with complicated shapes such as aircraft components, the product yield in weight is extremely low and the cost in manufacturing the parts by cutting is of concern. Because the superplastic

processing is effective in improving the yield for processing, this research aimed at developing Ti alloys that have excellent superplastic characteristic and excellent mechanical characteristics. The goals were: 1) specific strength at 573 K of greater than 274.6 MPa/g/cm<sup>3</sup>; 2) the elongation of higher than 10 percent; and 3) the working yield over three times that of the conventional method. In this R&D, first, an alloy design method for multicomponent  $\alpha$ - $\beta$  type Ti alloys was created, then efficient alloy development was carried out by using the design method.

## 5.2 Alloy Design Method

Regarding the strength of Ti alloys there is a report that complex addition of a number of  $\beta$ -stabilizing elements is stronger than addition of one kind of  $\beta$ -stabilizing element. Based on this, R&D was done on the eight-component Ti alloy Ti-Al-Sn-Zr-V-Mo-Cr-Fe. In order to design equilibrium structures for the two phases  $\alpha$  and  $\beta$  in a multicomponent Ti alloy we developed the following three techniques (A, B, and C).

### 5.2.1 Method A

This is a technique based on the binary constitutional diagram Ti-j (j = Al, Sn, etc.) of Ti and each alloying element, and its procedure is given below.

- (1) First, the  $\beta$ -phase compositions ( $X_j^\beta$ ) for elements other than Al and Ti are set to have various values limited to the solid solution state of each element.
- (2) From the equation for the  $\beta$ -plane (Equation (1)) the Al concentration ( $X_{Al}^\beta$ ) in the  $\beta$ -phase at a set temperature is computed. The equation for the  $\beta$  phase is determined by representing the transformation temperature ( $T_\beta$ ) in the Ti-j binary constitutional diagram, and by summing the effect over all the alloying elements.

$$T_\beta = 1155 + \sum [a_j \cdot (X_j^\beta)^2 + b_j \cdot X_j^\beta] \quad (1)$$

where: 1155 is the transformation temperature (K) for pure Ti  
 $X_j^\beta$  is the concentration (at%) of the j-th element  
 $a_j, b_j$  are constants (Table 8).

Table 8. Constants in Equation (1) as Determined From the Binary Constitutional Diagram for Ti-j

j	Al	Sn	Zr	V	Mo	Cr	Fe
$a_j$	-0.300	0.646	0.152	0.226	0.093	0.630	0.340
$b_j$	18.241	-9.893	-3.107	-17.057	-19.047	-24.430	-18.048

- (3) The composition of the  $\alpha$  phase which is in equilibrium with the  $\beta$  phase as set in (1) and (2) at a set temperature is determined from Equation (3) by using the distribution ratio (Equation (2)).

$$\begin{aligned}
C_{Al} &= 1.426 - 0.0148 \cdot X_{Al}^{\beta} \\
C_V &= 0.731 - 0.263 \cdot X_V^{\beta} \\
C_{Zr} &= 0.914 - 0.032 \cdot X_{Zr}^{\beta} \\
C_{Sn} &= 0.928, C_{Mo} = 0.078, C_{Cr} = 0.081, \\
C_{Fe} &= 0.089
\end{aligned} \tag{2}$$

$$X_j^{\alpha} = C_j + X_j^{\beta} \tag{3}$$

(4) Whether there is precipitation of  $\alpha_2$  phase which is a detrimental phase for the composition of the  $\alpha$  phase is confirmed by Equation (4).

$$X_{Al}^{\alpha} + X_{Sn}^{\alpha}/3 + X_{Zr}^{\alpha}/6 + 10 \cdot X_0^{\alpha} \leq 9 \text{ mass\%} \tag{4}$$

where  $X_i^{\alpha}$  are in the mass% only in Equation (4).

(5) Set the volume factor of the  $\alpha$  phase ( $V_{\alpha}$ ) at a set temperature, and compute the overall composition for the alloy by Equation (5).

$$X_j = V_{\alpha} \cdot X_j^{\alpha} + (i - V_{\alpha}) \cdot X_j^{\beta} \tag{5}$$

### 5.2.2 Method B

An alloy design method B based on the composition data for the  $\alpha$  and  $\beta$  phases that are in equilibrium, aimed at enhancing the design accuracy. The method  $\beta$  refers to the design method of the  $\gamma + \gamma'$  type Ni-based superhigh heat-resistant alloys developed by our Institute.

An equation for the  $\beta$  plane and a regression formula corresponding to the deterioration ratio was obtained using the analytical composition data by EPMA on the  $\alpha$  phase and the  $\beta$  phase, in 21 kinds of alloy samples that are put in equilibrium at 1173 K.

The use of method B made it possible to design alloys with higher accuracy compared with method A, at 1173 K.

### 5.2.3 Method C

Thermodynamic computations concerning the equilibrium between the  $\alpha$  phase and the  $\beta$  phase in multicomponent Ti alloys were carried out using the Hillert's quasi regular solution model. For the free energy of each element and the interaction parameters, the values reported by Kaufman, et al., were mainly used.

As a result of computation of the volume of the  $\alpha$  phase at various temperatures it was found that they are in good agreement with the measured values. In addition, a satisfactory agreement was also obtained for the deterioration ratio to the two phases of each element. From this result, it was found that the phase equilibrium calculations by thermodynamics are also possible in the multicomponent Ti alloy that involves the eight elements.

### 5.3 Alloy Development

#### 5.3.1 Superplastic Characteristic

A superplastic test was conducted at a strain rate of  $6.7 \times 10^{-4} \text{ s}^{-1}$ , at various test temperatures in the range of 1023–1323 K, using four kinds of alloys (GT-9, 33, 45, and 46, (see Table 9)) showing distinctively different  $\beta$ -Transus to obtain the design standards for Ti alloys suitable for superplastic processing by clarifying the volume factors of the  $\alpha$  phase and the  $\beta$  phase for the optimum superplastic processing and the temperature. As a result, each alloy has shown a large elongation which exceeds 400 percent at temperatures below 1123 K. On the other hand, all alloys showed maximum deformation stress which is low in the vicinity of 20 MPa for the temperature range of 1123–1223 K but the value went up sharply for temperatures below 1073 K. From this result, the optimum temperature for superplastic processing is considered to lie in the range 1073–1123 K. From the fact that the GT-33 alloy showed the largest elongation and the smallest deformation stress, among the designed alloys, it was found that a temperature around 1123 K is most suitable as the design temperature.

Table 9. Chemical Compositions of Representative Alloys Developed (mass%)

Alloy	Al	V	Sn	Zr	Mo	Cr	Fe	O	Ti
GT-5	3.6	—	6.3	12.1	1.1	—	—	0.09	Bal.
GT-9	5.7	0.5	1.4	3.9	1.0	1.3	1.0	0.12	Bal.
GT-10	5.0	0.7	1.2	9.1	0.5	0.6	0.7	0.11	Bal.
GT-11	5.2	0.5	2.7	5.5	0.6	0.6	1.2	0.12	Bal.
GT-15	4.8	0.7	2.1	3.7	0.7	0.6	1.0	0.11	Bal.
GT-16	6.0	0.6	1.1	10.6	0.5	0.5	1.2	0.10	Bal.
GT-33	6.5	1.4	1.4	1.0	2.9	2.1	1.7	0.11	Bal.
GT-45	6.4	2.9	0.9	1.1	2.5	2.5	1.6	0.11	Bal.
GT-46	5.7	1.5	0.9	5.1	2.5	3.5	2.6	0.16	Bal.

#### 5.3.2 Tensile Characteristic at 573 K

In the beginning, alloys were designed by the alloy design method A so as to have the ratio of 1:1 for the  $\alpha$  phase and the  $\beta$  phase at 1173 K. Seventeen kinds of alloys (GT1 to GT17) were manufactured. Table 9 shows the chemical compositions of the representative alloys. Each alloy was given a tensile test at 573 K by subjecting it to a solution treatment of 1173 K x 3.6 ks, water cooling, then to an aging treatment for 14.4 ks at various temperatures. As a result, the GT-9 alloy showed the specific strength and the elongation that satisfy the development target (hatched part in Figure 9) of this project.

Next, alloys were designed in which the added amount of the  $\beta$  phase stabilizing elements such as V, Mo, Cr, and Fe, by reducing the design temperature (temperature for which the ratio of the  $\alpha$  phase and the  $\beta$  phase is 1:1) from 1173 K (GT-1 to GT-17), to 1123 K (GT-33), 1073 K (GT-46), and 1023 K (GT-46)

(see Table 9). As a result, the alloys GT-33, 45, and 46 showed characteristics that exceed the development target (Figure 9).

In order to quantitatively show the influence of the various structure factors (volume factor ( $V_\alpha$ ) of the primary  $\alpha$  phase and crystal grain size ( $a_\alpha$ )) and the composition factors (solid solution strengthening degree ( $dDE^\alpha$ ) of the primary  $\alpha$  phase, and electron/atom ratio ( $e/a^\beta$ )) on the tensile characteristic of the materials subjected to a solution and aging treatments, the relationship between these factors and the tensile characteristic shown in Figure 1 was studied using successive regression analysis, and the following regression formula was obtained.

$$\begin{aligned}\sigma_u \text{ (MPa)} = & 2037.0 - 3092.3 \cdot V_\alpha \\ & + 1171.2 \cdot V_\alpha \cdot dDE^\alpha \\ & + 1746 \cdot (1-V_\alpha) \cdot (e/a^\beta - 4) \\ & - 186 \cdot (1-V_\alpha) \cdot T_{ag}/100\end{aligned}\quad (6)$$

$$El.\% = -19.86 - 9.28 \cdot V_\alpha + 13.08 \cdot dDE^\alpha + 2.95 \cdot T_{ag}/100 \quad (7)$$

The  $dDE^\alpha$  was expressed by the following formula which is an extension of the research result concerning the solid solution strengthening of  $\alpha$ -Ti by Sasano and Kimura:

$$dDE^\alpha = \sum X_i \cdot |(D_i - D_{Ti})/D_{Ti}| \cdot 100 + \sum X_j \cdot \Delta\rho_j, \quad (8)$$

where  $i$  is a transition metal element

$j$  is a nontransition metal element

$X_i$  and  $X_j$  are the concentrations (at%) of the  $i$  and  $j$  elements in the primary  $\alpha$  phase

$D_i$  and  $D_{Ti}$  are atomic radii (Table 10)

$\Delta\rho_j$  is the change in the electrical resistance when unit concentration of  $j$  element is added ( $\Omega \cdot \text{cm}/\text{at\%}$ , see Table 10).

### 5.3.3 Optimization of Tensile Characteristic and Superplastic Characteristic

Based on the results in 5.3.1 and 5.3.2, we tried to optimize the tensile characteristic and the superplastic processing. By setting the ratio of both phases at 1123 K at 1:1, and by optimizing the strengthening parameters ( $dDE^\alpha$  and  $e/a^\beta$ ) based on the information obtained from Sections 2 and 3, alloys GT-60 and 61 that exceed the performance of the alloys previously developed were created (Figure 1).

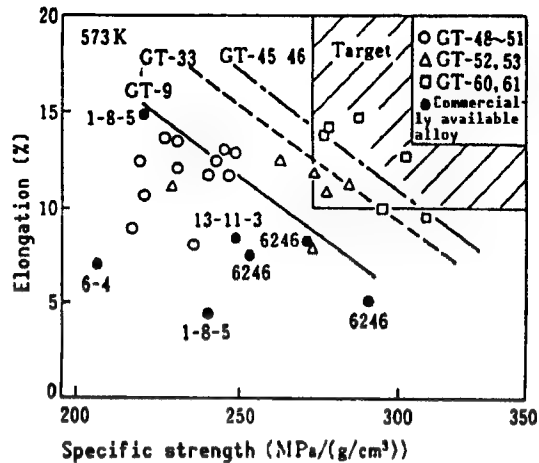


Figure 9. Tensile Characteristic at 573 K of the Alloys Developed

Table 10. Constants in Equation (8)

Element	Transition element (i)					Nontransition element (j)	
	V	Zr	Cr	Mo	Fe	Al	Sn
$  (D_i - D_{Ti}) / D_{Ti}   \cdot 100$	8.93	9.69	13.56	5.71	14.15	—	—
$\Delta \rho_j (\Omega \cdot \text{cm}/\text{at\%})$	—	—	—	—	—	14.40*	17.61*

\*: By Sasano, et al.

## 6. Evaluation of High-Temperature Fatigue Characteristics

### 6.1 Foreword

When high-temperature titanium alloys are used in the compressor vanes of the gas turbines for aircraft, creep and low cycle fatigue are of concern. The creep life of the  $(\alpha + \beta)$  type titanium alloys varies markedly with the ratio of these two phases. The influence of the microscopic structures, grain size, temperature, environment, etc., on the high-temperature low cycle fatigue was studied, but the effect of the ratio of the two phases is not known. Therefore, a series of titanium alloys was designed by keeping the chemical composition of the two phases, and the ratio of the two phases alone is varied, to examine the influence of the ratio of the two phases in the high-temperature low cycle fatigue characteristic.

### 6.2 Experimental Method

The titanium alloys (GT-69 to GT-71) are those designed to have the volume factors of the  $\alpha$  phase of 68, 27, and 10 percent at 1173 K, based on the composition of the  $\alpha$  phase and  $\beta$  phase of the GT-60 alloy which has excellent superplastic characteristic and the specific strength at 573 K. The chemical composition of these alloys is shown in Table 11.

Table 11. Chemical Compositions of GT-69 to GT-71 Alloys

GT	Al	V	Sn	Zr	Mo	Cr	Fe	O	N	Ti
69	8.49	1.23	0.52	0.99	0.35	0.51	1.76	0.11	0.005	Bal.
70	7.20	1.78	0.49	0.85	0.43	0.91	3.23	0.15	0.005	Bal.
71	6.78	1.84	0.51	0.97	0.56	1.10	3.88	0.15	0.005	Bal.

After melting these alloys for double arcs in an Ar gas atmosphere, round bars 30 mm in diameter were obtained by forging and rolling them at 1173~1223 K. The round bar was worked to a flattened round bar testpiece with 8 mm between

the parallel sides x 20 mm in length, quenched the sample in water after holding it at 1173 K for 3.6 ks, and the sample was subjected to aging treatment at 773 K for 14.4 ks. Tensile and low cycle fatigue tests were put to a sample in the air at a test temperature of 773 K by using a hydraulic servo type fatigue testing machine. The conditions of the fatigue test were strain waveform of a triangular wave, strain rate of  $1.67 \times 10^{-2} \text{ %/s}$ , for three strain ranges of  $\pm 0.25$ ,  $\pm 0.50$ , and  $\pm 1.00$  percent, and the repetition number of fracture was determined.

### 6.3 Result and Consideration

The microscopic structure of each alloy after heat treatment is shown in Photograph 1 [not reproduced]. Namely, the primary  $\alpha$  phase was equi-axed crystal for the GT-69 alloy, and needle crystal for the GT-70 and 71 alloys, whereas the  $\beta$  phase consisted, for all alloys, of fine precipitated  $\alpha$  phase and tempered martensitic phase.

The mean grain size of the GT-69 alloy was  $5.8 \mu\text{m}$  for  $\alpha$  phase and  $3.5 \mu\text{m}$  for  $\beta$  phase, the needlelike  $\alpha$  phase of the GT-70 and 71 alloys was  $6\text{-}7 \mu\text{m}$  long and  $1.4 \mu\text{m}$  wide, and the old  $\beta$  phase had a grain size of about  $400 \mu\text{m}$ .

Table 12. Tensile Property of GT-69 to GT-71 Alloys

GT	Temper- ature (K)	$\epsilon$ (1/s)	$\sigma_{0.2}$ (MPa)	$\sigma_{UTS}$ (MPa)	Elonga- tion (%)	R.A. (%)
69	773	$6.65 \times 10^{-5}$	578	715	20	82
70			685	720	30	97
71			640	788	32	99

The results of the tensile test and the low cycle fatigue test at 773 K are shown in Table 12 and Figure 10, respectively. The repetition number to fracture  $N_f$  was  $10^4$ ,  $10^3$ , and  $10^2$  for the total strain range  $\Delta\epsilon_t$  of 0.50, 1.00, and 2.00 percent, respectively, for all alloys, showing that the change in the ratio of the two phases did not affect the  $N_f$  much. The fatigue life of the  $(\alpha + \beta)$  type titanium alloys is known to be longer for the equi-axed  $\alpha$  phase than for the needlelike  $\alpha$  phase. A comparison of the life among the alloys showed that the GT-69 alloy which has the largest volume factor for the  $\alpha$  phase had the greatest

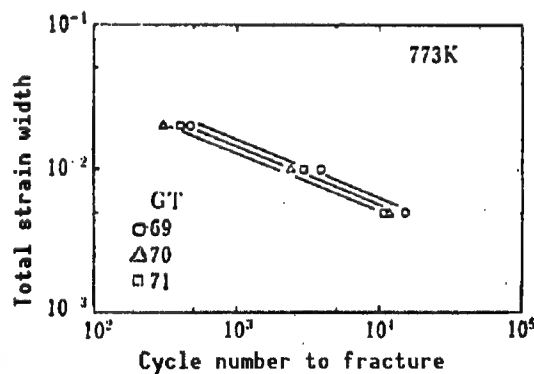


Figure 10. Result of Low Cycle Fatigue Test for GT-69 to GT-71 Alloys

value for all cases of  $\Delta\epsilon_t$ . In the GT-70 and 71 alloys which have small volume factor, the life of the GT-71 alloy with small volume factor for the  $\alpha$  phase was longer than that of the GT-70 alloy, except for the case of  $\Delta\epsilon_t$  of 0.50 percent. The degree of difficulty of generating cracks has something to do with this. As a result of measuring the number of cracks per unit length in a cross section perpendicular to the longitudinal direction of the sample after fracture, it was found that the life is longer when the number of the cracks is smaller (Table 13).

Table 13. Number of Cracks Per Unit Length in Cross Section Perpendicular to Longitudinal Direction

$\epsilon_t(T)$	Number of cracks (1/mm)		
	0.50	1.00	2.00
GT			
69	0.00	0.22	2.95
70	0.07	0.64	6.83
71	0.08	0.35	3.08

$\epsilon_t$ : Total strain

#### 6.4 Brief Summary

Titanium alloys with the same composition of the  $\alpha$  phase and the  $\beta$  phase and with different ratios were designed, and the effect of the ratio of the two phases in the high-temperature low cycle fatigue life was investigated.

- (i) The change in the ratio of the two phases did not affect much the high-temperature low cycle fatigue life.
- (ii) A comparison among alloys indicated that the life is related to the number of cracks per unit length.

#### 7. Evaluation of Corrosion Resistance

The addition of W, Ta, Mo, etc., plays an important role in enhancing the strength of the Ni-based single crystal alloys. For this reason, we studied what influence the addition of such a strengthening element has on the corrosion resistance of the alloys, by the burner rig test method. As the specimens, a series of Ni-based single crystal alloys with varying ratios of Ta/W and Mo/W was used. The test was carried out under the conditions of the temperature 1123 K of the burner rig test piece, flow speed Mach 0.5 of the combustion gas, NaCl concentration of 5 ppm (weight ratio to the air for combustion), sulfur concentration of 0.5 percent (weight ratio to the fuel), and the test time of 25.2 ks. Figure 11 shows the effect of the W/Ta ratio on the corrosion of the alloys.

It was found that the corrosion of the TMS-19 with small W/ta ratio is far lower than that of the TMS-1, -12, and -17 which have large ratios of W/ta. The corrosion structures of the cross sections of the alloys are shown in Photograph 2 [not reproduced]. In contrast to the fact that there remain almost no surface oxides for the three alloys that have large corrosion, a thick oxide layer remains on the surface in the TMS-19 that has little corrosion. This thick oxide layer was identified to be NiO by EPMA analysis and X-ray diffraction. It was found that a thin  $\text{Al}_2\text{O}_3$  layer is formed on the inside of the thick oxide layer. In alloys with a large Al content such as the Ni-based single crystal alloys it is known that the  $\text{Al}_2\text{O}_3$  layer acts as a protective layer against oxidation. In the TMS-19, the continuous protective  $\text{Al}_2\text{O}_3$  film formation is believed to be the direct cause of the small amount of corrosion. It is believed that the thick NiO layer seen on the surface indirectly contributes to the corrosion resistance of the alloy by creating an atmosphere of low oxygen to bring about selective oxidation of Al in the interior of the alloy. In the three alloys TMS-1, -12, and -17 which have a large amount of W, the oxide of W helps the melting of NiO into  $\text{Na}_2\text{SO}_4$ , so the formation of a thick NiO layer such as that seen in the TMS-19 will not take place. In these alloys, the formation of oxides of the various kinds of alloying elements on the surface is taking place, so overall corrosion occurs since a continuous  $\text{Al}_2\text{O}_3$  protective film is not formed.

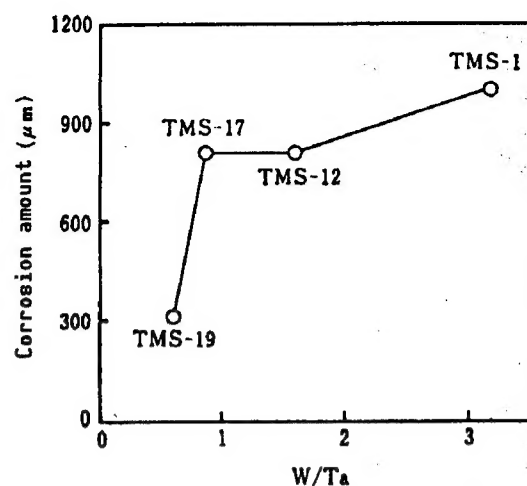


Figure 11. Effect of the W/Ta Ratio on the Amount of Corrosion

Table 14. Composition (at%) and Amount of Corrosion of Burner Rig Corrosion Testpiece

Alloy	Cr	Al	Co	W	Mo	Ta	Others	Amount of corrosion
TMS-19	8.0	11.0	—	2.7	—	4.4		312
TMS-17	8.0	11.3	—	3.4	—	3.9		809
TMS-12	8.0	12.2	—	4.4	—	2.7		811
TMS-1	6.7	12.3	8.1	5.8	—	1.8		1001
TMS-50	6.58	10.5	9.69	2.34	2.73	2.63	0.013Nb	449
TMS-48	6.58	10.7	9.26	3.01	2.04	2.57	0.02Nb	494
TMS-39	6.63	10.9	9.06	3.77	1.2	2.5		620
TMS-64	7.34	12.8	—	0.32	5.18	2.2		526

Ni: remainder

The effect of W as described in the above is also reported on Mo. Therefore, we investigated the corrosion behavior of the alloys (TMS-50, -48, and -39) in which the ratio of W/Mo is changed. Table 14 shows the corrosion of the various alloys. It was found that the corrosion decreases with the increase in Mo. The reason for this is that the Mo oxide is highly volatile so it is difficult to remain on the surface of the testpiece in an atmosphere of a high-speed combustion gas such as in the burner rig test. Therefore, its effect on accelerating corrosion is small compared with the case of W. Figure 12 shows the high-temperature corrosion characteristic of the proposed alloys.

It was found that the TMS-64 has lower corrosion in the burner rig test despite the fact that it has a superior high-temperature strength characteristic compared to TMS-1 and -12 which were proposed in the beginning. This relates to the fact that in contrast to TMS-1 and -12 which are alloys strengthened by W, the TMS-64 is an alloy strengthened by Mo.

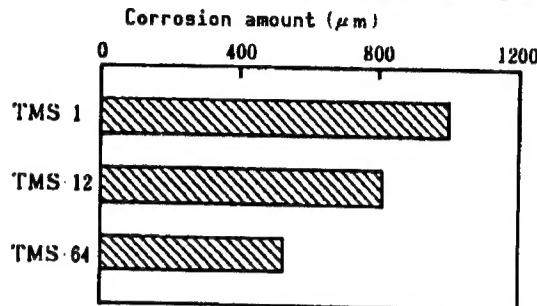


Figure 12. Corrosion of Proposed Alloys

#### 8. Conclusion

Over a period of eight years, research on the high-performance crystal controlled alloys has been carried out, and the project was safely completed. The high-performance crystal controlled alloy project strives to make the best crystal condition of an alloy suited for the composition by highly controlling both its components and process. It is possible to think of a fairly large number of materials and processes that fall in the above-mentioned range. Due to budget restrictions, this research was conducted on four kinds of alloys consisting of three kinds of Ni system alloys and one kind of Ti system alloy. We are proud that very significant results were obtained in this project thanks to the cooperation of a large number of people.

This project was carried out with the participation of this Institute, two national laboratories, and seven related private companies, promoted by the Science and Technology Agency and the Next-Generation Metals and Composites Research and Development Association, Inc. In this report, only the portion over which this Institute had charge was presented. We are grateful to various agencies and organizations for their kind cooperation and assistance over a period of many years.

- END -

NTIS  
ATTN PROCESS 103  
5285 PORT ROYAL RD  
SPRINGFIELD VA

2

22161

This is a U.S. Government publication. Its contents in no way represent the policies, views, or attitudes of the U.S. Government. Users of this publication may cite FBIS or JPRS provided they do so in a manner clearly identifying them as the secondary source.

Foreign Broadcast Information Service (FBIS) and Joint Publications Research Service (JPRS) publications contain political, military, economic, environmental, and sociological news, commentary, and other information, as well as scientific and technical data and reports. All information has been obtained from foreign radio and television broadcasts, news agency transmissions, newspapers, books, and periodicals. Items generally are processed from the first or best available sources. It should not be inferred that they have been disseminated only in the medium, in the language, or to the area indicated. Items from foreign language sources are translated; those from English-language sources are transcribed. Except for excluding certain diacritics, FBIS renders personal names and place-names in accordance with the romanization systems approved for U.S. Government publications by the U.S. Board of Geographic Names.

Headlines, editorial reports, and material enclosed in brackets [] are supplied by FBIS/JPRS. Processing indicators such as [Text] or [Excerpts] in the first line of each item indicate how the information was processed from the original. Unfamiliar names rendered phonetically are enclosed in parentheses. Words or names preceded by a question mark and enclosed in parentheses were not clear from the original source but have been supplied as appropriate to the context. Other unattributed parenthetical notes within the body of an item originate with the source. Times within items are as given by the source. Passages in boldface or italics are as published.

#### SUBSCRIPTION/PROCUREMENT INFORMATION

The FBIS DAILY REPORT contains current news and information and is published Monday through Friday in eight volumes: China, East Europe, Central Eurasia, East Asia, Near East & South Asia, Sub-Saharan Africa, Latin America, and West Europe. Supplements to the DAILY REPORTS may also be available periodically and will be distributed to regular DAILY REPORT subscribers. JPRS publications, which include approximately 50 regional, worldwide, and topical reports, generally contain less time-sensitive information and are published periodically.

Current DAILY REPORTS and JPRS publications are listed in *Government Reports Announcements* issued semimonthly by the National Technical Information Service (NTIS), 5285 Port Royal Road, Springfield, Virginia 22161 and the *Monthly Catalog of U.S. Government Publications* issued by the Superintendent of Documents, U.S. Government Printing Office, Washington, D.C. 20402.

The public may subscribe to either hardcover or microfiche versions of the DAILY REPORTS and JPRS publications through NTIS at the above address or by calling (703) 487-4630. Subscription rates will be

provided by NTIS upon request. Subscriptions are available outside the United States from NTIS or appointed foreign dealers. New subscribers should expect a 30-day delay in receipt of the first issue.

U.S. Government offices may obtain subscriptions to the DAILY REPORTS or JPRS publications (hardcover or microfiche) at no charge through their sponsoring organizations. For additional information or assistance, call FBIS, (202) 338-6735, or write to P.O. Box 2604, Washington, D.C. 20013. Department of Defense consumers are required to submit requests through appropriate command validation channels to DIA, RTS-2C, Washington, D.C. 20301. (Telephone: (202) 373-3771, Autovon: 243-3771.)

Back issues or single copies of the DAILY REPORTS and JPRS publications are not available. Both the DAILY REPORTS and the JPRS publications are on file for public reference at the Library of Congress and at many Federal Depository Libraries. Reference copies may also be seen at many public and university libraries throughout the United States.